A Study of Medium and High Voltage Form-Wound Coil Turn-to-Turn Insulation of Converter Fed Rotating Machines

by

Mohammad-Saleh Moonesan

A thesis

presented to the University of Waterloo

in fulfillment of the

thesis requirement for the degree of

Doctor of Philosophy

in

Electrical and Computer Engineering

Waterloo, Ontario, Canada, 2016

AUTHOR'S DECLARATION

I hereby declare that I am the sole author of this thesis. This is a true copy of the thesis, including any required final revisions, as accepted by my examiners.

I understand that my thesis may be made electronically available to the public.

Abstract

Converter fed medium voltage motors are increasingly being employed in industrial processes due to their higher efficiency and greater flexibility with respect to speed control. The increased use of motor adjustable speed drives has raised concerns about the adverse effects of the distorted voltage waveform of the converter on the insulation of the machine. Recent designs include a higher level of insulation than that are used in conventional AC-fed motors because of the presence of fast transients and harmonics in the voltage waveforms at the motor terminals. Many studies have focused on this problem, with most emphasizing on the stress-grading system and relatively a few investigating the form-wound turn insulation, with some contradictory reported results. Hence, the focus of the present research is to study the turn insulation of form-wound machines subjected to distorted voltage waveforms from converter pulses.

The effect of pulse parameters such as rise time, pulse duty cycle, and switching frequency on the times-to-failure of turn insulation under unipolar and bipolar square pulses are investigated. Back-to-back turn insulation samples, with enamel insulation, were prepared based on IEC 60034-18-42 with improved insulation in the crotch region of the samples to prevent failures in this region. A high voltage pulse generator, and an antenna based PD measurement system, were implemented in order to investigate significant factors affecting insulation system using PD activity measurements and times-to-failure experiments. The experimental results were used to identify the significant parameters of aging as well as suggesting the aging mechanism involved.

A point-to-plane setup having an insulation film representing a single defect in turn insulation system, was also implemented to investigate the PD features and their relationship to the times-to-failure of back-to-back samples in depth. Using this setup, a series of measurements were carried out to investigate the significance of charge accumulation on the times-to-failure of insulation samples. By conducting surface charge measurements, surface potential measurements, and COMSOL$^{®}$ simulations on the point-to-plane setup with different insulation films, the influence of accumulated charge in modifying the electric field and therefore the times-to-failure of insulation systems was studied for different pulse types and switching frequencies in order to explain the results of aging experiments and to validate the presented aging mechanism.

Acknowledgements

To my dear wife and parents.

Table of Contents

List of Figures

List of Tables

Chapter 1
Introduction

1.1 Introduction

More than half of the electrical energy produced in industrial countries is utilized by electric motors, over 90% of which are induction motors [1], [2]. Mainly because of their energy efficiency and inherent flexibility for controlling industrial processes, variable speed AC drives are now commonly used for controlling the speed of the motors. Decreasing the footprint of the motors is desirable for numerous applications, such as in electric motor-driven ships, where space is at a premium.

To produce a sinusoidal output voltage waveform with controllable magnitude and frequency to control the speed of induction motors, a pulse width modulated (PWM) voltage source inverter (VSI) is one of several available techniques. The use of these drives for motor speed control has far greater benefits than earlier methods, yet from an early stage, various types of motor failures and operating issues have continued to occur. Problems include premature insulation and mechanical (bearing) failures, electromagnetic interference, acoustic noise, and torsional vibration. The worse being their adverse effect on the machine insulation, which is due to the high frequency component of the PWM pulses and causes electrical and thermal stresses as well as faster aging. Operating these machines at a higher fundamental frequency than they are designed to operate (i.e., normal power frequency) is another reason for the increased rate of failures. Thus, fast repetitive PWM pulses with higher frequency impose stress on insulation systems that may lead to premature winding failure and forced machine outages [3]–[6].

In order to design a motor insulation system that can withstand the stresses produced by PWM drives, there is a need to study the behaviour of existing insulation under high frequency PWM waveform stresses, which will then enable a modification of insulation for PWM-driven motors. Such investigations will also provide a basis for the development of suitable test standards that will contribute to ensuring long-term operation of PWM-driven motors. Previous work has focused on the stress grading aspects of form-wound motor coil insulation [2], [7]–[9]; however, the focus of this research is on turn-to-turn insulation of form-wound motor coil insulation.

1.2 Insulation System of AC Machines

For over a century, induction machines powered the industry with their robust and reliable performance. The motors are composed of a rotor and a stator, the latter which is the stationary part of the machine and consists of coils that form three-phase windings placed in the slots of the core.

Motors are usually divided in two categories: low and medium voltage. As their name implies, low voltage motors operate at low voltage and have a terminal voltage of less than 690V. These types of motors normally also have a stator that is randomly wound. Random-wound stator coils are typically magnet wires placed in the stator slots in a random manor to form a full coil, the location of each strand of which is not fixed. According to IEC standard 60034-18-41, this type of insulation is also known as "Type I" insulation and is not intended to withstand partial discharge (PD) over its operational life [10].

The second category of motors is the medium voltage type that has a voltage rating of between 690V and 13,800V. The stator slots of these motors are filled with coils made in factories on a form; hence, the term 'form-wound'. Form-wound coils are made of mica-resin-based insulation on firm rectangular-shaped magnet wires configured according to the stator slot dimensions, and with insulation applied and designed to be fixed in the stator. This type of insulation is known as "Type II" in the IEC standard 60034-18-42, and PD is allowed to occur throughout the operational life of medium voltage motors [1].

Figure 1.1 shows random- and form-wound stators, illustrating the two types of insulation systems. The insulation system for each coil mainly includes ground-wall insulation, phase-to-phase insulation, and turn-to-turn insulation. Form-wound coils above 6.6 kV generally have additional stress grading, which is shown as (e) in Figure 1.1b.

Numerous studies have tackled the problems of low voltage machines with random-wound insulation fed by PWM drives; the issues are not only well understood but have already been extensively addressed. On the contrary, very few studies have been reported on form-wound machine insulation, in the specific the turn-to-turn insulation. IEC Standard 60034-18-42 is being developed to test the turn-to-turn insulation without having a sufficient basis for specifying the important test parameters. In the above context, the focus of the present research is on the turn-to-turn insulation of medium voltage machines with form-wound coils. The following section describes various insulations that are used in the coils.

a phase insulation / overhang insulation   1 phase to phase
b ground insulation   2 phase to ground
c turn insulation   3 turn to turn

a phase insulation / overhang insulation   1 phase to phase
b ground insulation   2 phase to ground
c turn insulation   3 turn to turn
d corona protection shield
e stress grading region
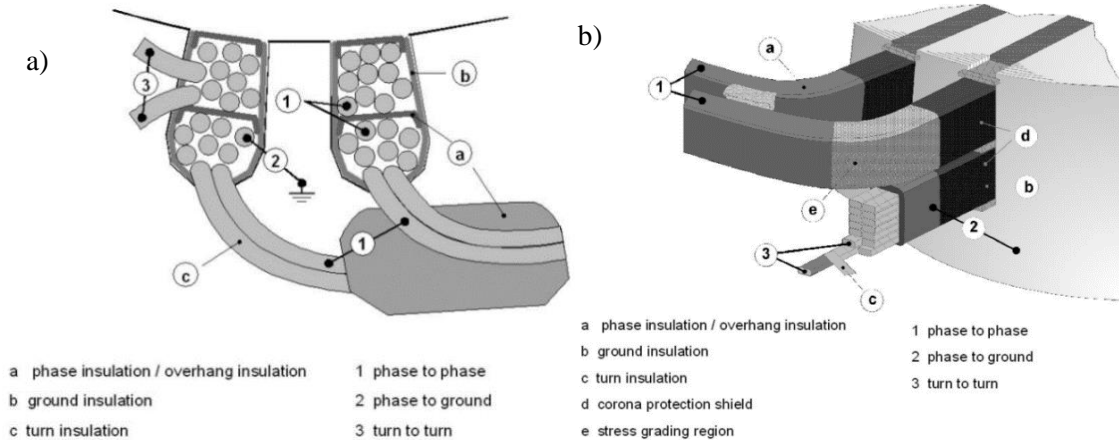
Figure 1.1. Illustration of motor stator windings: (a) random wound or Type I insulation, (b) form-wound or Type II insulation.

1.2.1 **Ground Wall Insulation**

The task of this insulation is to protect the energized coil from the iron core of the stator. The insulation is made of several layers of resin-rich mica-glass tape over the entire coil, as shown in Figure 1.1b. Thick layers of insulation make this system robust and resistant to PD discharges over decades of operation.

Full form-would coils, produced by the General Electric company in Peterborough for testing (Figure 1.2), were aged using high voltage PWM and conventional power frequency stresses to compare the relative performance of the ground wall insulation under both stresses. Accelerated aging of these coils for more than 1,000 hours under PWM stress showed that there is no significant change in the life compared to conventional stress. This finding confirms the robustness of the applied insulation system and is therefore of no concern to long-term operations under PWM waveforms.
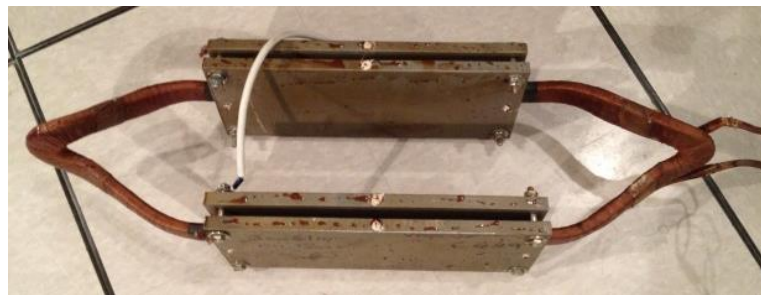
Figure 1.2. Photograph of a form-wound coil with simulated stator for testing.

3

1.2.2 **Stress Grading System**

Stress grading is used in motors operating above 6.6 kV to grade the electric field at the slot exit, thereby suppressing PD. Although it was well developed and designed for conventional power frequency stress, the stress grading system showed weakness under PWM stress due to the steep front waves emanating from PWM drives. This problem was studied and addressed in previous research at the high voltage engineering laboratory at the University of Waterloo [2], [11] as well as by other research groups [12]–[14].

1.2.3 **Turn-to-turn Insulation**

Turn-to-turn insulation prevents electrical shorting of the turns in coils. Conventionally, the voltage drop on each turn is only a few volts increasing to kilovolts under transient surges entering the machine. As a result, the insulation design of the turns has been based on occasional overvoltage surges. However, for machines that are fed from adjustable speed drives (ASD), steep wave surges occur at the operational frequency of the PWM drives, which are in the range of 2 kHz. These fast transients have to be considered in the design of the machine insulation, otherwise the machine will experience premature failure. The amplitude of these transients can be exceedingly high, as the fast transient impulse voltage is not evenly distributed along the series-connected coils of a stator leg, resulting in a high voltage stress appearing mainly on the first turn of the first coil. Wheeler investigated this phenomenon by applying pulses with different rise times and measuring the voltage drop at the first turn of a coil (Figure 1.3) [15]. As can be seen, faster rise times result in a higher voltage drop on the first turn. For example, a surge having a 200 ns rise time will have approximately 95% of terminal voltage dropped along the first turn.

In addition, the impedance mismatch between the cables connecting the converter to the motor can result in traveling waves with an overshoot on the voltage waveform. The overshoot is a function of the rise time of the pulse and length of the cable, as shown in Figure 1.4. As reported by Wheeler [15], the voltage overshoot can be as high as 100% for a surge having a rise time of 50 ns and a cable length of 4 metres. The overshoot is lower for surges with slow rise times; for example, 20% for a 1µs rise time surge with the same cable length [15].

4
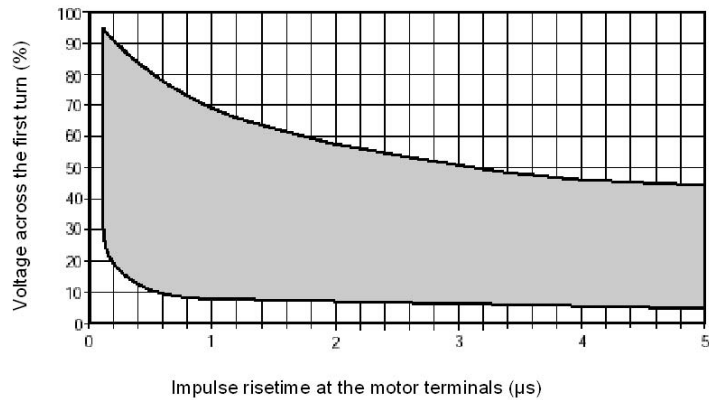
Figure 1.3. Voltage across the first turn of a coil as a function of surge rise time (the gray area indicates the range of voltage drop for different pulses) [15].
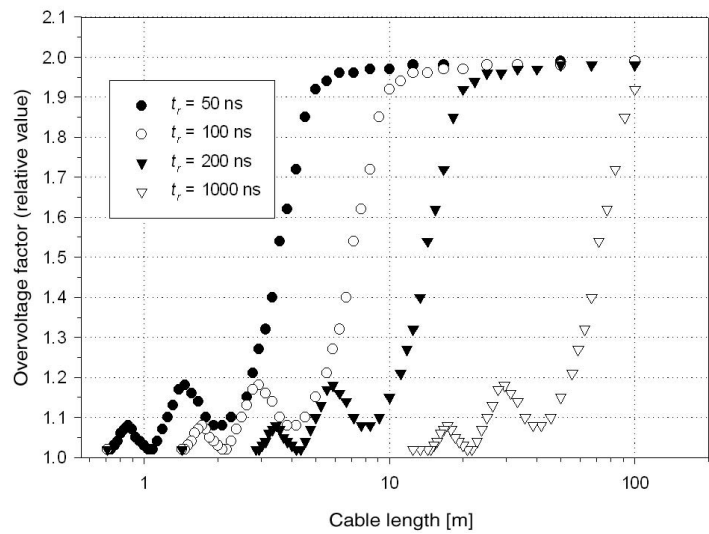
Figure 1.4. The effect of overshoot on the motor terminal due to travelling waves on the cable connecting the converter to the motor as a function of surge rise time and cable length, from Wheeler [15].

   Although filters at the motor terminals can be used to attenuate transient surges, this is not always desirable as they must be custom designed for each application, and are often bulky and quite costly for some applications (e.g., electric ships). Therefore, turn insulation design considerations have to be taken into account in order to withstand such stresses.

5

1.2.3.1 Turn Insulation Material Used in Form-wound AC Motors

There have been many studies and developments in random-wound motor wire insulation. These have concerned mainly the type of enamel and the use of nano-sized fillers to impart improved resistance to PD, including previous research work performed at the University of Waterloo [16]–[20] on enamel wires fed by converters. However, few studies have addressed the issue of form-wound motor coils with rectangular copper strands insulated with various materials. The materials commonly used for turn insulation are outlined as follows:

a) Mica-Glass Turn Tape

Mica-glass turn tape is an integrated tape consisting of mica flakes supported by fibre glass tape. The tape is wrapped around rectangular wire that has been enameled and, after forming, is vacuum pressure impregnated (VPI) with epoxy resin.

b) Mica PET (polyethylene terephthalate) Turn Tape

This turn tape is a class F Samica® tape impregnated with a modified epoxy "B" stage binder, reinforced with two polyester films and a hot melt adhesive on the thicker film surface. The tape is known as Simicafilm® F290+, which is wrapped over bare rectangular copper wire.

c) Daglas®

Daglas® insulation consists of three layers of insulation on rectangular copper wire. The first layer is a quadruple-coated polyimide layer or enamel, the second layer is fused double glass fibre and polyester fibre, and the third layer is polyester varnish, respectively.

d) Enamel

Enamel turn insulation consists of a heavy coat of polyamide-imide over polyester or polyimide film on a rectangular copper strand.

1.3 Adjustable Speed Drives (Converters)

Adjustable speed drives (ASDs) became commercially available in 1970 as a replacement for gearboxes and eddy current clutches for medium voltage motors [21]. Due to their excellent efficiency, reliability, process precision and improved power factor, these converters continue to be in great demand [22]–[25]. The ARC advisor group, an industry analyst company, provided a market study forecasting the demand for the future. The anticipated growth of these drives to 2017 is 10% annually [26].

Figure 1.5 shows the three stages of an ASD. In the first stage, three-phase AC power conversion to DC takes place using diodes or thyristors; in the second stage, capacitors store the energy; and in the third stage, DC conversion to AC takes place by GTO (gate turn-off thyristor) or IGBTs (insulated-gate bipolar transistor) to AC by square pulses with constant frequency but different pulse widths that are proportional to the equivalent sinusoidal waveform amplitude. The technique is commonly known as pulse width modulation (PWM). The output waveform may have different levels depending on the topology and can be 2, 3, or 5 levels. Figure 1.6 shows a typical 2-level PWM ASD [26].
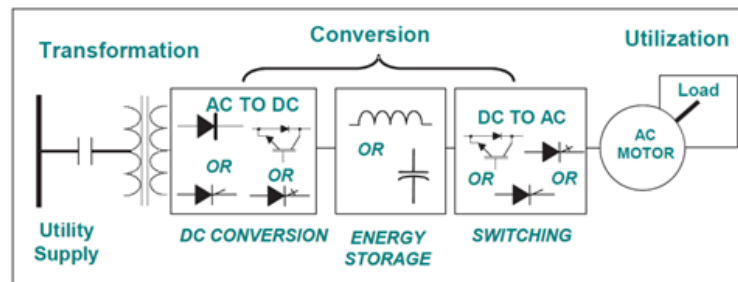
Figure 1.5. General schematic of an adjustable speed drive [26].
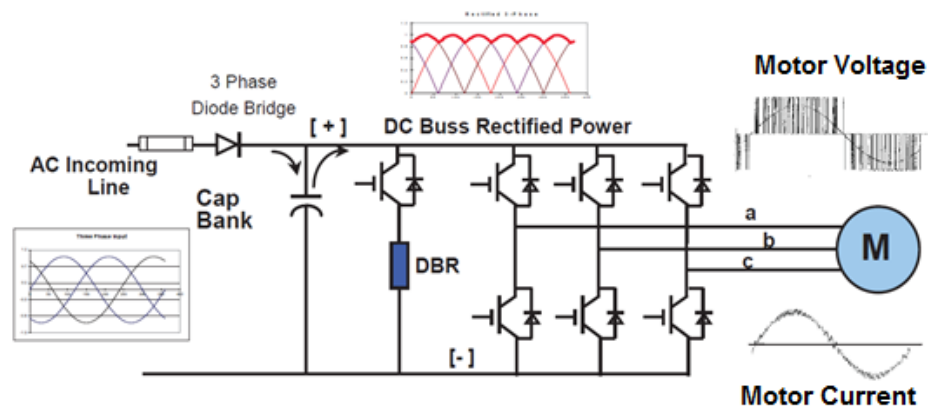
Figure 1.6. Example of a two-level PWM ASD [26].

As illustrated in Figure 1.7, the evolution of solid state devices for the converter has played an important role in ASD development. There has been considerable interest and continuous development and improvement in solid state technology to make switches with higher voltage rating, improved reliability and faster switching times, and this trend is expected to continue in the future. The above described voltage transients propagate into the machine, placing more of a burden on the insulation system of motors.

7
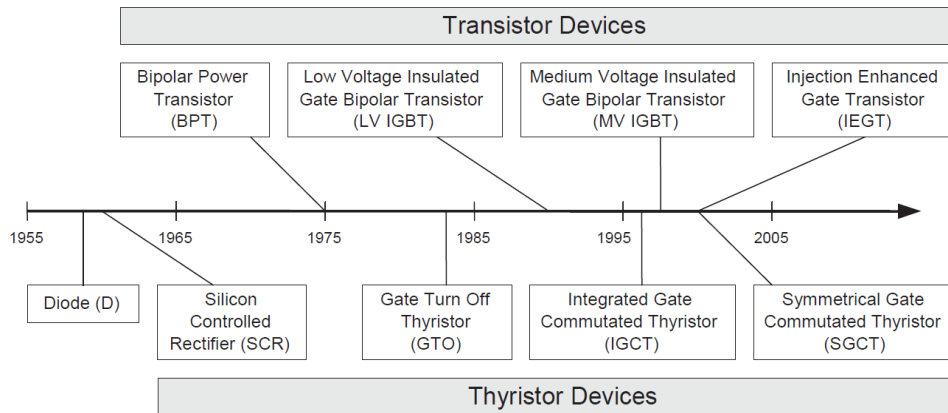
Figure 1.7. Development of power semiconductors over the past 35 years [26].

1.4 Literature Review

Numerous papers have been published over the past decade on the topic of PWM-driven machines. However, the majority of these papers have focused on the turn insulation of low voltage random-wound motors, whereas very few have studied form-wound turn insulation. Although the stress factors and therefore the aging mechanisms are different in form-wound motors [4], [5], [15], it is possible to apply some of the results obtained on random-wound machines or cable insulation, especially with fundamental aging phenomena such as partial discharge and space charge effects. Hence, the following review provides a summary of the applicable research on form-wound insulation, followed by related research on random-wound insulation.

Of the relevant literature, probably the most important is the IEC standard 60034-18-42 [1], which was updated in 2008 and is also currently under revision, which focuses on the problems of inverter-driven medium voltage motors with form-wound coils. This document has been developed based on field experience, suggestions of experts, and relevant research addressing the issues of aging. The standard lists the stress factors of inverter driven form-wound machines, as follows:

- Fundamental and impulse repetition frequency to the machine terminals.
- Peak-to-peak voltages of the fundamental and repetition frequencies as well as the jump voltages that are expected to occur at the machine terminals.
- The impulse rise time.

8

The standard also shows the significance of each parameter on different parts of the insulation, as provided in Table 1.1.

Table 1.1. Influence of features of the converter drive voltage on acceleration of aging of components of Type II insulation systems (from IEC 60034-18-42)

Insulation component	Fundamental frequency	Impulse repetition frequency	Fundamental frequency pk/pk voltage	Jump voltage	Impulse repetition frequency pk/pk voltage ($U'_{pk/pk}$)	Impulse rise time
Turn to turn insulation	○	●	○	●	○	●
Main wall insulation	●	○	●	○	○	○
Corona protection layer and stress grading	○	●	●	●	●	●

NOTE ○ Less significant ● More significant

As highlighted in Table 1.1, the impulse repetition frequency, jump voltage and impulse rise time are the parameters that enhance the stress on turn insulation. It is also suggested that a faster rise time increases the occurrence of partial discharge between the turns. Hence, inverter-driven turn insulation will age electrically, as opposed to non-inverter-driven or conventional operation of motors, where impulses occur occasionally and the aging mechanism is primarily thermal rather than electrical.
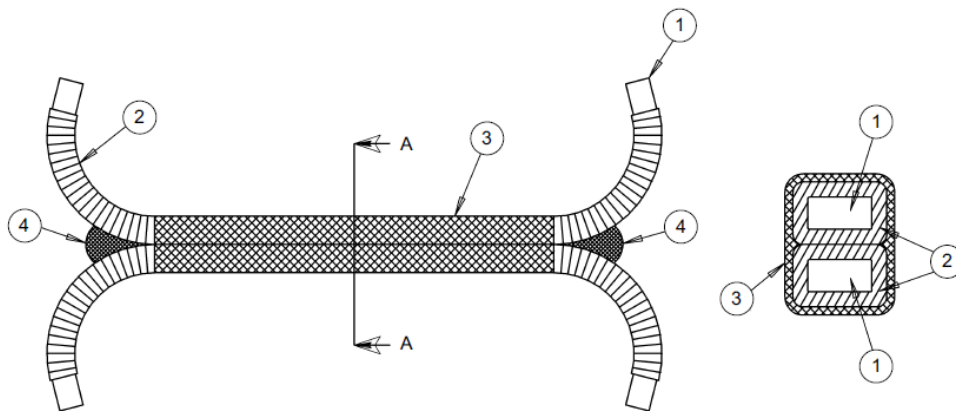
Figure 1.8. Preparation of turn insulation sample of form-wound motor copper conductor or strand (1) turn insulation (2); binding tape (3); and crotch filler material (4) [1].

The standard also provides a procedure to produce and test turn insulation samples of form-wound turn insulation. The test samples are formed from two rectangular copper wires or strands, with turn

insulation applied, and held together by a binding tape which is usually ground wall mica-glass tape. The ends of the strands are bent apart to avoid electric field enhancement at the ends. The space between the strands at the ends of the sample, defined as the crotch, must be filled properly to avoid PD at the crotch. Additionally, the samples must be vacuum pressure impregnated (VPI) with epoxy resin to exclude air pockets or bubbles in the samples, and the VPI process must be done in the same way that form-wound coils for motors are manufactured. The sketch in Figure 1.8 illustrates the construction of a turn insulation sample.

Over the past few years, many publications have either supported or challenged the standard [4]–[6], [15], [27]. Chen et al. [27] reported on experiments on different form-wound insulation components such as turn insulation, ground wall insulation, and stress grading to support the IEC standard. Enamel- and mica-insulated samples were prepared and aged at power frequency and PWM stresses. It was reported that the enamel insulation has a reduced life under PWM stress, while mica insulation exhibits similar lifetimes under power frequency and PWM stresses, primarily due to the PD resistance of mica (Figure 1.9). However, the authors did not provide sufficient details of the test conditions on types of insulation materials that were evaluated (more than 5); in fact, only two were reported.
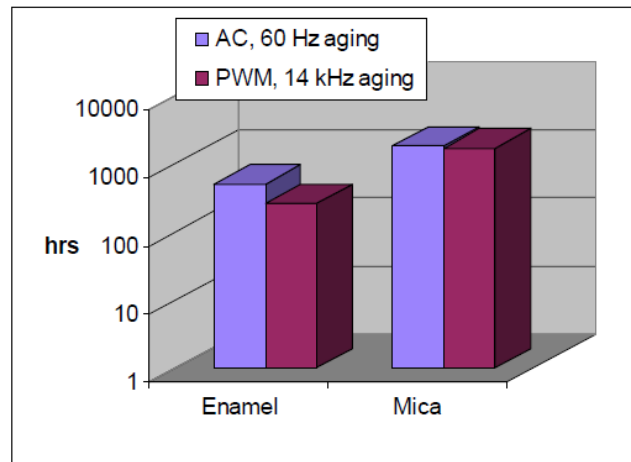
Figure 1.9. Times-to-failure of various insulation materials under power frequency and 14 kHz PWM waveform stresses [27].

Luo et al. [28] investigated the times-to-failure and microscopic structure of form-wound turn insulation comprised of Dupont Kapton® 100CR film containing nano-sized filler. In their research, a bipolar square waveform with a frequency of 10 kHz, a peak voltage of 1750 V, and a rise time of 1µs was applied to the insulation samples. A high frequency current transformer (HFCT) and a personal

10

computer (PC) were used to detect and record PD. It was observed that the number and magnitude of PD increases with aging time. In addition, they reported the phase dependence of the PD, initially between 5 and 15° but increasing to 20° with higher amplitudes after 100 hours of aging. As a mechanism, it was suggested that with aging, the voids increased in size due to PD, resulting in a higher partial discharge inception voltage (PDIV) and causing a delay in the occurrence of PD. Furthermore, at higher voltages, higher PD magnitudes occur. Scanning electron microscopic (SEM) analysis was done on the samples, concluding that the organic materials are eroded by the PD, leaving behind nano-sized filler particles that form a layer and thereby protect the insulation material.

Manns et al. [29] examined the life of form-wound turn insulation made of epoxy-mica insulation. The frequencies of 60 Hz, 418 Hz and 10 kHz with sinusoidal waveforms were used in their studies. Using Weibull distribution parameter analysis, no difference was found between the three frequencies in terms of the number of cycles to failure. The rise time for a 10 kHz sine wave is 25 µs, and at the test voltage of 7 kV, the 280 V/µs rise time is relatively slow. The results would support the low significance effect of the fundamental frequency on turn insulation aging in the IEC standard. However further studies are required using PWM pulses with faster rise times.

Fabiani et al. [30] carried out similar research on four different twisted enamel wires. Partial discharge inception voltage (PDIV) was recorded when different waveforms were applied considering 50 Hz, 1 kHz and 10 kHz square pulses, both unipolar and bipolar forms. The results showed that the PDIV is not a function of frequency and unipolar waves have a PDIV higher than twice that of the bipolar ones, as shown in Figure 1.10a. On the other hand, the magnitude of the PD as well as the delay in the PDIV increases with increasing frequency when a voltage equal to PDIV is applied, as illustrated in Figure 1.10b. It was suggested that charges accumulated on the electrodes rather than penetrating the insulation resulted in higher stresses at higher frequencies. A lower penetration of charges into the insulation was confirmed, especially for bipolar pulses at higher frequency rates using a pulsed electro-acoustic (PEA) technique to measure space charge accumulation (Figure 1.11a). Assuming that higher PD magnitudes contribute to faster aging, these results contradict those of Manns et al. [29], suggesting that the repetition frequency is not of concern, which may be due to the mica-based material used in [29]. In the work of Fabiani et al., the low rate of rise (<5 kV/µs) was suggested as the possible reason for the independence of PDIV with respect to the frequency. Another interesting result is the difference between bipolar and unipolar waveforms, in which the PDIV was reported as more than twice for

11

unipolar cases. These results suggest that PDIV is a function of peak-to-peak of the test voltage, even when comparing low rise times such as 50 Hz sinusoidal and 50 Hz unipolar square wave.
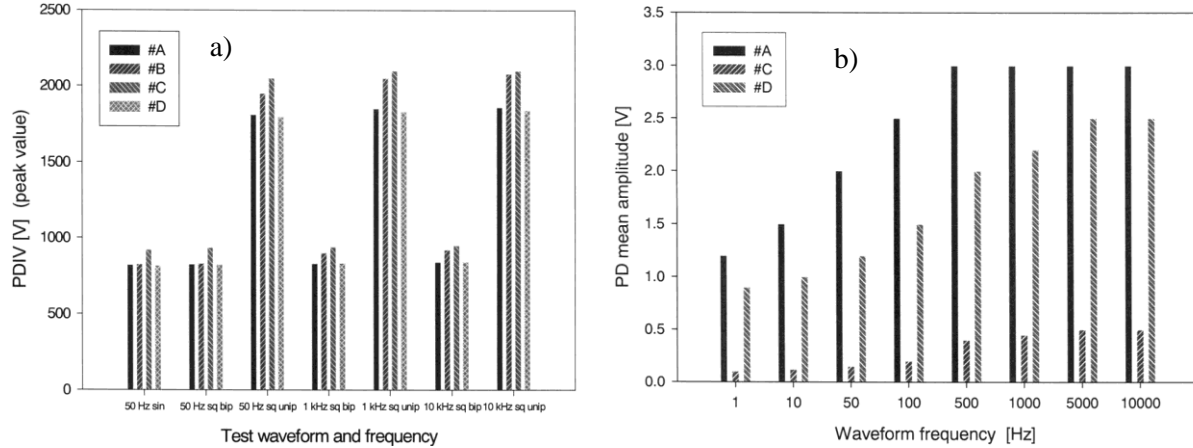
Figure 1.10. Behaviour of PDIV (peak value) with test waveform and frequency for four tested materials, #A, #B, #C, #D, in (a); and PD mean amplitude per period (V) as a function of frequency for bipolar square and amplitude PDIV, for tested materials, #A, #B, #C, in (b), [30].

Fabiani et al. also described theoretically to relate space charge to electric field. In the presence of space charge in the material, the electric field in the air gap adjacent to it will be enhanced. A formula relating electric field to the charge accumulation in the bulk and interface of insulation and air was presented.

The effect of interfacial space charge accumulation on PDIV is another topic that was tackled by Fabiani et al. It was suggested that the interfacial field reduces the electric field in the voids, consequently increasing the PDIV. Interfacial polarization and charge accumulation in the bulk of the insulation may have an opposite effect on PDIV, e.g., the former increasing and the latter decreasing the PDIV. Their theoretical deduction was supported by applying a square wave with an amplitude of 0.5 PDIV level for various times and measurements of the PDIV (Figure 1.11b). They related the initial increase in PDIV to the presence of interfacial polarization and homo-charge accumulation, and the subsequent decrease in PDIV to charges that penetrated deeper into the bulk of the insulation.

On the other hand, Florkowska et al. [31] reported contradicting results. The effect of rise time and frequency of a square waveform stressing ethylene-propylene rubber (EPR) was investigated. The surface PD activities took place on a sheet of EPR placed between rod-plane electrodes. A low resistance CT and antenna to capture PD was used. It was observed that higher frequencies and faster

rise times exhibit lower inception voltages, as shown in Figure 1.12a, which is opposite to that reported in [29] and [30]; nonetheless, the rise times studied are in a similar range calculated between 1 to 4.5 kV/µs. It was also demonstrated that the magnitude of PD is higher at faster rise times, suggesting faster aging under fast rise times, as shown in Figure 1.12b. In addition, it was reported that both higher switching frequency and faster rise times resulted in lower time to inception. This is completely opposite to what was published in [30], where an increase in the inception delay with increased frequency were observed. Considering such contradicting results, it is necessary to investigate such behaviour for form-wound insulation.
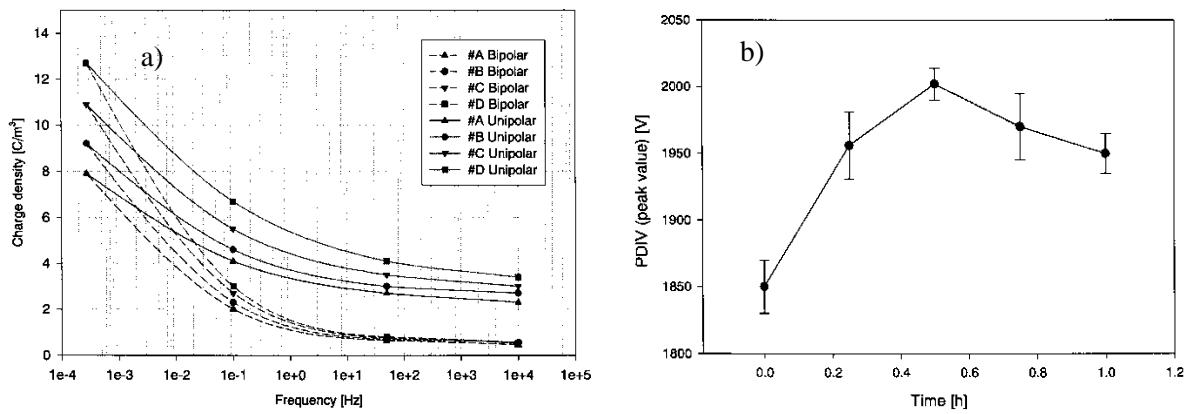
Figure 1.11. (a) Charge accumulation behaviour with frequency for various materials for unipolar and bipolar supply waveform. Experimental points on the left are relevant to DC tests having polarization-depolarization time of 7200 s. (b) Behaviour of PDIV with poling time for an unipolar square wave at 50 Hz (poling voltages of 0.5 PDIV) [30].
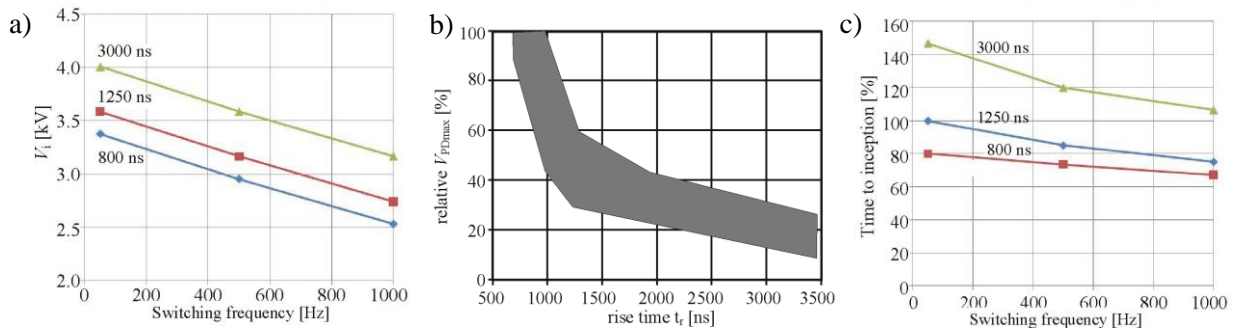
Figure 1.12. (a) Effect of switching frequency on inception voltage for different rise times; (b) effect of rise time of PD magnitude; and (c) effect of switching frequency on time to inception of PD for different rise times [31].

Lindell et al. [32] investigated the effect of rise time on the extinction voltage of various insulation systems, namely, corona in the air, twisted wires, and turn-to-turn insulation in oil. Their PD measurement system was comprised of a coupling capacitor with a series resistor and a National Instruments ADC (Analog to Digital Converter) to record the waveform. The number of PDs in each period was related to the applied voltage. The rise time was found to be an effective parameter for the twisted pair where the extinction voltage was lower at faster rise times, matching the results reported in [31] for sheet material. However, no effect of rise time for turn-to-turn insulation in oil was observed. Square waves with 2 and 100μs rise times and peak voltages between 1 kV and 8 kV were used. PD took place at each switching event as well as at steady state, with a delay in corona in air samples, while it mostly occurred on switching for twisted wires with smaller PD magnitude at steady, and finally at the steady part with a long delay of several milliseconds for the turn-to-turn sample in oil.

Wu et al. [33] investigated the effect of aging time on PD magnitude and behaviour for square wave and AC. CIGRE samples [34] and a balanced bridge with ideal and non-ideal samples was used to detect PD. The rise time of the square pulse was 0.4 kV/μs. It was reported that there is no change in PD behaviour during aging time for both AC and square, which agrees with the results of [29] and contradicts those in [31]. The authors explained the occurrence of more than one PD at the rise time of the applied voltage to the surface area of the void.

Fabiani et al. [35] studied times to failure of enamel samples under 50 Hz and 10 kHz sinusoidal waveform. Three different materials were considered, including PD resistant enamel and tested in air (in which PD occurred) and in oil (in which PD did not occur). It was concluded that the life of the samples is lower even in the absence of PD at high frequencies, which was also reported by [16]. Voltage and switching frequency were listed as the dominant factors of aging. No significant effect was found relating rise time to aging in the studied range of rise times <1 kV/μs, which is relatively a slow rise time. A life calculation formula was used to estimate the voltage endurance coefficient and five samples were considered for each test at three or more voltage levels in order to obtain a life model for each test condition.

Wang et al. [36], [37] investigated the effect of rise time of square waves on single-point contact crossed pairs [38]. An RF antenna and high pass filter along with computer processing were used in order to detect PD. The samples were stressed with pulses, having a peak value of 2.5 kV and rise times ranging between 200 ns and 400 μs. It was reported that the magnitude of PD will increase with faster

rise times, as shown in Figure 1.13a. This result matches those in Figure 1.13b reported in [31]. On the other hand, PDIV was observed to increase at faster rise times (Figure 1.13b). This means that the PDIV is higher at faster rise times, which is completely opposite to that reported in Figure 1.12a in [31], [32] for the extinction voltage.
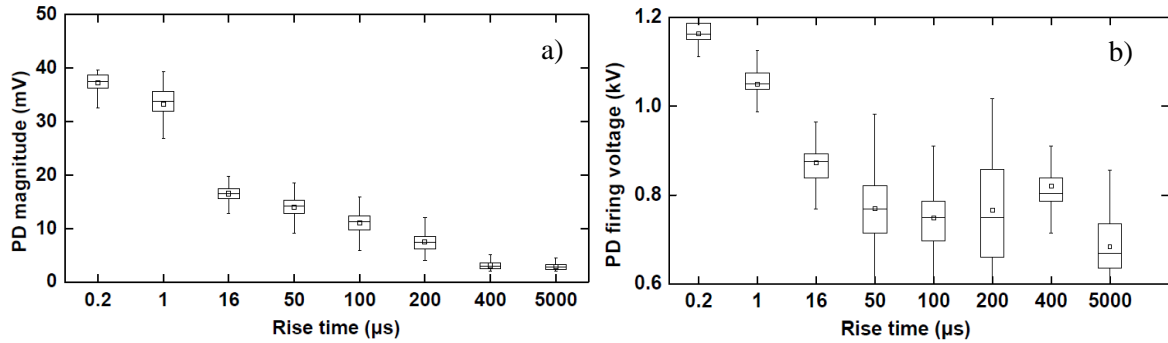
Figure 1.13. (a) PD magnitude verses rise times; (b) PD firing voltage (PDIV) verses rise times [36].

The energy of the PD spectra at different rise times was measured. It was reported that at faster rise times the energy of PD spectrum is higher, as shown in Figure 1.14. PD has significant energy in the range of 1 to 1.7 GHz (rise time equal to 200 ns) with rise times between 0.2 and 16µs for 0.4 to 0.7 GHz and 50 to 400µs for 0 to 0.7 GHz.
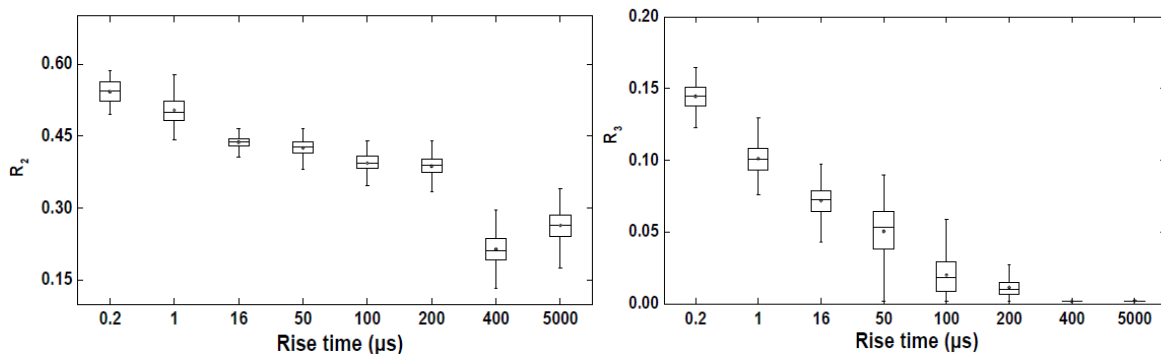
Figure 1.14. Energy ratios R_2 (total energy in frequency range of 0.6 to 1.2 GHz) and R_3 (total energy in frequency range of 1.2 to 1.8 GHz) as a function of rise time [36].

Yin [39] showed that samples of twisted wire turn insulation fail faster under square wave stress with faster rise times, as shown in Figure 1.15. Bipolar square waves of 20 kHz with a peak-to-peak voltage of 4 kV and 0.04 to 0.1 µs rise times were used to conduct the study. Accumulative dielectric heating was reported as the main reason for the shorter lifespan when stressing using faster rise times.

15
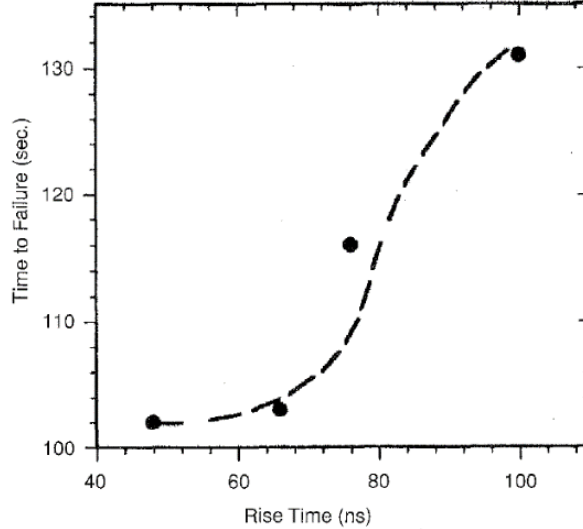
Figure 1.15. Time-to-failure verses rise time for enamel twisted samples stressed using bipolar square wave with applied peak-to-peak voltage of 4 kV [39].

Yin also used bipolar and unipolar square wave pulses, a 2 kV peak voltage, a 20 kHz switching frequency, and a 25 ns rise time to age twisted enamel pairs. It was reported that the greatest reduction in the time-to-failure of the samples was produced by the bipolar waves, with a smaller reduction achieved using negative unipolar waves, followed by that obtained with the positive unipolar waves, as illustrated in Figure 1.16. The reason given for the shorter failure time with the bipolar pulses was higher intensity PD, but the longer time-to-failure under unipolar pulses was attributed to the presence of a counter electric field arising from the accumulated space charge. When bipolar waves were applied, the electric field of the space charge aligned with the applied external field, and when the polarity reversed, increased PD occurred, which is in agreement with [30]. In this case, it was assumed that the time required for the rate of charge to dissipate was less than the transient time of the wave. It was concluded that the increase in the space charge under the positive pulses limited the electric field and resulted in a longer time-to-failure than when negative pulses were applied. The authors also reported a threshold in the switching frequency after which the degradation rate of the insulation increased, as shown in Figure 1.17. It was suggested that, above a switching frequency of 5 kHz, a different mechanism that affects aging leads to a shorter time-to-failure than expected when only the number of cycles to failure is taken into account.

16
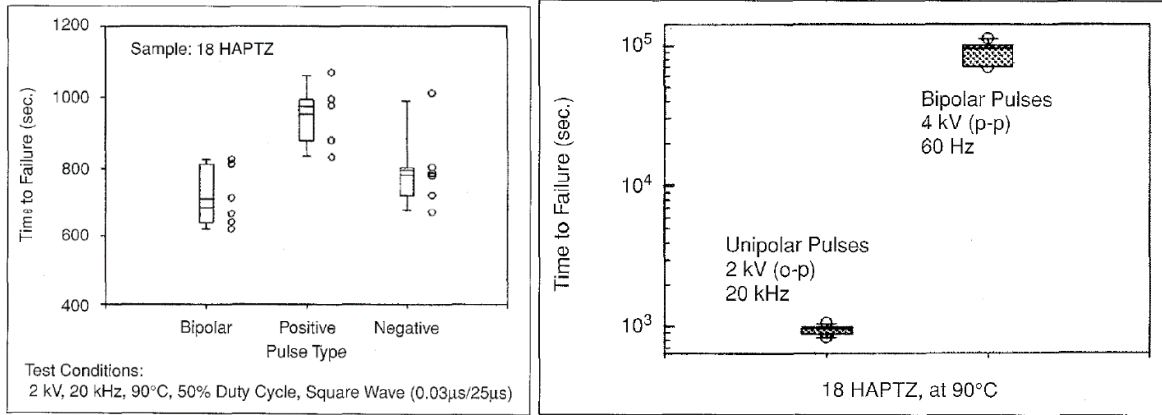
Figure 1.16. Time-to-failure verses pulse type [39].
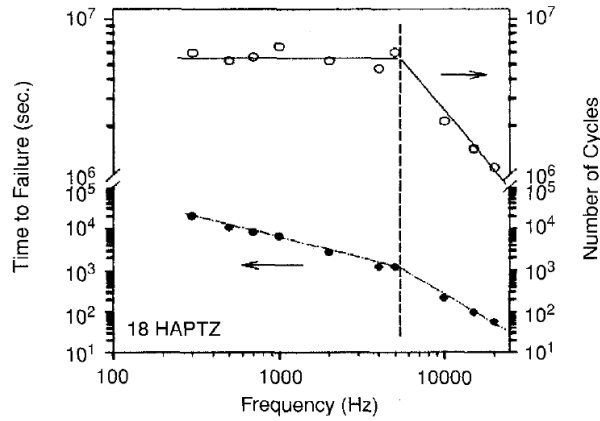
Figure 1.17. Pulse frequency dependency on time-to-failure and number of applied cycles [39].
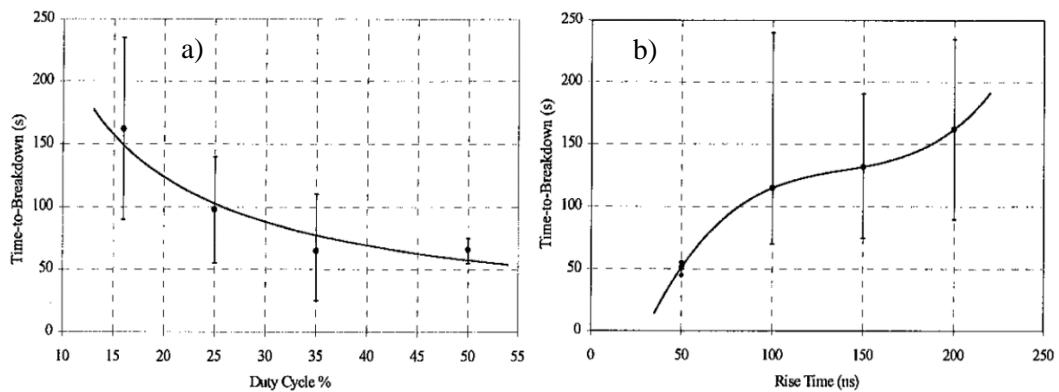
Figure 1.18. Time-to-failure examinations for different rise times in a), and duty cycles in b).

17

Grzybowski et al. [40] also reported faster times-to-failure with faster rise times when stressing twisted enamel samples under square waves having rise times ranging between 50 ns to 200 ns (Figure 1.18a). As illustrated in Figure 1.18b the higher duty cycles resulted in shorter times-to-failure.

Bellomo et al. [41] investigated the effect of the square wave types (unipolar/bipolar) on the time-to-failure of Kapton® sheets between parallel plates. It was reported that unipolar waves resulted in a shorter time-to-failure, contradicting the results published by Yin et al. [39]. It was speculated that PD under unipolar waves is controlled by the mobility of the charge carriers through the bulk for unipolar waves and on the surface with bipolar waves. When sinusoidal waves were used, no significant changes in time-to-failure were observed for frequencies ranging from 500 Hz to 2500 Hz.

Kaufhold et al. [42], reported longer time-to-failure with unipolar than with bipolar waves when stressing two parallel enamel samples held together by VPI resin, using 0.1/5 μs impulses at a 5 kHz frequency. Fabiani et al. [43] also showed a longer time-to-failure with unipolar than with bipolar waves for twisted enamel samples stressed by square waves at a 10 kHz switching frequency.

Ul Haq [16], [17] studied the effect of the repetition rate of steep front impulses on the time-to-failure of enameled form-wound turn insulation. The time-to-failure was found to decrease when the impulse repetition rate increased, with a steeper reduction slope for repetition rates above 500 Hz. This change in the aging mechanism was attributed to the accumulation of the space charge at higher frequencies, which contradicts the results reported in [39].

It is evident from the above literature that there are both contradicting and supporting results on the effect of different parameters such as rise time and switching frequency on PD behaviour and aging of the insulation , which thus necessitate further investigations on the subject.

Humidity and temperature are additional parameters that can modify an electric field in a system and affect PD activity. Nawawi et al. [44], [45] investigated the effect of humidity on PD using the CIGRE test cell. It was reported that the increase in humidity had no effect on partial discharge inception voltage (PDIV), but it decreased the surface resistivity and therefore the charge accumulation. Discharge time lag and PD amplitude were reported to decrease with increased relative humidity. On the contrary, Waldi et al. [46] reported increasing PD magnitude with increased relative humidity. Centurioni et al. [47] in another research showed that the accumulated charge on the surface is lower at higher humidity levels, which is in agreement with [44], [45]. Fenger et al. [48] suggested that absolute humidity rather than relative humidity must be considered when evaluating the effect of

humidity on PD. It was reported that PDIV increased with increased absolute humidity and that there would also be an electric field enhancement due to condensation. Kikuchi et al. [49] showed a decrease in PDIV with increased absolute humidity at low temperatures on twisted wire stressed using 60 Hz sinusoidal voltage. However, at higher temperatures, PDIV showed an opposite trend and was observed to be increasing in higher absolute humidity levels. It was speculated that the water droplets absorb free electrons at higher temperatures, which causes PDIV to rise. Soltani et al. [50], [51] investigated the effect of humidity on machine insulation using an asphalt coil and epoxy bar. They reported that humidity amplifies internal discharges while slightly decreasing surface discharges. The PDIV was also reported to increase with increased humidity [51].

In all of the reported works, PD plays a significant role in the aging of turn insulation under square wave stress. Hence, the detection of PD is of great importance to these studies. Conventional PD measurement under AC waveform can be easily done by monitoring the current and applying a simple filter-rejecting power frequency and its harmonics while retaining the PD pulses, which is not the case when square-like waveforms are present. This is due to the large capacitive current in the insulation generated by the application of fast rise time voltage pulses, which is much greater than PD pulses and makes it quite difficult to detect PD. The following paragraphs briefly present several methods used in the literature to detect PD under square waves.

Using an antenna is probably the most popular method for detecting PD under pulsed waveforms where the capacitive current of the sample can be ignored. By selecting an appropriate range of frequency, it is possible to disregard the effect of the supply pulses. This method has been used by several researchers [30], [31], [36], [43].

Cavalini et al. [52], [53] used an antenna embedded in a low voltage three-phase inverter driven motor to detect PD. Using a high pass filter in which the inverter interference signal was filtered-out, a good signal-to-noise ratio was achieved.

A high frequency current transformer (HFCT) [28], [54] was used to measure the current waveform and transferred it to a data acquisition system consisting of an analog-to-digital card (ADC) in a personal computer (PC). Post-processing software was used to disregard the supply current, retaining only the PD pulses. This technique may, however, fail to detect PD at fast rise times due to similar frequency components of supply current and PD current.

Using shunt resistors instead of HFCT is another method for detecting PD, but again, the method may suffer limited detection similar to the HFCT method [31], [32].

Wu et al. [33] used a balanced bridge with ideal (with no voids) and non-ideal (with voids) samples to cancel out the capacitive current of the sample, and then used ADC to transfer the detected pulses to a PC.

1.4.1 Summary of Literature Survey

The above discussion on literature can be summarized as follows:

- PD is an important aging factor which is mainly governed by the applied voltage, and a higher applied voltage results in a higher PD repetition rate.
- Higher switching frequency accelerates the aging in enamel twisted wires and cable insulation.
- PD magnitude increases with increased switching frequency.
- There are contradictions in the relationship between PDIV and the switching frequency, which in one work was reported to be constant, while in another it decreased as the switching frequency increased.
- Mica-based insulations are reported to be independent of switching frequency.
- Charge accumulation is a function of switching frequency, which has been reported to decrease with increased switching frequency. Furthermore, the accumulation from a unipolar waveform is higher than that of a bipolar waveform.
- Time-to-inception of PD is a function of switching frequency that may change with aging; however, there are contradictions in the reported trend.
- Faster rise times result in higher PD magnitude, but there are inconsistencies in reporting the effect of rise time on PDIV and on time to inception.
- The energy content of PD for different rise times is reported to be different.
- Humidity increases PDIV, but there are some contradiction in the results reported.

PD measurement in the presence of steep front voltage pulses is done using antenna, HFCT, shunt resistor, and balanced bridge. Extra care should, however, be considered when rejecting the supply waveform signal to avoid measurement errors.

From the presented literature review, it is obvious that there are contradicting results reported on the PD behaviour as well as insulation aging respect to the applied aging parameters such as rise time,

20

switching frequency, and pulse type. Moreover, some of the reported results are specific for random-wound insulation which may not be necessary applicable to the form-wound insulation. Hence, conducting the research in this context to address the existing issues has a great benefit.

1.5 Aim of Present Work and Thesis Organization

Current PWM-VSC drives are introducing new voltage stresses to the ground-wall and turn insulations of form-wound coils of medium voltage machines. Moreover, as advances in solid state switching technology develop devices with higher voltage ratings and faster rise times, higher voltage stresses are expected in the future. However, due to the robustness of the ground-wall insulation, the industry has identified turn insulation as the critical component affecting the life of the machine's insulation. Hence, understanding the mechanisms of aging of turn insulation under PWM-VSC surges has great importance.

This research focuses on obtaining a better understanding of the aging mechanism in turn insulation of form-wound coils under steep-front square pulses. The main objectives of this thesis are as follows:

- Design and development of test facility including test samples, high voltage pulse generators, PD measurement system, and charge measurement system to study machine turn insulation.
- Evaluate the relationship between pulse parameters and aging factors of turn insulation using measurements and statistical analysis, which will contribute to addressing the existing conflicts and to developing a standard test method.
- Contribute to the IEC standard by improving the construction of turn insulation samples.
- Provide a thorough understanding of the failure mechanisms of turn insulation by relating fundamental studies to the times-to-failure of turn insulation samples to address existing issues.

The thesis is organized as follows. Chapter 2 presents the development of the test equipment and also describes the material and methods used in the study. The design and implementation of the developed equipment are presented, including the high voltage unipolar PWM generator, the bipolar/unipolar square wave generator (along with the protection system and the aging setup), the PD detection system, the surface charge measurement system, back-to-back insulation samples, and point-to-plane setup with insulation film. The surface potential measurement and surface resistivity evaluations are described. Numerical analysis using FEM for the estimation of field distribution for both back-to-back and point-to-plane setup is also described.

Chapter 3 presents the results of time-to-failure experiments of back-to-back samples for various pulse parameters when stressed using square waves. In addition, the results of examining PD features and surface charge accumulation for various parameters such as pulse frequency, pulse type, temperature, and humidity on point-to-plane setup using different insulation samples are presented.

The results obtained in the previous chapter are discussed in Chapter 4. The times-to-failure examination of back-to-back samples, fundamental studies under point-to-plane setup, and FEM simulation are employed to explain the failure mechanism and identify the main factors affecting the insulation lifespan.

Chapter 5 provides a summary of the work along with a conclusion, and suggests potential directions for future works.

Chapter 2

Equipment Design, Materials, Methods and Modeling

2.1 Introduction

This chapter introduces the design and implementation of the methods and equipment that are developed throughout the research as an important contribution of the present work. These systems include the modification of an HV unipolar generator, the design and implementation of a unipolar/bipolar HV generator, the design and implementation of a PD detector compatible with HV PWM interference, the design and modification of back-to-back turn insulation samples, and the design and implementation of a point-to-plane setup with film insulations barrier and a surface charge measurement system. The materials, methods, and apparatuses used to conduct the measurements for both the turn insulation samples and point-to-plane setup are also described. The last part of the chapter presents the FEM modeling parameters and characterizations.

2.2 High Voltage Unipolar PWM/Square Wave Generator

The developed design uses a Marx generator configuration in which the capacitors are charged in parallel and are discharged in series. Figure 2.1 shows a simplified schematic of the design for multiple stages. The benefits of this design include cascade-ability and a smaller DC input voltage. The generator was developed previously [55] but was modified to enhance its performance in the present research.

The maximum voltage capability was improved by optimizing the circuit parameters. The reliability of the system was also improved, providing the capability to run the generator continuously without internal failures. The generator was used for aging tests lasting thousands of hours.

The generator is capable of generating unipolar PWM waves up to 4 kHz switching frequency and unipolar square waves up to 8 kHz switching frequency, with adjustable output voltage between 0 kV and 20 kV peak. The duty cycle of the square wave is also adjustable between 15% and 85%. The rise and fall times are dictated by the capacitance of the load and can be slowed down by the use of series external resistors. The rise time is typically in the range of 100 ns to 300 ns depending on the load, while the fall time is longer and ranges between 3 μs and 5 μs. Figure 2.2 shows the schematic of the generator for two stages in which capacitors C_1 and C_2 are charged in parallel through diodes D_1 and

D_2 when charging switches SW_1 and SW_2 are on. Figure 2.3 shows the equivalent circuit during the charging and discharging cycles.
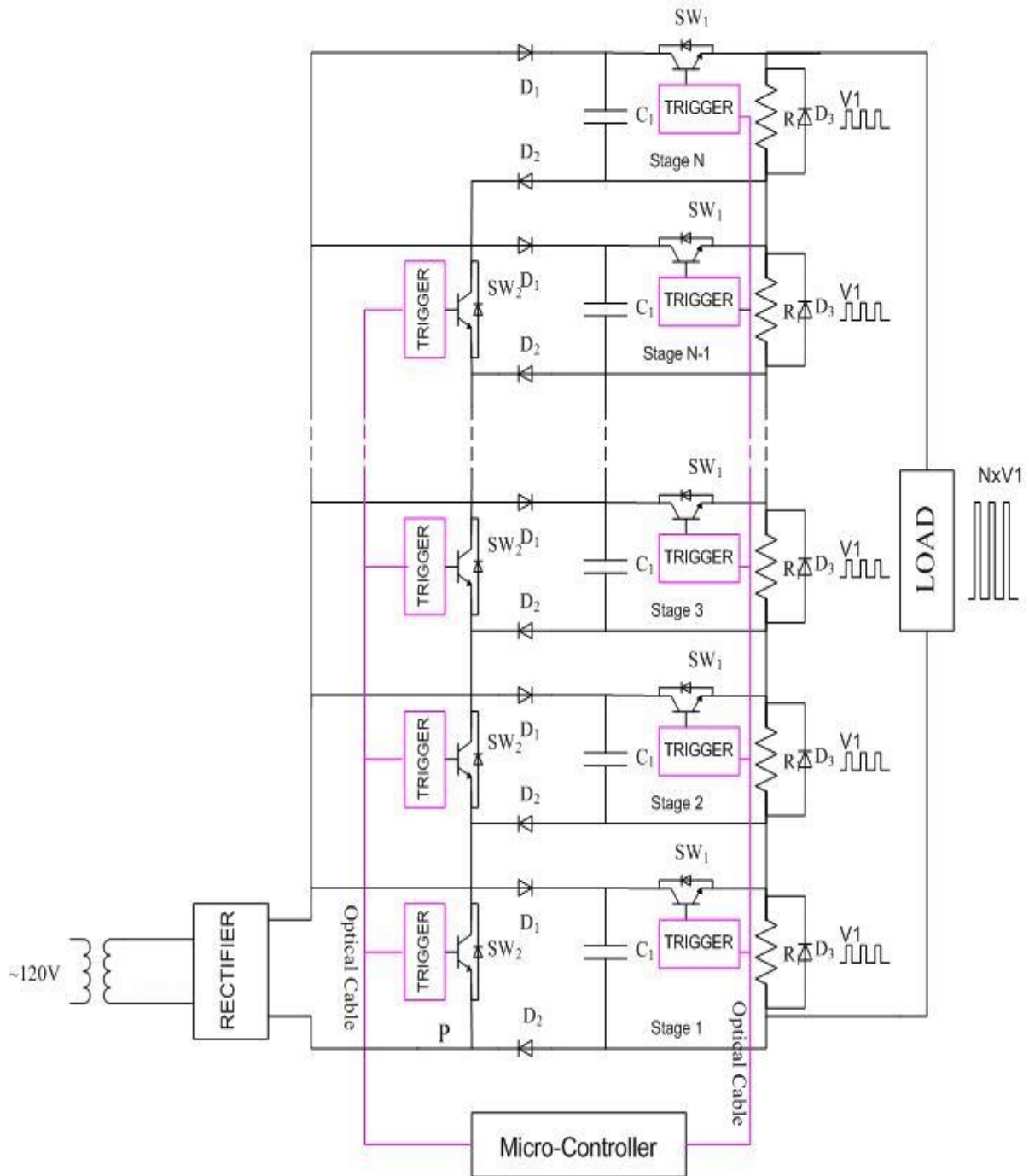
Figure 2.1. High voltage unipolar pulse generator schematic [55].
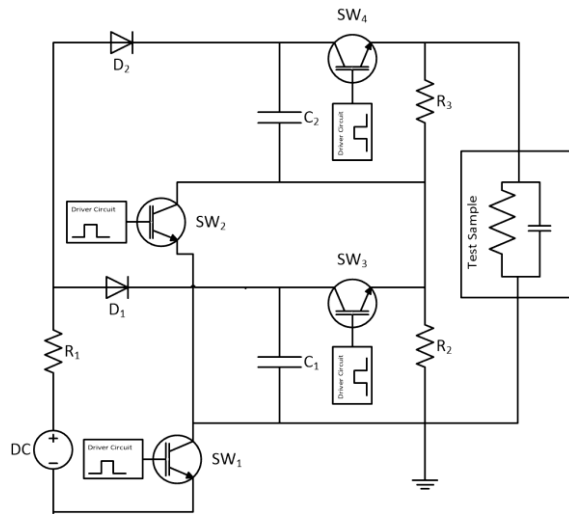
Figure 2.2. A two-stage solid-state Marx generator with SW_1 and SW_2 turned ON for charging of capacitors C_1 and C_2.
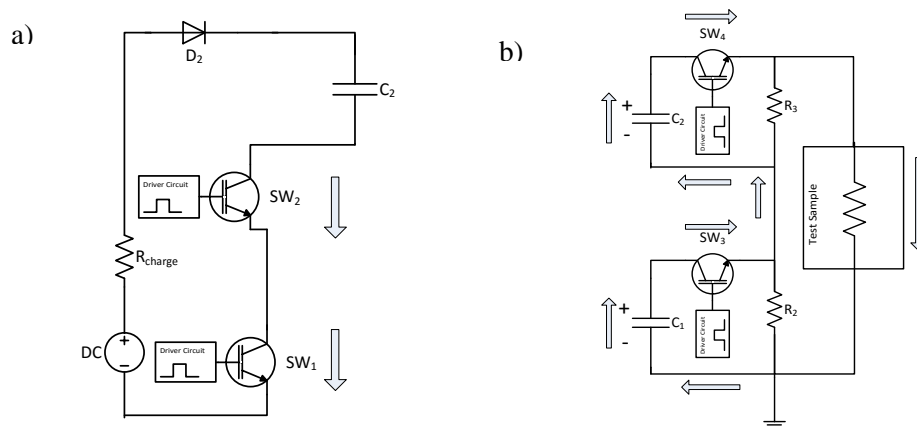
Figure 2.3. Two-stage equivalent circuit during a) the charging cycle and b) the discharge cycle.

As shown in Figure 2.3a, as the capacitors are charged and the charging switches are turned off. Then, after a dead time, the discharging switches SW_3 and SW_4 are turned on, connecting the capacitors in series and thereby delivering twice the maximum DC charging voltage to the load. Figure 2.3b shows the equivalent circuit during the discharging cycle. The dead time is adjusted in such a way that a good interlock is provided between the charging and discharging switches. If both switches turn on at the same time, the short-circuit path will burn out the switches. Resistors R_2 and R_3 discharge capacitors C_1 and C_2 when no load is connected to the output. These resistance values are several kilo ohms, which prevents the adverse operation of the generator.

25

The maximum charging current is controlled by R_1 and is selected according to the rating of the switch and load requirements. High voltage IGBT switches are selected for handling high voltage and high frequency as well as their small ON-state voltage drop. Both charging and discharging switches must be capable of withstanding the entire voltage of a single stage. Each switch has an isolated driver circuit, which takes its fire command from a controller circuit using a fibre optic link.

The waveform type, PWM or square, switching frequency, fundamental frequency, and test duration are adjustable parameters that can be set in the controller. The output voltage can be controlled by adjusting the input DC voltage, adjustable between 0 and 2 kV; therefore, with 10 stages, a maximum peak voltage of 20 kV can be generated at the output terminal. A photograph of the complete system used in this study is presented in Figure 2.4, while Table 2.1 summarizes the generator's output parameters.

Table 2.1. Output parameters of the generator

Parameter	Value
Waveform Type	Square, PWM
Output Peak Voltage	0-20 kV
Output Peak Current	100 A
SPWM Fundamental Frequency	20-300 Hz
Switching Frequency	500-4000 Hz
Rise Time	>200 ns
Overshoot	5-50 %
Maximum Capacitive Load	200 pF

Figure 2.5 shows typical waveforms of the generator when stressing turn insulation samples. A maximum of 5 turn insulation samples can be connected in parallel for voltage endurance tests.
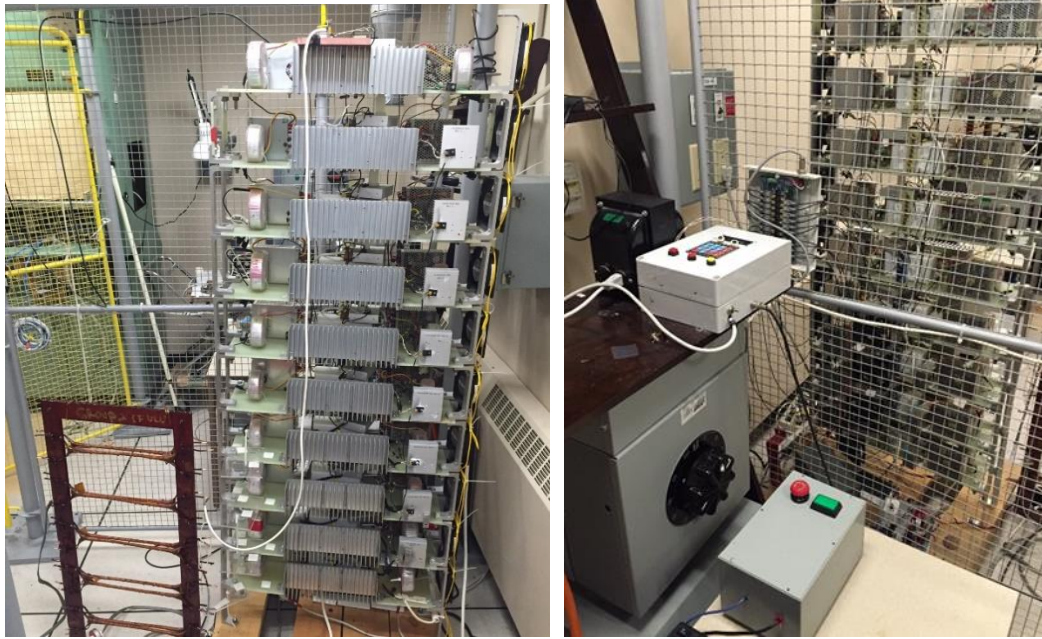
Figure 2.4. Left photograph: the high-voltage PWM generator connected to a back-to-back sample; right photograph: controller and protection system.
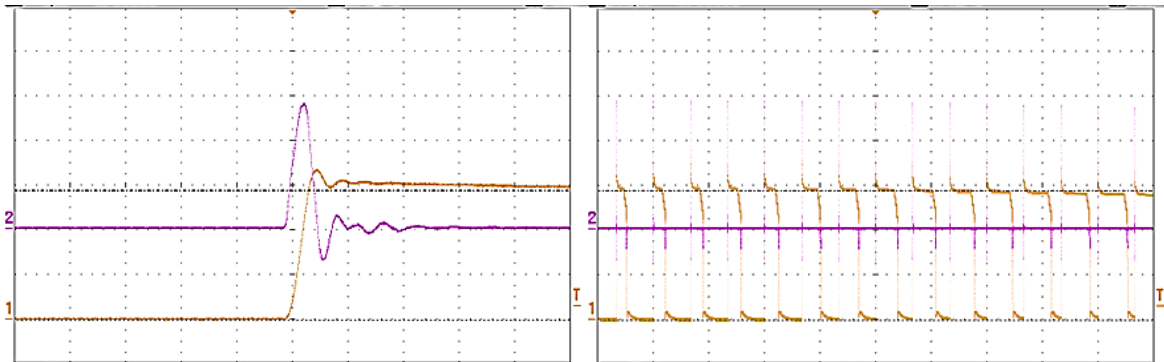
Figure 2.5. Typical waveform of the generator, where orange (1) is the output voltage (5kV/div) and pink (2) is the output current (10A/div). The time scale are 1µs/div and 500 µs/div for left and right waveforms respectively

It is important to detect a failed sample and quickly turn off the generator, otherwise the short-circuit will damage the generator and the time-to-failure of the sample will be missed. In order to address this issue, a fast protection system was designed and developed, a schematic of which is shown in Figure 2.6. The protection system is comprised of a high frequency current transformer (HFCT) and an electronic detection circuit. The electronic circuit accepts a small signal voltage representing the

27

capacitive current through the samples using the HFCT and a preset fault threshold current. By comparing the measured current to the fault threshold, the fault current is detected through a failed sample and the controller responds by shutting down the generator within 1.0 μs. It should be noted that the measured pulsed current has a pulse width of less than 2μs, as shown in Figure 2.6, which is not long enough to be detected by the controller. So, a mono-stable timer is used to lengthen the fault signal pulse.
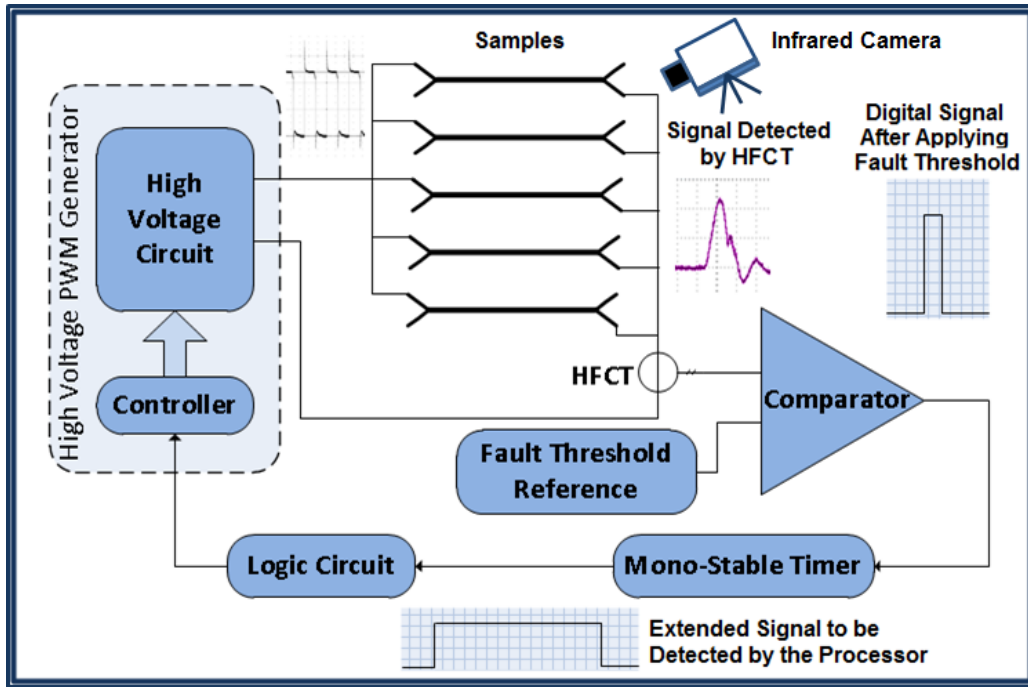
Figure 2.6. Schematic of fast protection circuit.

The fault signal interrupts the normal operation of the generator via a controller circuit, which safely shuts the IGBT switches off, sends a trip signal to the main circuit breaker, and records the failure time of the sample. After a sample fails, the sample is taken out and the generator is re-energized.

2.3 Design and Implementation of Bipolar/Unipolar Square Wave Generator

The high-voltage power supply described in the previous section is a unipolar generator which limits its application only for generating unipolar waves and therefore cannot be used when the application of bipolar pulses is required. In addition, the fall time is considerably slower than the rise time, which might affect the aging data. Hence, a new high-voltage generator that can address the above-mentioned requirements was designed and implemented.

28

Figure 2.7 shows the schematic of the implemented high-voltage square wave generator capable of generating both unipolar and bipolar pulses. The generator uses QIS4506001-powered IGBTs to generate square pulses of up to 4.5 kV peak-peak. The circuit provides the option to switch between bipolar and unipolar configurations, using a switch shown in Figure 2.7. Because it utilizes a similar topology for both unipolar and bipolar, the pulse characteristics do not alter when switching between two modes.
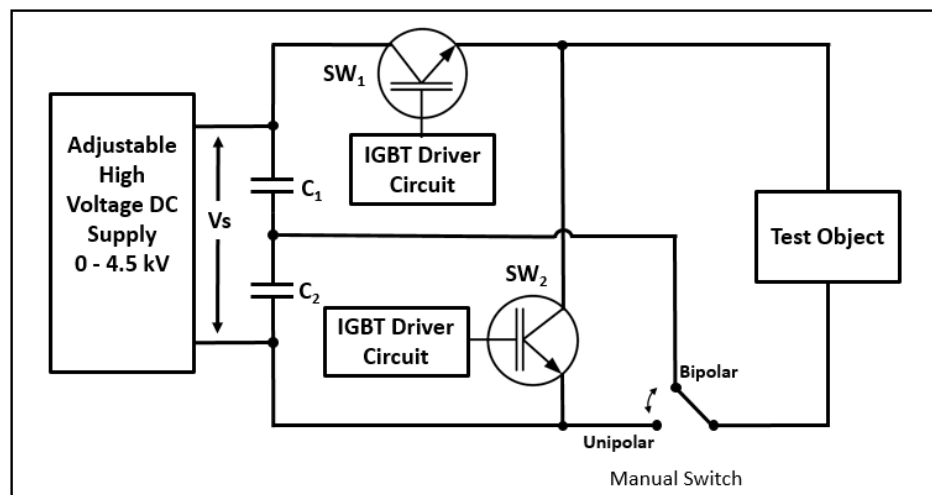
Figure 2.7. High-voltage square wave generator capable of generating both bipolar and unipolar square pulses with peak-to-peak voltage as high as 4.5 kV.

When working in unipolar mode, the capacitors are connected through SW_1, while SW_2 is open during the ON cycle of the square wave and imposes a voltage equal to Vs on the load, as illustrated in Figure 2.8a. After a short dead time, SW_1 is turned OFF, and the load which is mainly capacitive is discharged by SW_2 (Figure 2.8b). Discharging the load provides a fast fall time independent of the load.

In bipolar mode, the high voltage capacitors are charged to Vs/2 through the input DC supply. During the positive half-cycle, SW_1 imposes a +Vs/2 on the load when the SW_2 is open. Then the load is charged to -VS/2 in the negative half-cycle when the SW_2 is closed and SW_1 is open, as shown in Figure 2.9.

Figure 2.10 and Figure 2.11 show a typical wave shape of the generator for unipolar and bipolar waves respectively.
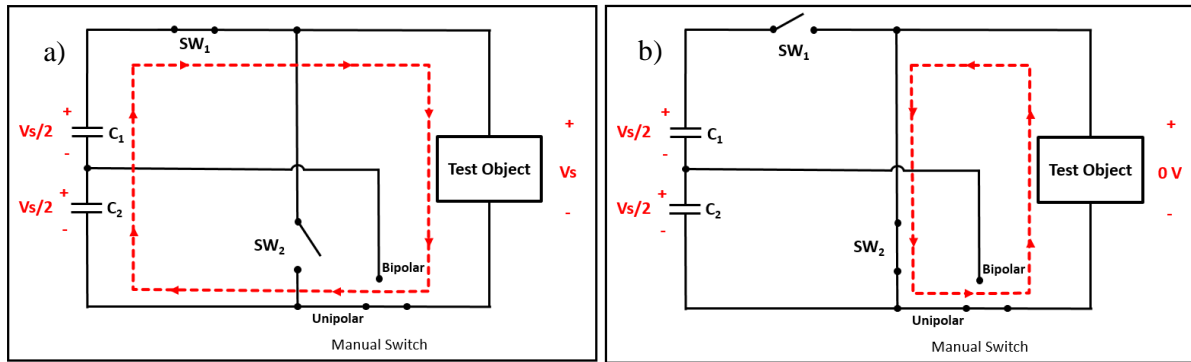
Figure 2.8. High-voltage square wave generator in unipolar mode: a) charging the load to Vs; b) discharging the load to zero.
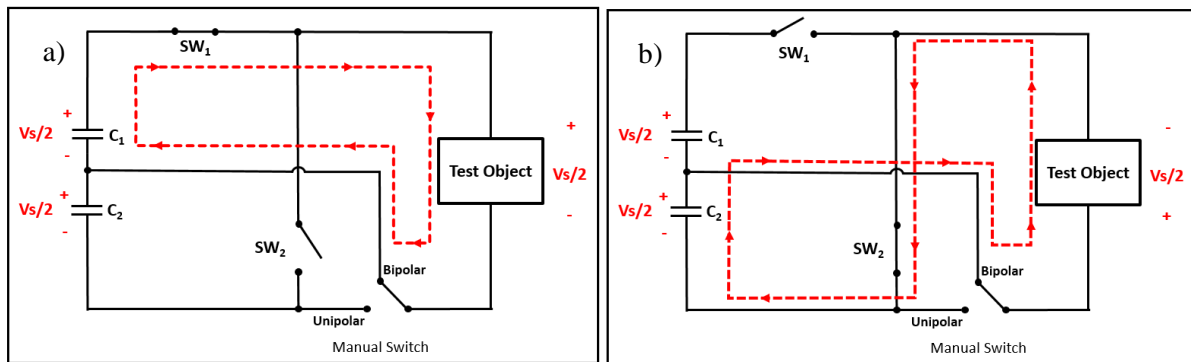
Figure 2.9. High-voltage square wave generator in bipolar mode: a) charging the load to +Vs/2; b) charging the load to -VS/2.
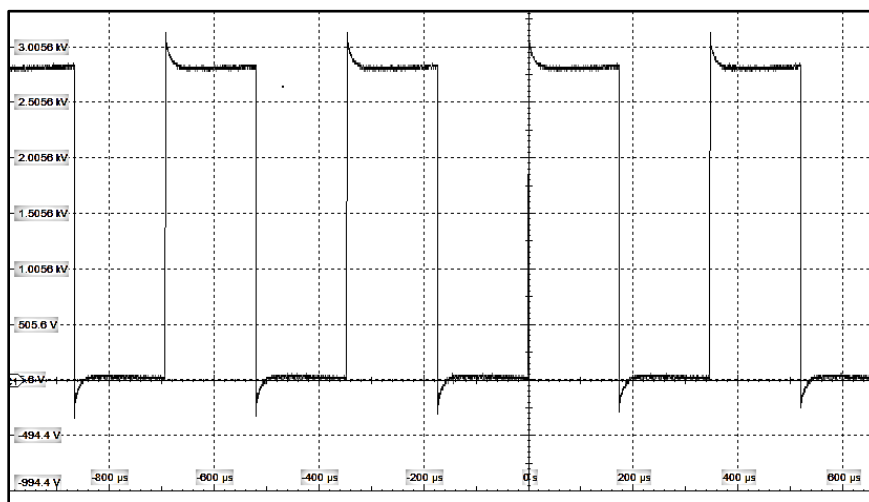
Figure 2.10. Output voltage waveform of the generator in unipolar mode.

30
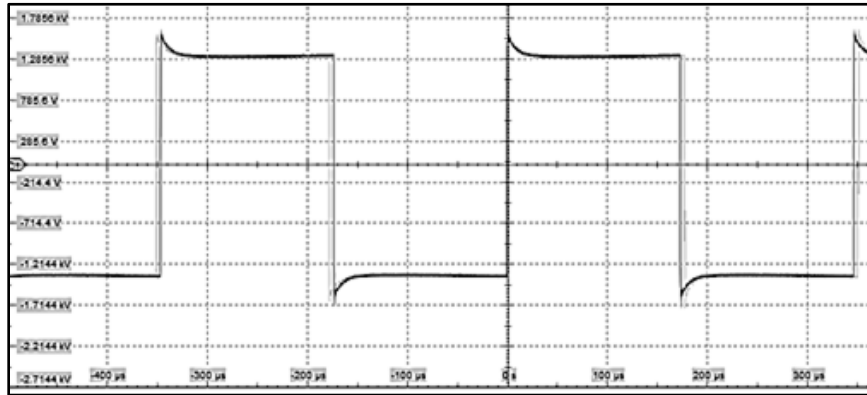
Figure 2.11. Output voltage waveform of the generator in bipolar mode.

Figure 2.12 shows the pictures of the implanted generator stressing back-to-back samples (left) and point-to-plane samples (right).
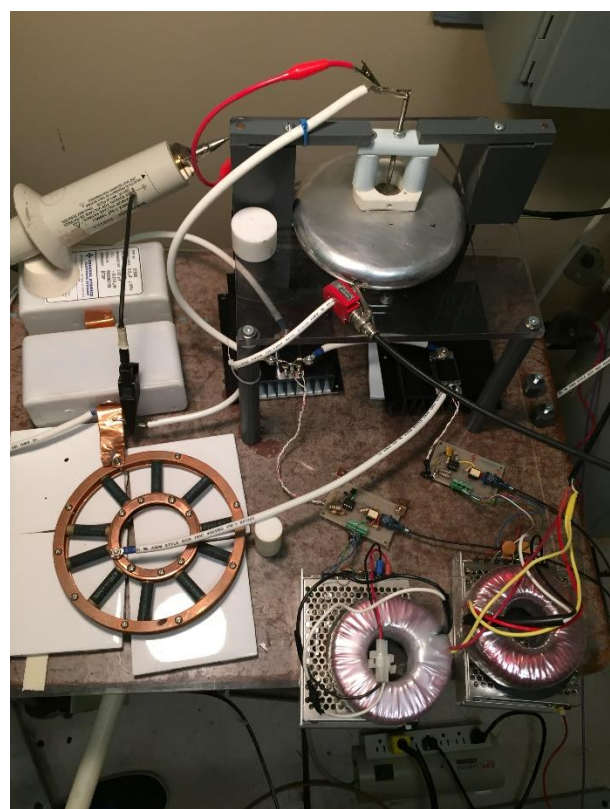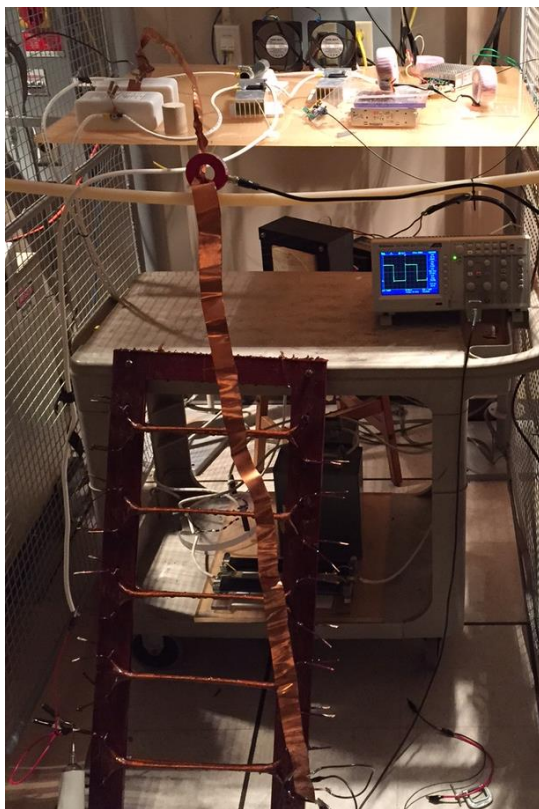
Figure 2.12. High-voltage bipolar/unipolar square wave generator. Left: the setup for aging the back-to-back turn insulation samples. Right: the setup used to stress insulation film samples using point-to-plane setup.

2.4 Design of PD Measurements in the Presence of High-Voltage PWM Interference

Detecting PD that is the main factor of insulation aging in the presence of interference emanating from high-voltage square pulse stress has great importance in the present research. Although there are commercially available instruments to do this for low-voltage random-wound machines [56], [57]; a similar instrument is needed for medium-voltage form-wound insulation in the presence of interference from a high-voltage PWM generator. Such a system is comprised of an RF antenna to collect the electromagnetic PD signals, a high-pass filter with appropriate cut-off frequency to filter out the generator signal, and a high-bandwidth oscilloscope to capture the signals.

To determine the required cut-off frequency of a filter, the frequency spectrum of the signal received by the antenna from a turn-to-turn sample was measured. Figure 2.13 shows the measured frequency spectrum with less than 1 kV applied to the sample in which no PD occurred. It shows that the PWM generator contains frequency components up to 170 MHz. PD was initiated at about 2 kV; the captured spectrum, as shown in Figure 2.14, indicates that PD signals have a frequency spectrum between 250 and 720 MHz.
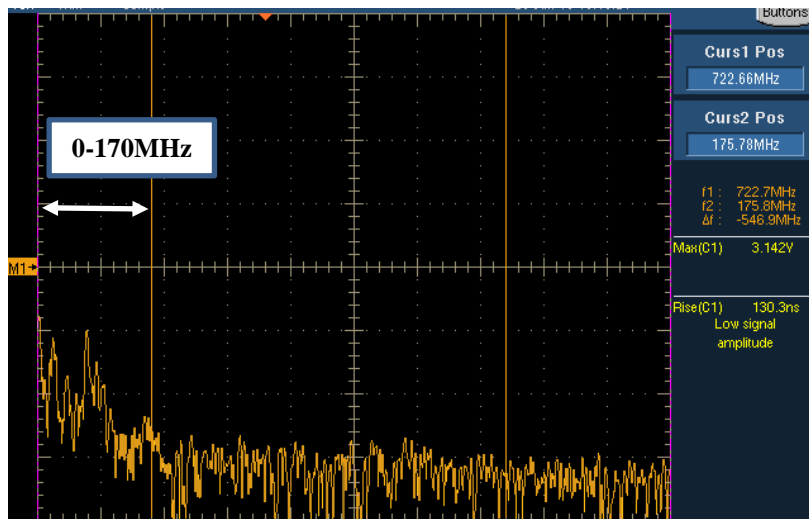
Figure 2.13. Measured frequency spectrum of antenna signal with no PD from the turn sample at 1 kV.

From the above, it can be observed that a high-pass filter that filters the signal below 250 MHz and retains the higher frequency components is useful for detecting PD that rejects the interference from the HV PWM generator. The first trial, in which a high-pass RC filter was used, was not successful, as

only a 5 dB attenuation of the generator signal (<170 MHz) was obtained while keeping PD with 3dB attenuation. This problem was solved by designing a 7th order high-pass Chebyshev filter, as illustrated in Figure 2.15, using the RF and microwave design software ADS (Advanced Design Simulation System). The simulation showed an attenuation of 51.8 dB at 170 MHz, which means that the generator signal will be attenuated by a factor of 0.0025 while keeping the PD signal nearly intact (Figure 2.16).
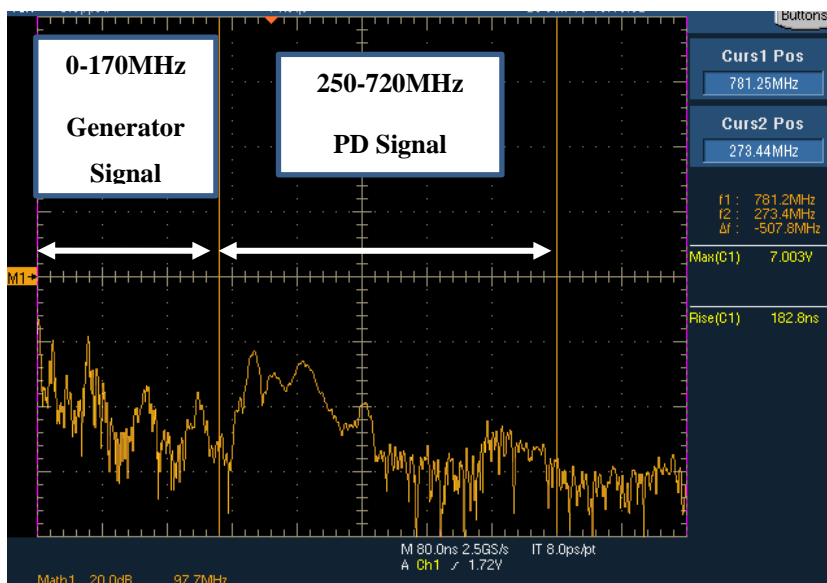
Figure 2.14. Measured frequency spectrum of antenna with PD from turn sample higher than 2 kV.
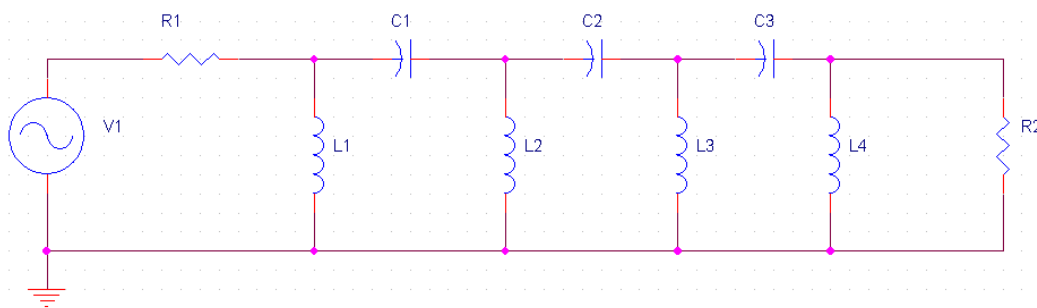
Figure 2.15. Schematic of the 7th order high-pass Chebyshev filter.

Figure 2.17 shows a photograph of the filter. The frequency response of the circuit was measured using the facilities at the Centre for Integrated RF Engineering (CIRFE) lab at the University of Waterloo. The measured results in Figure 2.18 show an attenuation of 58 dB at 170 MHz and a loss of 6 dB at 250 MHz, which is in good agreement with the simulation in Figure 2.16.

33
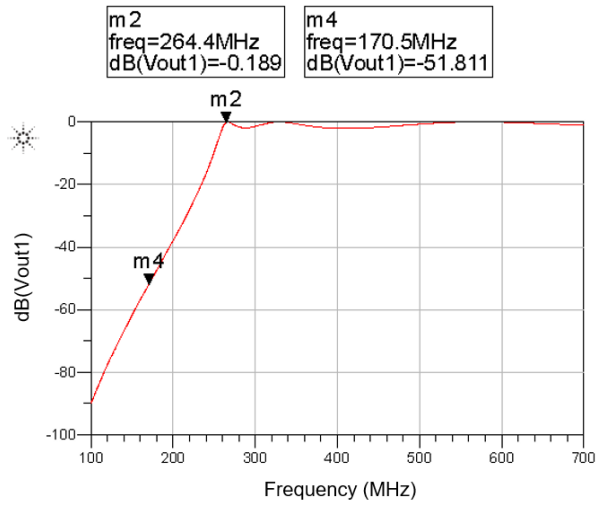
Figure 2.16. Simulated frequency response of the 7th order high-pass Chebyshev filter.
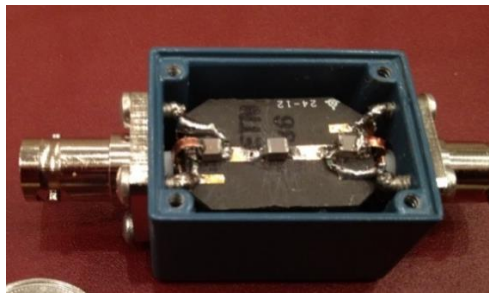
Figure 2.17. Photograph of 7th order high-pass Chebyshev filter.
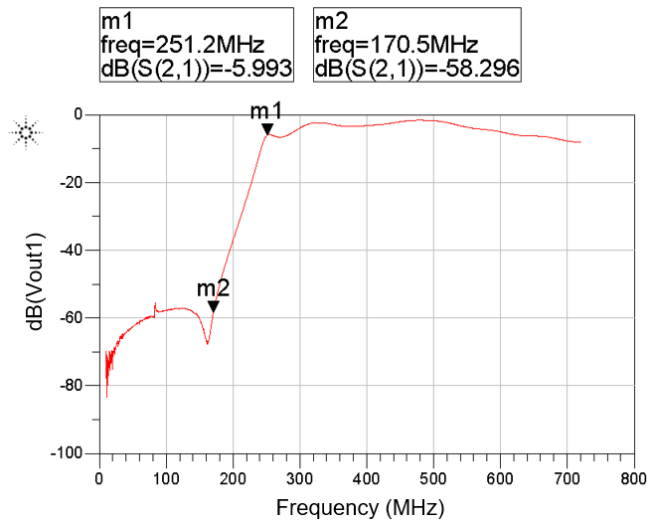
Figure 2.18. Measured frequency response of 7th order high-pass Chebyshev filter.

34

Figure 2.19 depicts the PD signal when 5 kV peak voltage was applied to a turn-to-turn sample. This shows that the generator signal is completely filtered, leaving only a very small trace.
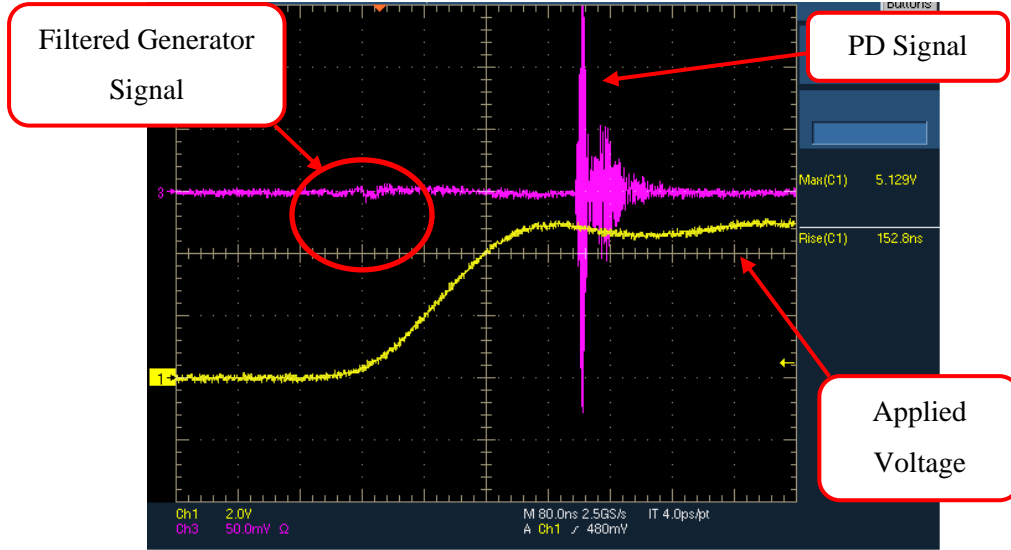
Figure 2.19. Measured applied voltage (yellow) and PD signal (pink) with 5 kV applied to a sample.

A Rohde & Schwarz RTO1024 oscilloscope with a 2 GHz bandwidth and a 10 Gsa/sec sampling rate was used to capture and record the PD. A MATLAB code was developed for the statistical analysis of the captured data in terms of the location and magnitude of the PD pulses with respect to the applied voltage waveform. The analysis involved denoising the recorded signal, detecting the PD envelope, identifying a single PD signal, and classifying the signal based on the location of the occurrence (Figure 2.20). It should be noted that PD measurements were done independent of the aging tests when a single sample was energized, and that all the comparisons presented on PD features were done on a single sample at the same aging level.
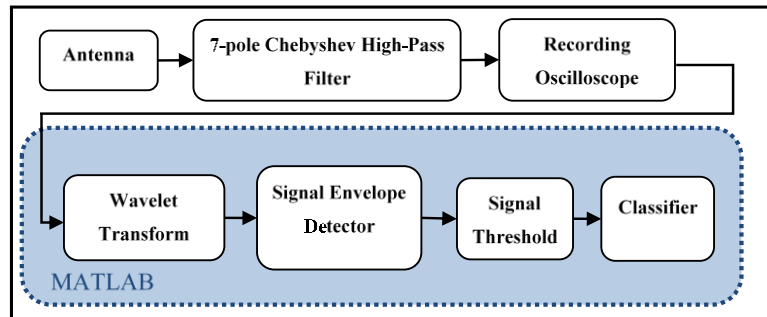
Figure 2.20. PD detection system diagram.

2.5 Back-to-back Turn Insulation Sample Preparation and Testing

Turn-to-turn insulation samples representing actual insulation in form-wound machines have to be prepared. The turn insulation samples used in this study were prepared according to the recommendations set out in IEC 60034-18-42 [1]. As illustrated in Figure 2.21, the samples were comprised of two rectangular enameled wires, whose ends were spread apart and held together with mica-glass tape and vacuum pressure impregnated (VPI). The test voltage is applied to the insulated wires simulating the stress on turn insulation.
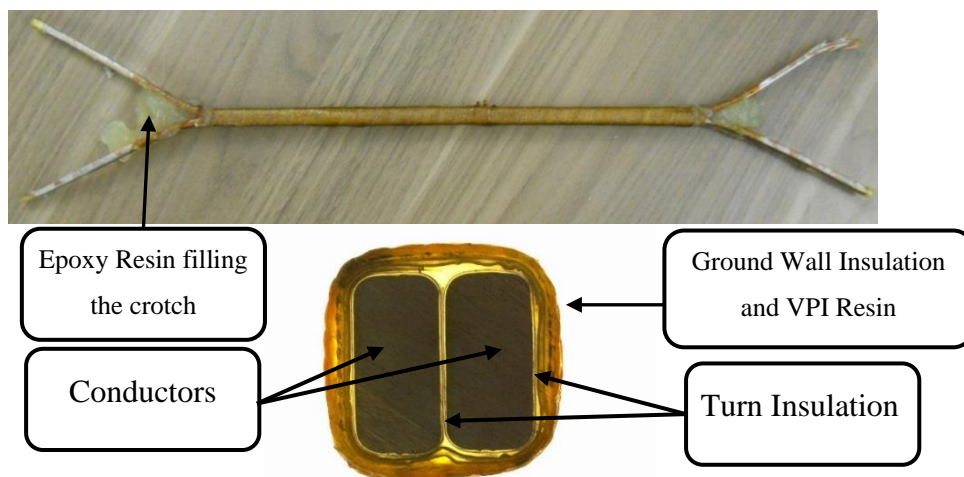
Figure 2.21. Back-to-back turn insulation sample, prepared as per IEC standard.

When the samples were constructed according to the IEC standard, failures most often occurred in the region where the wires are bent apart (crotch). The location of the failure was determined by applying a circulating short-circuit current and then observing any localized heating by means of a FLIR 650SC infrared camera. Figure 2.22 demonstrates the failure at the crotch (a) and at the straight section of the sample (b).
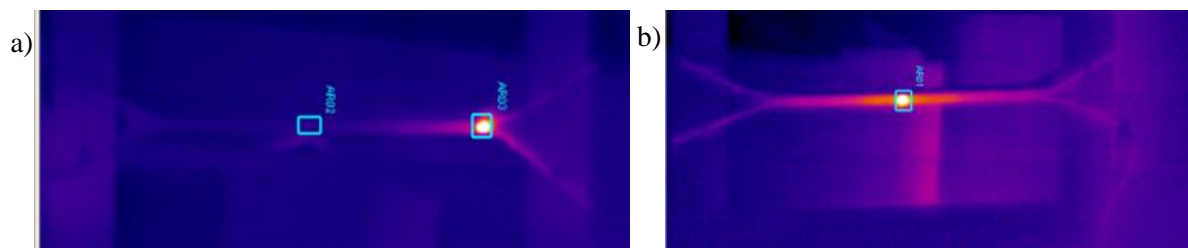
Figure 2.22. Detection of the failure location using an infrared camera: a) failure at the crotch; b) failure in the straight section.

The reason for these failures was incomplete filling of the crotch with epoxy resin and the resulting electric field enhancement in trapped air pockets. To prevent failures from occurring due to air pockets in the crotch and to address this deficiency in the sample preparation procedure described in the IEC standard, modifications were required.
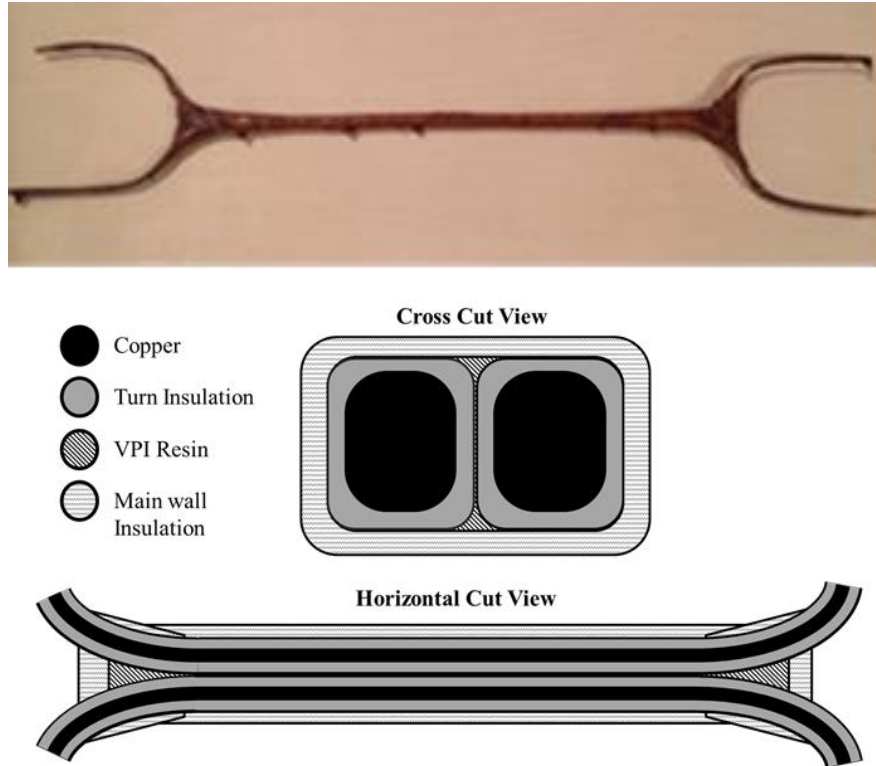
Figure 2.23. Form-wound enamel turn insulation sample prepared using IEC 60034-18-42 with modifications to prevent crotch failures.

Accordingly, the following design changes and alterations to the samples were incorporated as a means of addressing crotch failures. As a first step, in an attempt to completely fill the crotch, the filled resin was replaced with one having a lower viscosity. However, failures were observed at the interface between the filler resin and the VPI resin. The open space at the crotch also caused the VPI resin to leak following the VPI process and prior to the bake/cure process, leaving a narrow air channel at the straight section of the sample. An alternative batch of samples was prepared that entailed sandwiching a small cotton sheet between the wires at the crotch prior to the VPI process in order to keep the VPI resin in the crotch. However, this attempt resulted in failures right at the end of the triple point of the cotton, the VPI resin, and the turn insulation; these failures stemmed from the smaller interface and

greater electric field at that location. The trial was repeated using an RTV silicone sealant rather than cotton, which resulted in the same issues. It was noted that avoiding any field enhancement required the crotch to be filled only with VPI resin without voids.

The results of these initial trials led to the preparation of good samples, in which the crotch was covered and sealed with mica-glass tape and a folded piece of cotton was placed into the covered crotch to form a pool of resin, thereby keeping the VPI resin in place. However, in a few samples, resin still seeped out after the VPI process and prior to baking, leaving some air pockets at the crotch. This problem was solved by repeating the VPI cycle several times (Figure 2.23). The uniformity of the prepared samples was confirmed by measuring PDIV using square waves with a switching frequency of 1 kHz. The inception voltage was similar and averaged at 1.7 kV peak. For the work reported here, five samples in each test group were prepared for Weibull time-to-failure analysis.

2.6 Time-to-failure Examination of Back-to-Back Turn Insulations Under PWM Stress

Time-to-failure experiments are conducted in order to relate a specific parameter (e.g., voltage level, rise time, switching frequency, duty cycle, insulation material, and lapping) to the time-to-failure of the insulation. Therefore, a group of five samples was selected and stressed, using the desired pulse parameters and either bipolar or unipolar pulse generators, as shown in Figure 2.6. When a sample fails, the protection system disconnects the generator and records the time. Then the location of the failure is inspected using an IR camera to make sure it occurred in the straight section of the sample.

The aging test is resumed for the remaining samples until all samples have failed and the time-to-failure for each sample is extracted. In order to keep the pulse parameters consistent, a dummy high-voltage capacitor replaced the failed sample when required. The time-to-failure data are plotted using the Weibull distribution, and statistical parameters are extracted. Figure 2.24 shows the timeline of aging test on five samples; it also demonstrates the use of IR camera in locating the site of failure in samples.
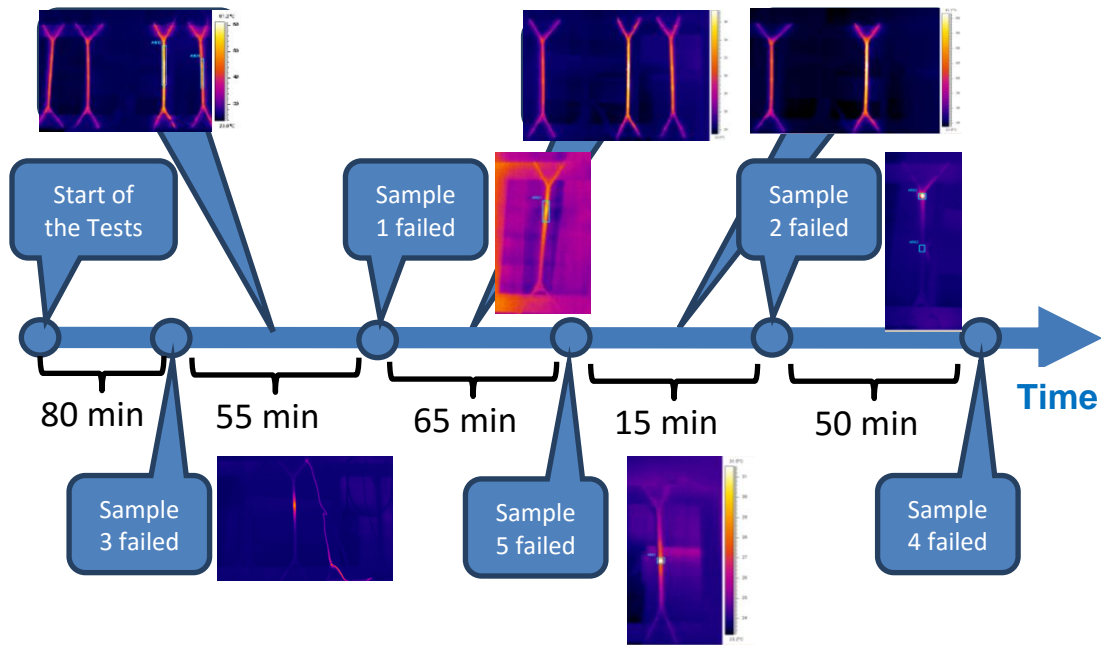
Figure 2.24. An example of the timeline of the failure test process.

2.7 Point-to-plane Setup with Insulation Film Barrier

The presence of voids or air pockets in the process of making machine insulation as well as form-wound back-to-back samples is inevitable. Although the back-to-back samples are an appropriate representation of machine insulation and are suitable for time-to-failure analysis, PD measurements are not consistent due to a multitude of voids in the insulation system. Therefore, to study the PD features with square wave parameters, a simple geometry test cell having a single source of PD with controlled dimensions is necessary, and the cell must be representative of a single void that appears in a form-wound insulation.

Figure 2.25 shows the test cell used in the study. It is made of a point-to-plane electrode assembly with an insulation film on the plane electrode, and an air gap between the point electrode (0.5 mm radius) and the insulation barrier material of 0.25 mm. Various insulation materials with dimensions 37.5 mm x 37.5 mm were used and held in place with a cylindrical ceramic spacer.
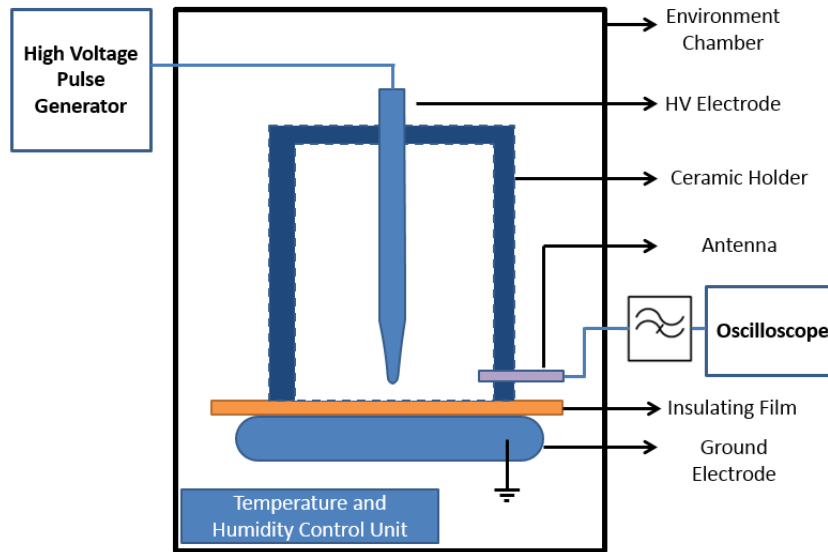
Figure 2.25. Schematic of the point-to-plane test setup.

This geometry provided a single cavity for recording PD events. A miniature RF antenna was attached to the ceramic spacer to capture PD and a high-pass filter was used to filter out the square wave pulses from the generator, allowing only the PD pulses to be recorded.

The point-to-plane setup was used for all the fundamental studies, including the time-to-failure experiment on the insulation film, PD measurements, and surface charge measurements.

The setup was placed into an environment chamber in order to conduct studies on the effect of temperature and humidity. The temperature was controlled using a heater and a PLC controller. The humidity was adjusted manually by the placement of water containers and constant monitoring of humidity levels. It should be noted that the environment chamber was only used for temperature and humidity studies and that all other tests were done in the lab environment.

To ensure that the PD was occurring from the point electrode and not from accumulated charge on the 37.5 mm x 37.5 mm sheets to the ground plane, a larger 150 mm x 150 mm sheet of Kapton® film was used to observe the PD. These measurements confirmed that the PD was indeed occurring from the point electrode which are presented in the next chapter.

2.8 Surface Potential Measurements

Using the point-to-plane setup, the effects of pulse type and switching frequency on surface charge accumulation were investigated by pulse stressing the insulation film for a fixed period, disconnecting the generator from the point electrode, and then measuring the surface potential using a TREK 341A non-contacting electrostatic potential probe. The pulse stressing time of 5 minutes was selected based on PD amplitude and surface charge measurements that stabilized after 3 minutes of pulse stressing. The surface potential profile was obtained by sweeping the probe across the surface using a linear motorized positioning device with steps of 1 mm, starting at the centre of the film right after it was stressed using the pulse generator. Figure 2.26 shows the surface potential measurement setup.
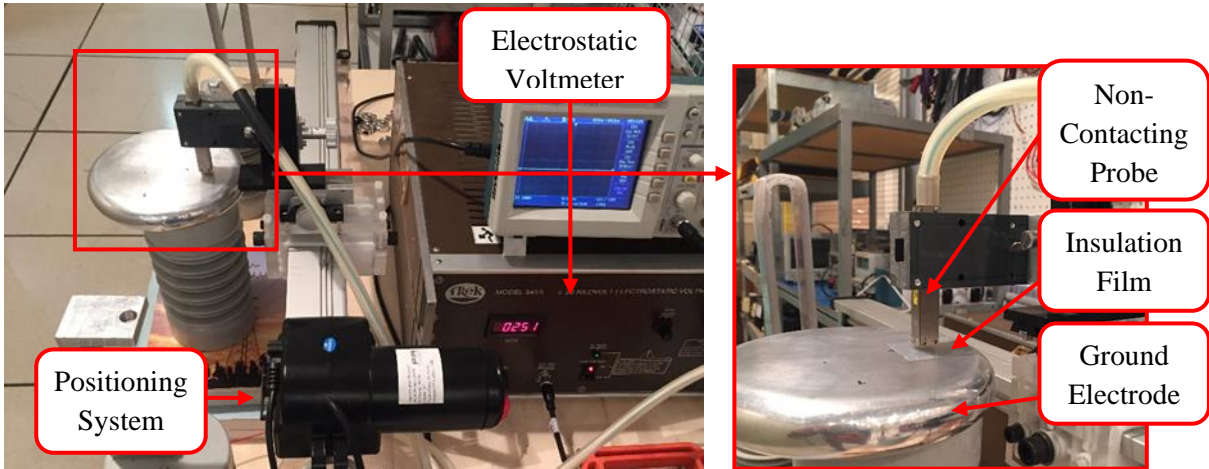
Figure 2.26. Surface potential measurement using non-contacting voltmeter and a linear motor.

2.9 Surface Charge Measurements

Measuring the surface potential provides some knowledge of the accumulated charge, but it does not yield the actual amount of the charge. Moreover, it is not known how much charge is dissipated during the process of transferring the film to the measurement station, although the charge dissipation rate was observed to be very slow. Therefore, implementing a measurement system capable of estimating the amount of charge is beneficial.

The following describes the direct surface charge measurement method based on collecting the charge using a fixed capacitance, which in this case is the input impedance of an oscilloscope set to 50 Ω. Figure 2.27 shows the equivalent circuit. The Rohde & Schwarz RTO1024 oscilloscope introduced in the previous sections is used to capture the pulses.

The insulation film is stressed for five minutes with the desired pulse parameters. Then the pulse generator controller is triggered to turn off the IGBT switches instantaneously and disconnect the point-to-plane setup from the power supply. The high voltage connection is physically removed from the point electrode and the accumulated charge on the surface is scavenged by snapping a low voltage probe to the point electrode while the ground connection is connected to the ground plane. The flow of charge through the oscilloscope probe results in a voltage pulse with decaying tail, and the peak of the pulse is proportional to the scavenged charges that can be calculated from the probe's capacitance (Q = CV) as well as its input impedance.
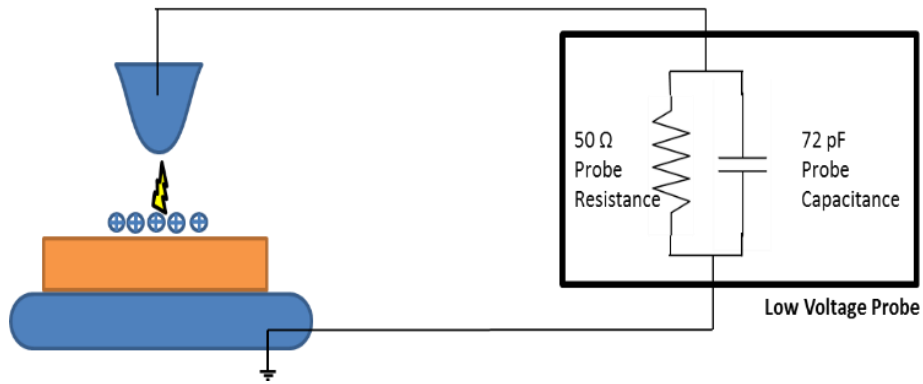
Figure 2.27. The measurement of surface charge using the low-voltage probe.

It should be noted that this process collects only a portion of the surface charge from each snapping. Therefore, the process of snapping the probe to the point electrode is repeated in intervals of several seconds, allowing the charge to reach equilibrium after each reading. This process was repeated until most of the charge was extracted from the surface. Hence, the total surface charge can be estimated from the summation of all of the pulses captured by the probe. Figure 2.28 shows the overlaid pulses captured for the 50 Ω and 1 MΩ input impedances of the oscilloscope. As can be seen, the peak voltage that is proportional to the scavenged charge diminishes after several iterations.

The capacitance of the probe is confirmed as equal to 72 pF by measuring the time-to-decay to 50% for both the 50 Ω and 1 MΩ internal impedances, as follows:

$$V_{100\%} - V_{50\%} = 0.5 = e^{\frac{-t}{RC}} \rightarrow t = 0.693\ RC$$

$$C_{50\Omega} = \frac{2.5 \times 10^{-9}}{0.693 \times 50} \approx 72\ pF \qquad\qquad C_{1M\Omega} = \frac{50 \times 10^{-6}}{0.693 \times 1 \times 10^6} \approx 72\ pF$$
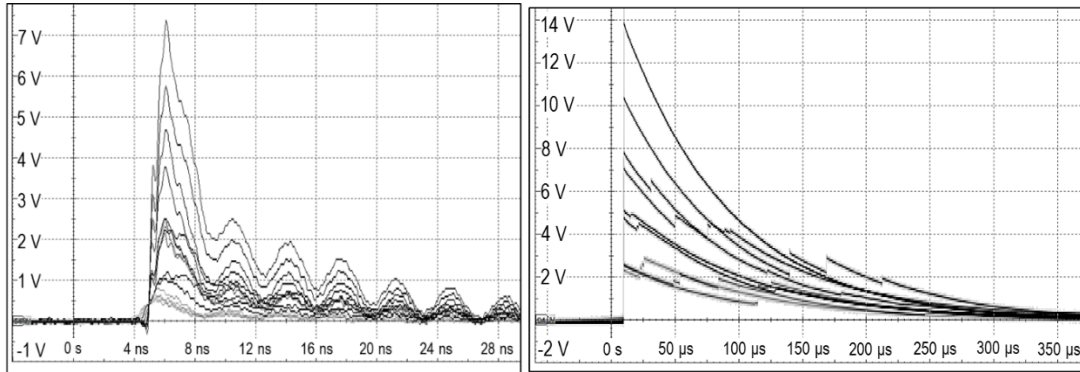
Figure 2.28. Overlay of voltage pulses captured several seconds apart by snapping the probe to the point electrode for estimation of surface charge; top, 50 Ω, and bottom, 1 MΩ, internal impedances.

2.10 Test Materials

Two types of samples are used in the present research, namely back-to-back turn insulation and insulation film samples. Back-to-back insulation samples, which represent the actual insulation system used in the machines, are prepared based on the method described in section 2.5 and employed to examine the lifespan of machine insulation with respect to various parameters. Table 2.2 summarizes the materials and construction of the samples.

Table 2.2. Back-to-back turn insulation samples

Insulation Group	Turn Insulation	No. of Layers and Lapping	Nominal Thickness (pu)
A	mica/film	1 layer 1/2 lap	2.7
B	mica/film	1 layer 1/3 lap	(1.3-2.7)
C	mica/film	2 layers butt lap	2.7
D	Daglas®	N/A	1.7
E	Daglas®	N/A	2.5
F	enamel I	N/A	1
G	enamel II	N/A	1
H	enamel + mica glass turn tape	1 layer 1/2 lap	4.2

Film insulation samples, which are characterized in Table 2.3, are mainly used in a point-to-plane setup to conduct the fundamental studies in which there is only one source of PD at the tip of the point electrode. The fundamental study includes PD features, times-to-failure, surface potential, and surface charge measurements when stressed using square waves. The mica sheet was subjected to 160 °C for 2 hours to remove moisture. The surface resistivity of the films were measured using the method described in ASTM D257 [58].

Table 2.3. Properties of insulating films

Material	Dielectric Constant @ 1 MHz	Surface Resistivity (Ω/Sq)	Thickness (mm)
Mica sheet	6	6×10^{13}	1
Kapton®	3.4	10^{16}	0.125
PA6 (Nylon 6)	3.6	5×10^{10}	0.1
PTFE (Polytetrafluoroethylene)	2.1	10^{17}	0.1

2.11 Statistical Methods

Analyzing the results of aging and failure is an important part of this research. It requires the use of statistical methods to correlate insulation failures to specific parameters. Among the statistical distribution functions available to represent and analyze life and time-to-failure estimations, Weibull distribution is a well-known method [59]. The cumulative Weibull distribution function is given by:

$$F(t) = 1 - \exp[-(\frac{t - \gamma}{\eta})^{\beta}]$$

The random variable *t* may represent time-to-failure or the electric field required for breakdown where the electric field increases linearly with time. The scale parameter, η, represents the time required for 63.2% of samples to fail and is an indication of average time-to-failure, and the parameter γ indicates the time of aging where failure is not possible. The parameter β is a dimensionless factor known as the shape parameter and can be interpreted as follows:

A value of $\beta < 1$ indicates that the failure rate decreases over time. This happens if there is significant "infant mortality" or defective items failing early, with the failure rate decreasing over time as the defective items are weeded out of the population.

A value of $\beta = 1$ indicates that the failure rate is constant over time. This might suggest random external events are causing failure.

A value of $\beta > 1$ indicates that the failure rate increases with time. This happens if there is an "aging" process or parts that are more likely to fail with time.

2.12 Modeling and Simulation

Modeling and simulation of a turn insulation system provides a better understanding of the system under particular conditions, and allows for exploring the effects of various parameters such as geometry and material properties on a specific requirement. Moreover, the findings and speculations obtained from experiments may be confirmed using such simulations. In this regard, COMSOL®, a finite element method (FEM) simulation tool, is employed to simulate turn insulation system under various conditions.

The electric field and Maxwell-Ampere's equations are the main governing equations on this subject, as follows:

$$E = -\nabla V$$

$$\nabla \times H = J_c + \frac{\partial D}{\partial t}$$

Applying divergence on both sides and the charge continuity condition ($\nabla . \nabla \times H = \nabla . J_{total} = 0$), we have:

$$\nabla . \nabla \times H = \nabla . \left[J_c + \frac{\partial D}{\partial t} \right] = 0$$

where E, V, ε, and ρ represent the electric field, scalar potential, permittivity of material, and space charge density, respectively. J represents conduction current density, where $J = \sigma E + D$, and $\frac{\partial D}{\partial t}$ displacement current density, where $D = \varepsilon E + P$.

Solving the above-mentioned equations with FEM will be used to model the turn-to-turn insulation of form-wound machine coils in this research.

2.12.1 **Simulation of Back-to-back Turn Insulation Samples Using FEM**

FEM simulations were employed to investigate the distribution of the electric field, electric current and temperature on turn-to-turn samples when stressed by square pulses. The effects of an air gap at the crotch of the sample as well as the thickness, permittivity and conductivity of the materials on the electrical parameters were tackled in these simulations. Figure 2.29a shows a schematic representation of the turn-to-turn sample. The electrostatic and Joule modules of heating were used to simulate the sample in both the stationary and time domain simulations.
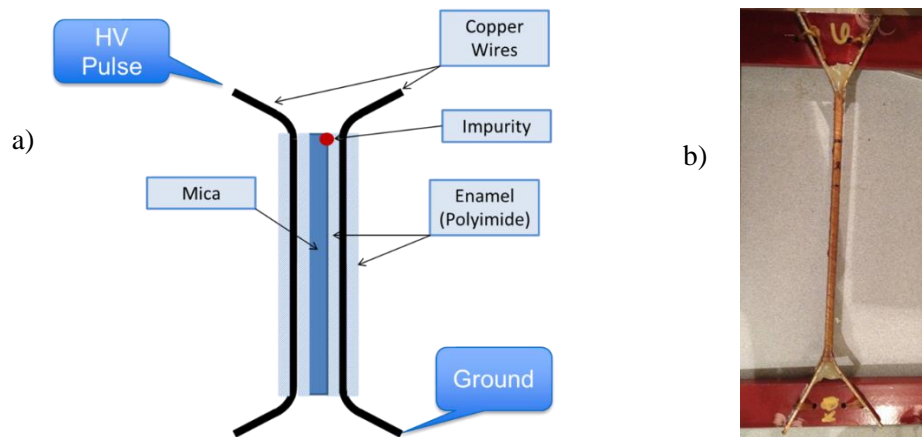
Figure 2.29. (a) A schematic of turn-to-turn sample; (b) a photograph of the prepared sample.

Figure 2.30 shows the implemented geometry of the sample. All the dimensions are parametric so that they easily can be changed. This geometry consists of a copper conductor, enamel coating (silica glass is used in the material assignment), mica turn insulation, and an insulating material to fill the space at the crotch surrounded by air. There are also two air cavities: one in the form of a bubble at the intersection of two insulations, and the other right at the crotch. Figure 2.31 shows the material assignment for each highlighted part.
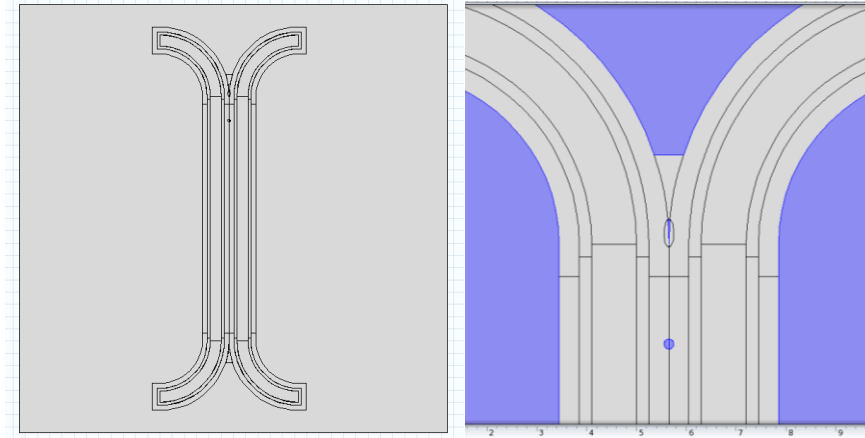
Figure 2.30. The geometry implemented in COMSOL®.
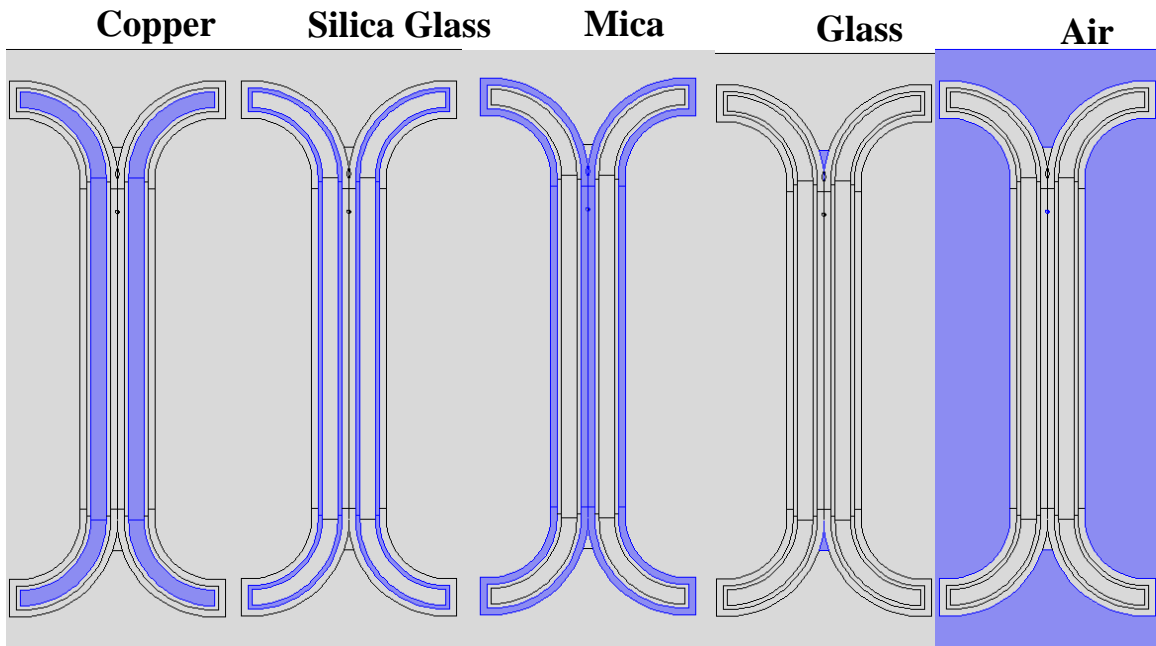
Figure 2.31. Material assignment for each section (the assigned part is highlighted).

The parameters to control the thickness include enamel insulation layer thickness (th = 0.01cm), mica turn insulation thickness (turn = 0.2 cm), copper conductor width (cond width = 0.9 cm), and the bending radius of each leg (bend = 5 cm). Table 2.4 summarizes the required parameters for each material used.

Table 2.4. Required material properties for joule heating and electrostatic studies

	Relative Permittivity	Electrical Conductivity σ [S/m]	Thermal Conductivity k [W/(m*K)]	Heat Capacity at Constant Pressure Cp [J/(kg*K)]	Density ρ [kg/m³]
Copper	Inf	5.998×10^7	400	385	8700
Air	1	1×10^{-20}	0.0257*	1005*	1.205*
Silica Glass	4	1×10^{-14}	1.38	703	2203
Mica	6	2.01×10^{-15}	0.71	500	520
Glass	4.2	1×10^{-14}	1.05	840	2579

* at room temperature.

The electric potential is applied to two copper wires: high-voltage potential (left side), and ground (right side). The boundary condition considered for joule heating includes electrical insulation, thermal insulation and heat flux, all of which have the same boundary on the outer box, as shown in Figure 2.31. The heat flux coefficient is considered like that of air and is equal to 5 W/m²K.

2.12.2 Simulation of Point-to-plane Setup with Insulation Film Barrier

An electrostatic study was employed to simulate the electric field in the air gap of the point-to-plane setup for the different insulation films presented in Table 2.3. Figure 2.32 shows the geometry of the point-to-plane setup implemented in COMSOL®. The system has an axial symmetry around the z axis, and the permittivity of materials is selected based on the values reported in Table 2.3. The permittivity of the electrode was set to a very large value to represent that of metals. The permittivity of the box surrounding the point electrode was set to unity to represent permittivity of air.

A radial charge distribution function is also added to the surface of each film to represent the leftover charge after stressing the system using high voltage pulses. The initial charge in the system was set to zero.
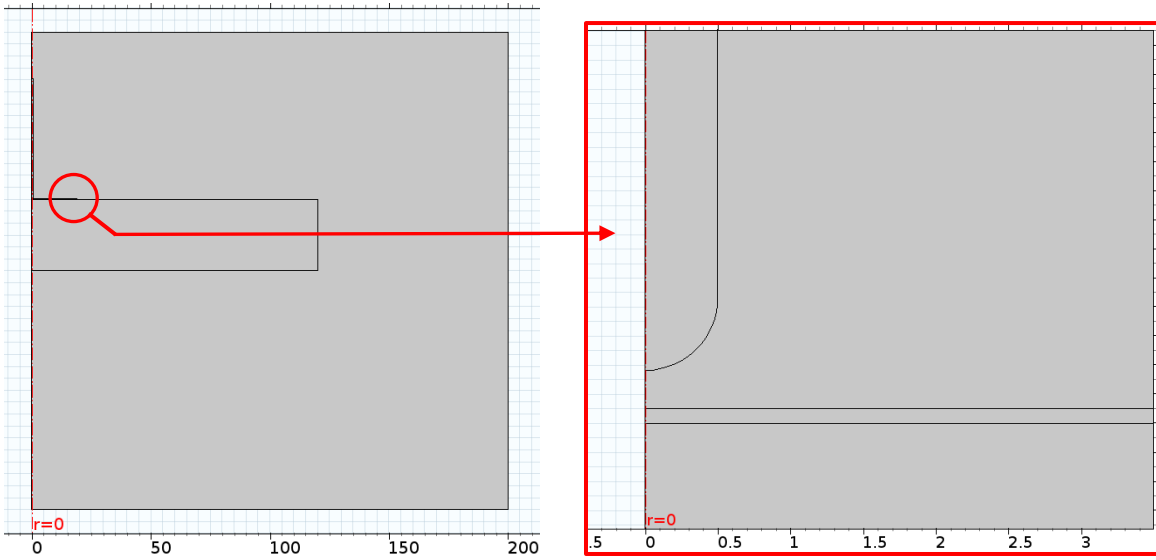
Figure 2.32. Geometry of point-to-plane setup.

Chapter 3

Results

3.1 Introduction

This chapter presents experimental and simulation results, including times-to-failure examination of back-to-back turn insulation samples using parameters such as insulation type, applied voltage, rise time, switching frequency, duty cycle, and pulse type. The chapter also details fundamental studies on point-to-plane setup with different film insulations, evaluating times-to-failure, PD features, surface potential, and surface charge when stressed using square pulses with different parameters. As well, it provides the simulation results for the back-to-back samples and point-to-plane setup.

3.2 Times-to-failure Determination of Different Turn Insulation Types Stressed Under PWM Unipolar Pulses

A unipolar PWM waveform with a peak of 12 kV, a rise time of approximately 270 ns, and a switching frequency of 3 kHz was used for aging. Four different insulations (enamel, Daglas®, mica tape with polyester film, and enamel with mica glass turn tape as the baseline insulation system) were considered, for a total of eight variations. Five samples from each group were prepared as shown in Table 2.2. The time-to-failure data were analyzed using two-parameter Weibull statistics, with the breakdowns examined microscopically to provide information on the probable cause of the failures.

3.2.1 Time-to-failure Analysis

The turn insulation samples introduced in Table 2.2 were subjected to a 12 kV peak unipolar PWM waveform recording the time-to-failure of each sample (Table 3.1). The highlighted times-to-failure in Table 3.1 are those that took place in the crotch of the samples due to incomplete filling of the air space during sample preparation. These results were not considered valid and were therefore not used in the statistical analysis. This included all samples of Group A. Additionally, the samples of baseline Group H did not fail even after 800 hours of aging, so these were also not included in the discussion, despite their demonstrating the highest voltage endurance among all groups considered.

The remaining group failures, which took place in the straight section of the samples, are considered valid and were analyzed using ReliaSoft®'s Weibull++ software. The Weibull plots are shown in Figure 3.1, while the Weibull parameters are shown in Table 3.2. The scale parameter η in Table 3.2

indicates the characteristic time-to-failure in minutes for each group. The taped samples, Groups B and C, have the longest times-to-failure compared to the enamel and Daglas® samples, with the enamel Group F showing the shortest times-to-failure.

The shape parameters, β (or the slopes), of the Weibull distributions are all well above one, indicating that the failures are due to aging.

Table 3.1. Times-to-failure (minutes) for different insulation groups subjected to unipolar PWM waveform having 12 kV peak applied voltage and 3 kHz switching frequency

Sample No	Group Name						
	A	B	C	D	E	F	G
1	10080	1510	5010	20	24.5	0.42	59.5
2	9810	462	2730	5	34	1.36	104
3	17546	357	1526	21	15	0.98	67
4	14546	844	3810	18	33	1.19	127
5	14530	473	3300	10	10	0.72	142.5
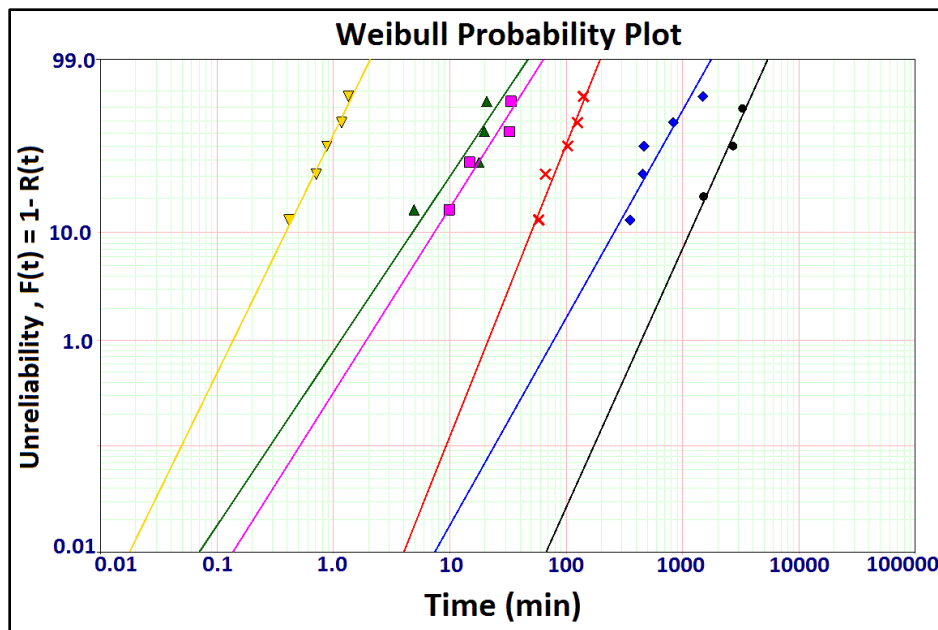
Figure 3.1. Weibull probability plots for Groups B (♦), C (●), D (▲), E (■), F (▼) and G (×).

51

Table 3.2. Weibull Parameters

Weibull Parameter		Insulation Group					
		B	C	D	E	F	G
η (min)	Scale Parameter	809	2888	18.6	26.6	1.05	112
β	Shape Parameter	1.96	2.45	1.65	1.75	2.26	2.76
ρ	Correlation Coefficient	0.99	0.98	0.89	0.96	0.99	0.97

In order to have a more detailed comparison, groups with the same insulation are compared in the following sections.

3.2.2 Mica Film Turn Tape (Groups A, B and C)

As can been seen in Table 3.1, nearly all of the failures of Group A samples consisting of one layer 1/2 lap of mica/film took place in the crotch. Nevertheless, the times-to-failure are much longer than those of the corresponding insulation with 1/3 lap (Group B), where the failures took place in the straight section. This indicates that the 1/2 lap construction is superior to the 1/3 lap construction. Furthermore, although the two-layer butt lap using mica/film tape (Group C) showed longer times-to-failure compared to Group B, Group C samples showed shorter times-to-failure than Group A samples. It is curious that Group C samples did not last as long as Group A samples, despite having the same insulation thickness. Thus, the observed differences could be related to the type of lapping used.
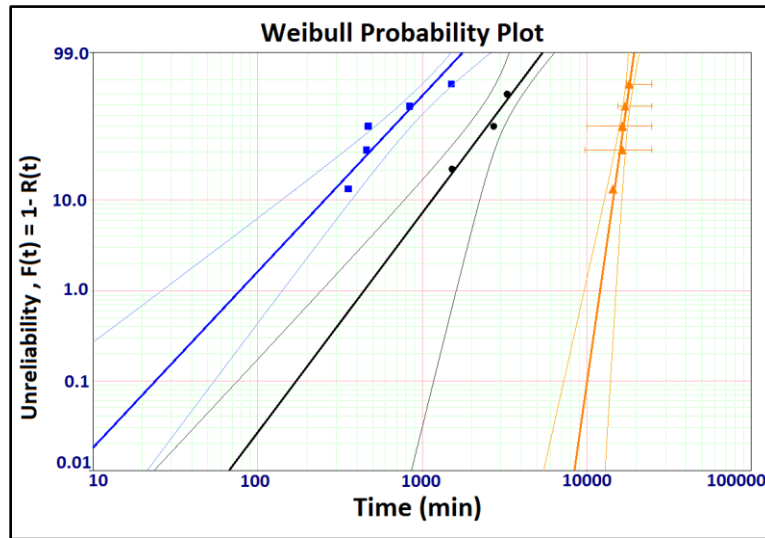
Figure 3.2. Weibull probability plots for Groups A(▲), B(♦), and C(●) with 80% confidence bounds.

Figure 3.2 shows the Weibull plots for the three groups, including the results of the times-to-failure in the crotch for Group A and the valid failures for Groups B and C, along with their corresponding 80% confidence bands. Clearly, the voltage endurance is the greatest for Group A, followed by Group C and then Group B.

3.2.3 **Daglas® (Groups D and E)**

The Weibull probability plots for Groups D and E are shown in Figure 3.3, together with their corresponding 80% confidence bands. Given the confidence bands of the data overlap, it can be concluded that no difference exists between these two groups, albeit Group E samples have slightly thicker insulation.
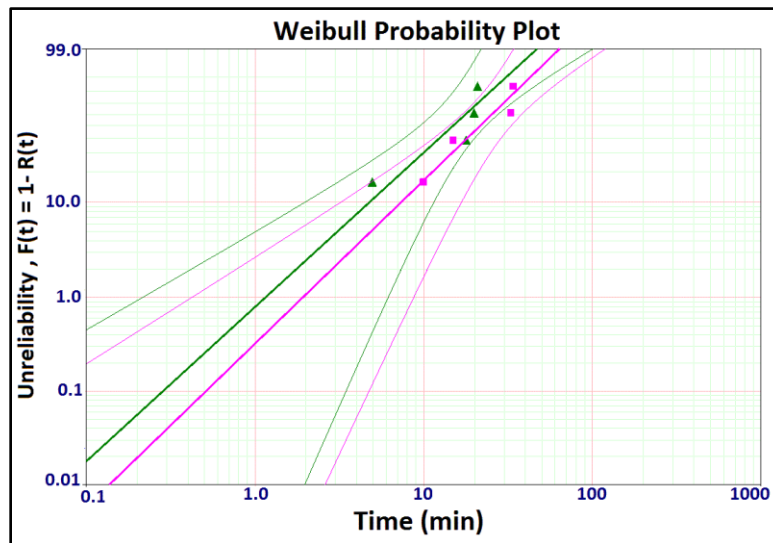
Figure 3.3. Weibull times-to-failure for insulation Groups D(▲) and E(■), with 80% confidence bounds.

3.2.4 **Enamel (Groups F and G)**

Group G demonstrated considerably higher voltage endurance compared to Group F (Figure 3.4), which could be due to differences in the type of enamel. Further studies, such as repeating the experiment using lower voltage stresses, are required, as the stress level for these groups is considered too high due to using the same test voltage level for all groups.
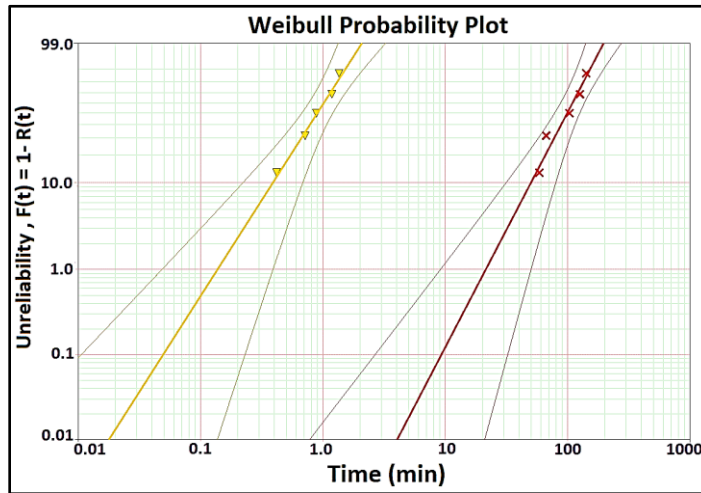
Figure 3.4. Weibull probability plots for Groups F (▼) and G (×), with 80% confidence bounds.

3.2.5 **Examination of Failure Sites**

Figure 3.5 shows the failure sites for two samples from Groups A and B. As can be seen, the failure is mostly at the edge of the strand rather than between two strands for the dissected samples. This may be due either to higher stress at the radius of curvature or to the presence of air pockets at the edge. Figure 3.5a confirms the existence of air pockets, which may result from the loss of VPI resin. The presence of an air pocket results in field enhancement, leading to PD inception and ultimately failure. Figure 3.5b shows a short-circuit between the top-left side of the left strand and the top-left side of the right strand. Such a footprint suggests the creepage current over the outer insulation tape.
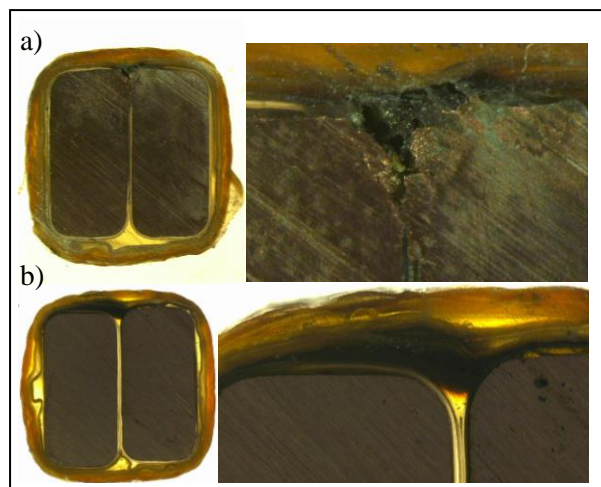
Figure 3.5. Failure sites in samples from Groups A (top) and B (bottom).

54

3.3 The Effect of Pulse Parameters on Time-to-failure of Back-to-back Turn Insulation Samples

The research work presented in this section examines the effect that rise time, duty cycle, switching frequency, and amplitude of square waves have on the lifespan of motor stator coil turn insulation. Back-to-back samples with enamel insulation, as presented in Group G in Table 2.2, are prepared according to the procedure described in section 2.5 to conduct the following experiments. Table 3.3 provides the details of the test parameters for the different test conditions.

Table 3.3. Test parameters for different test conditions

Case Study Group	Peak Voltage (kV)	Rise Time (µs)	Duty Cycle (%)	Switching Frequency (kHz)	Pulse Type
I	2.5	0.27	50	3.0	Unipolar
J	2.5	4.50	50	3.0	Unipolar
K	6.0	0.27	50	3.0	Unipolar
L	6.0	4.50	50	3.0	Unipolar
M	6.0	0.27	15	3.0	Unipolar
N	6.0	4.50	15	3.0	Unipolar
O	6.0	4.50	85	3.0	Unipolar
P	6.0	4.50	43	8.3	Unipolar
Q	5.2	0.27	50	3.0	Unipolar
R	4.5	0.27	50	3.0	Unipolar
S	4.0	0.30	50	0.5	Unipolar
T	4.0	0.30	50	1.0	Unipolar
V	4.0	0.30	50	3.0	Unipolar
W	4.0	0.30	50	0.5	Bipolar
X	4.0	0.30	50	1.0	Bipolar
Y	4.0	0.30	50	3.0	Bipolar

3.3.1 **Effect of Rise Time on Aging**

Two sets of samples were aged at a peak voltage of 2.5 kV and a switching frequency of 3 kHz. Rise times of 270 ns were allotted for case study I and 4.5µs for case study J. Prior to commencing the aging procedure, the PDIV was measured at 1.7 kV peak and the times-to-failure were recorded. The Weibull results are shown in Figure 3.6. The shape parameters for case studies I and J were found to be 1.5 and 1.4, respectively, which is greater than 1.0, so the failure is due to aging. On the other hand, the overlapped confidence bands of these two case studies suggest that rise time may not play a significant role in aging.

During the aging, online PD measurements were taken every 5 minutes and stored using the persistent mode of the oscilloscope (Figure 3.7). PD signals that occurred multiple times at the same location are shown using colour spectrum; white indicates the highest number of pulses, while red represents a low concentration of pulses. The results show increased PD with higher magnitudes on the front of the square wave.
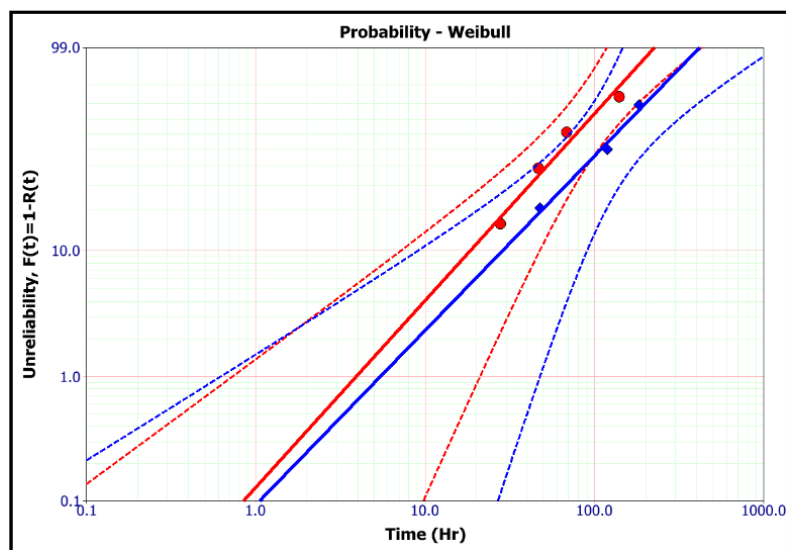
Figure 3.6. Weibull times-to-failure with 50% duty cycle square waves at 3 kHz switching frequency and 2.5 kV peak; with 270 ns rise time (.) and with 4.5µs (♦), considering 90% confidence bounds.

Figure 3.7 also shows a PD of about six times higher magnitude for 270 ns rise time waves than for 4.5 µs rise time waves. Therefore, due to the higher PD pulses, one may speculate that the faster rise time pulses should age the insulation faster than the slower rise time pulses. However, from Figure 3.6, both rise times show little, if any difference, in the times-to-failure. This anomaly may be explained by

examining the occurrence of PD on the DC portion of the pulses, which suggests that regardless of the difference in PD severity on the rise time, the characteristic life is governed by the PD on the DC portion of the wave.

The DC portion is considerably longer in duration than the rise time section of the wave. PD occurring during the DC section may be due to accumulation of space charge in the insulation, which needs further investigation. Additionally, the applied voltage is close to the PDIV, which may have altered the results. Therefore, the tests were repeated at a higher applied voltage of 6 kV at different duty cycles.
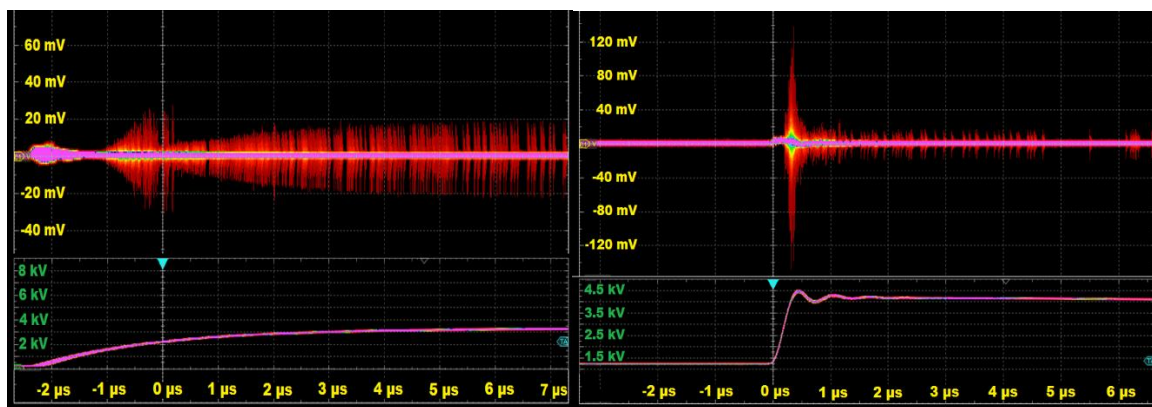
Figure 3.7. Accumulated PD using antenna. The left trace is for a pulse rise time of 4.5 µs with 20 mV/div of PD and 1 kV/div of voltage, and the right trace is for a pulse of 270 ns rise time with 40 mV/div of PD and 500 V/div of voltage; both 1µs/div of time.

The peak voltage of the square wave was kept at 6 kV, with a 50% duty cycle and a switching frequency of 3 kHz. The two rise times considered (270 ns and 4.5 µs) correspond to case study Groups K and L. These rise times were selected as a means of producing a wide range of times-to-failure while maintaining a reasonable acceleration factor. Before aging, the PDIV of the five samples for each test averaged a peak voltage of 1.7 kV. Figure 3.8 shows the Weibull distributions, with 90% confidence bounds for case study Groups K and L. Because the confidence bounds intersect, it can be inferred that the aging is independent of the rise time within the range studied.

To examine the effect of the DC component of the pulse on the time-to-failure, the DC component was reduced from 150 µs to less than 50 µs, i.e., a 15% duty cycle for both rise times. The aging tests were repeated with a 6 kV peak for case study Group M samples, which had a 270 ns rise time, and case study Group N samples, which had 4.5 µs rise time pulses. In order to achieve more accurate

57

results, the number of samples considered per group for this test was increased by two. The results are shown in Figure 3.9. It appears that when the duty cycle was reduced to 15%, the faster rise time resulted in slightly faster times-to-failure, as the separation of confidence bounds occurs in the high percentiles and the slope of the Weibull plots are different. The reduced duty cycle resulted in a longer time-to-failure for both rise times.
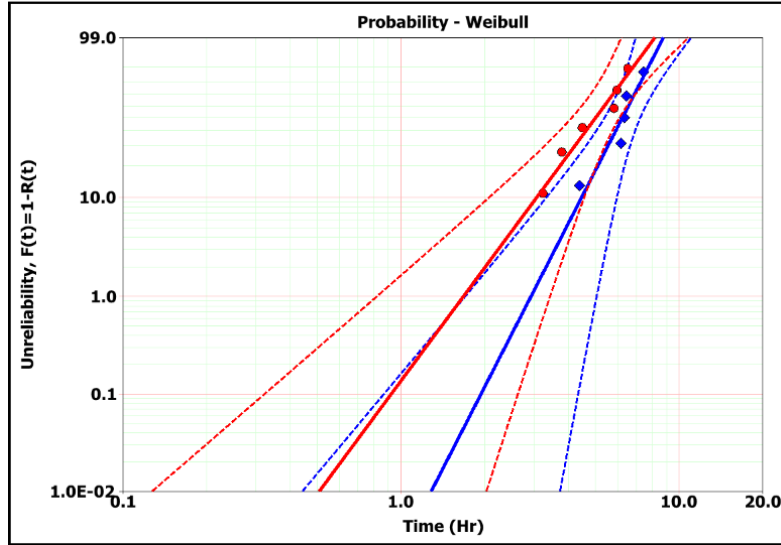
Figure 3.8. Weibull plot with 90% confidence bounds for square waves, 6 kV peak, 3 kHz switching frequency and 50% duty cycle, for 270 ns (♦) and 4.5 µs (●) rise times.
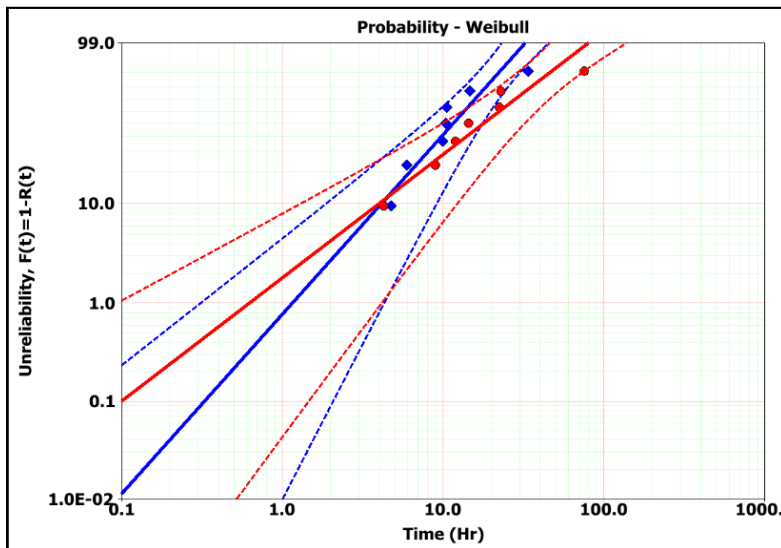
Figure 3.9. Weibull plot with 90% confidence bounds for square waves, 6 kV peak, 3 kHz switching frequency and 15% duty cycle, for 270 ns (♦) and 4.5 µs (●) rise times.

3.3.2 **Effect of Duty Cycle on Aging**

With the applied voltage, switching frequency and rise time kept constant at 6 kV, 3 kHz, and 4.5 µs, respectively, the effect on aging was investigated for duty cycles of 15%, 50%, and 85%. Figure 3.10 shows the Weibull time-to-failure distributions with 90% confidence bounds. The results show that duty cycles of 50% and 85% have essentially identical slopes; however, for the duty cycle of 15%, the slope is greatly reduced, indicating a longer time–to-failure for reduced impulse duration.
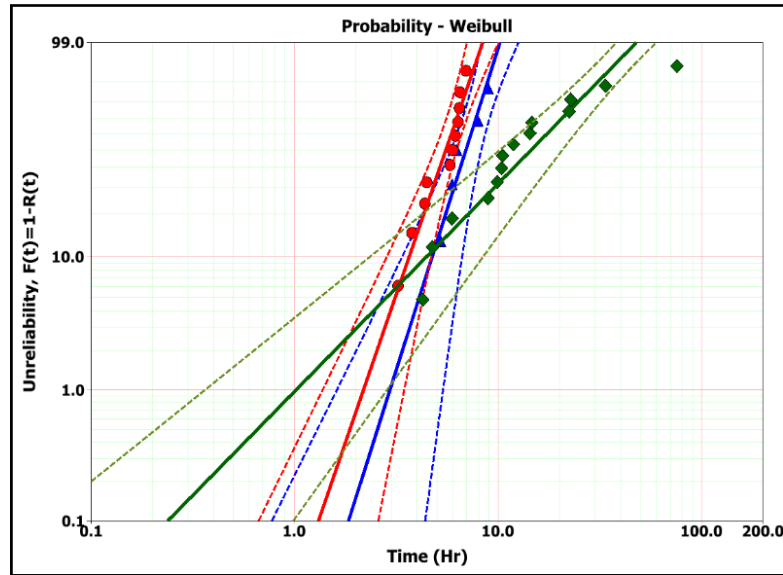
Figure 3.10. Weibull plot with 90% confidence bounds for square waves, 6 kV peak, 3 kHz switching frequency and 4.5 µs rise time, for 15% (♦), 50% (●), and 85% (▲) duty cycles.

3.3.3 **Effect of Switching Frequency and Duty Cycle on Aging**

To examine the effect of switching frequency on time-to-failure, case study Group L samples were aged with 6 kV applied, a 4.5 µs rise time, a 3 kHz switching frequency, and a 50% duty cycle. The results were then compared with those from case study Group P samples, which had 6 kV applied, a 4.5 µs rise time, an 8.3 kHz switching frequency, and a 43% duty cycle. On the basis that the difference between a 50% and a 43% duty cycle would be negligible, a comparison (Figure 3.11) shows similar Weibull slopes for the two frequencies. As expected, the time-to-failure at 8.3 kHz is faster than the results at 3 kHz. However, the times-to-failure does not correspond to the ratio of the two frequencies, i.e., 2.8 and instead, it decreased by a factor of 1.5. This observation suggests the presence of the accumulated charge reducing the slope of degradation at the higher switching frequency.

To further demonstrate the importance of duty cycle, the Weibull time-to-failure distribution for a 6 kV peak, a 4.5 μs rise time, 3 kHz switching frequency, and a 15 % duty cycle is compared in Figure 3.11, which reveals a longer time-to-failure.
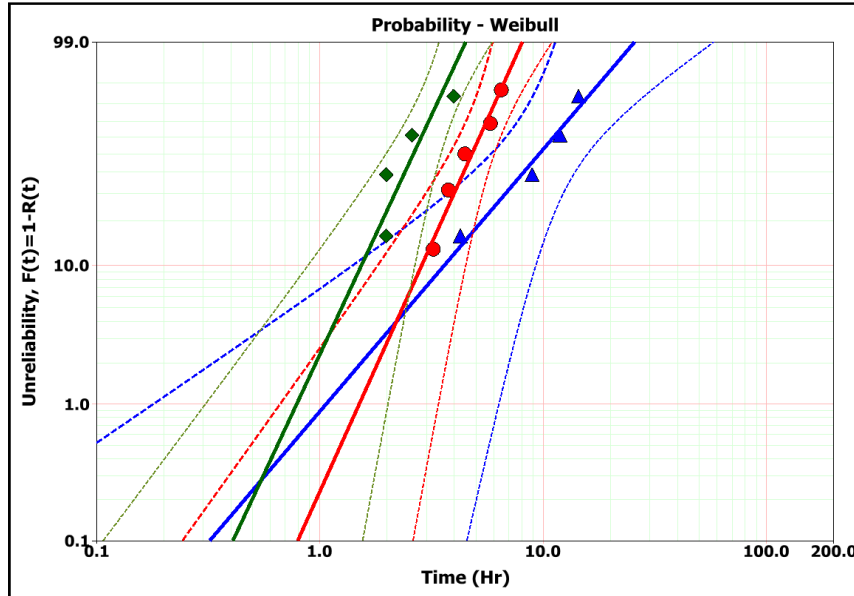
Figure 3.11. Weibull plot with 90% confidence bounds for square waves, 6 kV peak and 4.5 μs rise time; for 15% duty cycle with 3 kHz switching frequency (▲), 50% duty cycle with 3 kHz switching frequency (●), and 43% duty cycle with 8.3 kHz switching frequency (♦).

3.3.4 Effect of Applied Voltage on Aging

With the switching frequency, duty cycle, and rise time of 3 kHz, 50%, and 270 ns, respectively, the applied voltage was varied as a means of observing the effect of applied voltage on the times-to-failure (Figure 3.12).

Three different peak voltage levels of 4.5 kV, 5.25 kV, and 6 kV were considered. It can be seen that the slopes of the Weibull plots are similar for 5.25 kV and 6 kV, but differ for 4.5 kV. This outcome means that increasing the applied voltage from 4.5 to 5.25 kV changes the aging mechanisms, possibly due to exceeding the repetitive PDIV threshold.
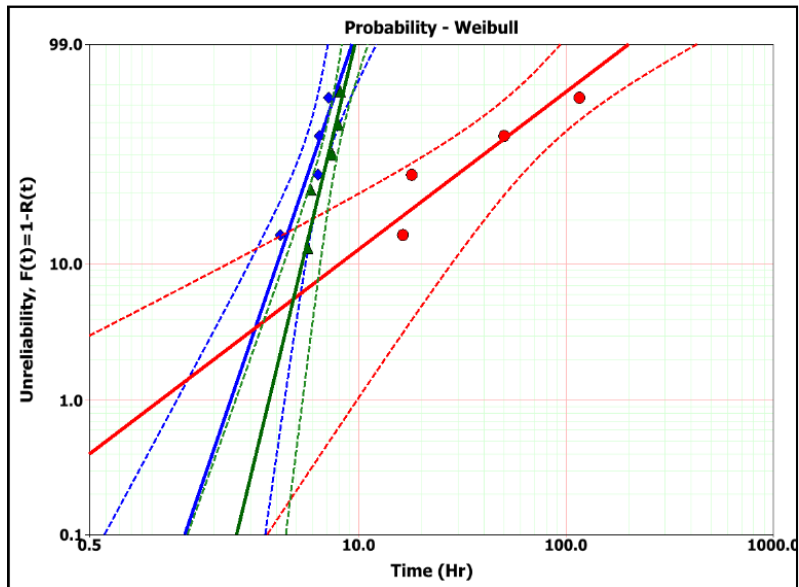
Figure 3.12. Weibull plot with 90% confidence bounds for square waves, 3 kHz switching frequency, 50% duty cycle, and 270 ns µs rise time; for 6 kV (♦), 5.25 kV (▲), and 4.5 kV (●) peak voltages.

3.3.5 **PD Measurements on Back-to-back Samples**

Many researchers [3, 6, 10] have demonstrated that insulation degradation under fast repetitive pulses is mostly due to dV/dt and space charge effects. As such, the PD was measured and analyzed in order to correlate PD features with the time-to-failure results presented in the previous section. The PD was captured with sampling intervals as low as 400 ps in a window of 400 µs in order to ensure that all PD events were captured at high resolution over the full wave of the applied voltage. The lower sampling rate causes the peak of the PD signal to be missed.

Given the above resolution and the available memory of the scope, it was possible to gather 54 waveforms in each batch of PD recordings. The data collected were processed in MATLAB, and the absolute peak amplitude and the location of each PD pulse with respect to the applied voltage were extracted for each waveform. To demonstrate the accumulation of PD events over time, histogram representations of the PD events with respect to the applied voltage were produced for both PD amplitude and PD numbers (Figure 3.13). A window of 5 µs was considered for the accumulation of the PD peak amplitudes (solid trace) and the PD numbers (dashed trace) for all 54 waveforms captured. The cumulative intensity and the number of PD pulses can thus be observed as a function of time and with respect to the applied voltage.

61

It should be noted that the PD amplitude is represented without a dimension because it corresponds to the PD signal strength captured from the antenna and is not the apparent charge; however, it can be used for comparing cases that have the same arrangement. The recorded RF magnitudes are divided by a factor to fit the values using a single Y-axis for both the PD numbers and PD signal strength as PD amplitude.

Figure 3.13 shows phase-resolved histograms of the PD for the pulses with two different rise times and two different duty cycles while the applied voltage was maintained at 6 kV and the switching frequency was fixed at 3 kHz. For ease of comparison, Figure 3.13 shows only the parts of the wave where the PD is present, with discontinuity in time scale (X-axis).

Regarding the fact that the lifetime test results were similar for 50% and 85% duty cycles compared to that of 15%, based on Figure 3.12, the comparison of the phase-resolved PD measurements are presented only for 15% and 50% duty cycles.
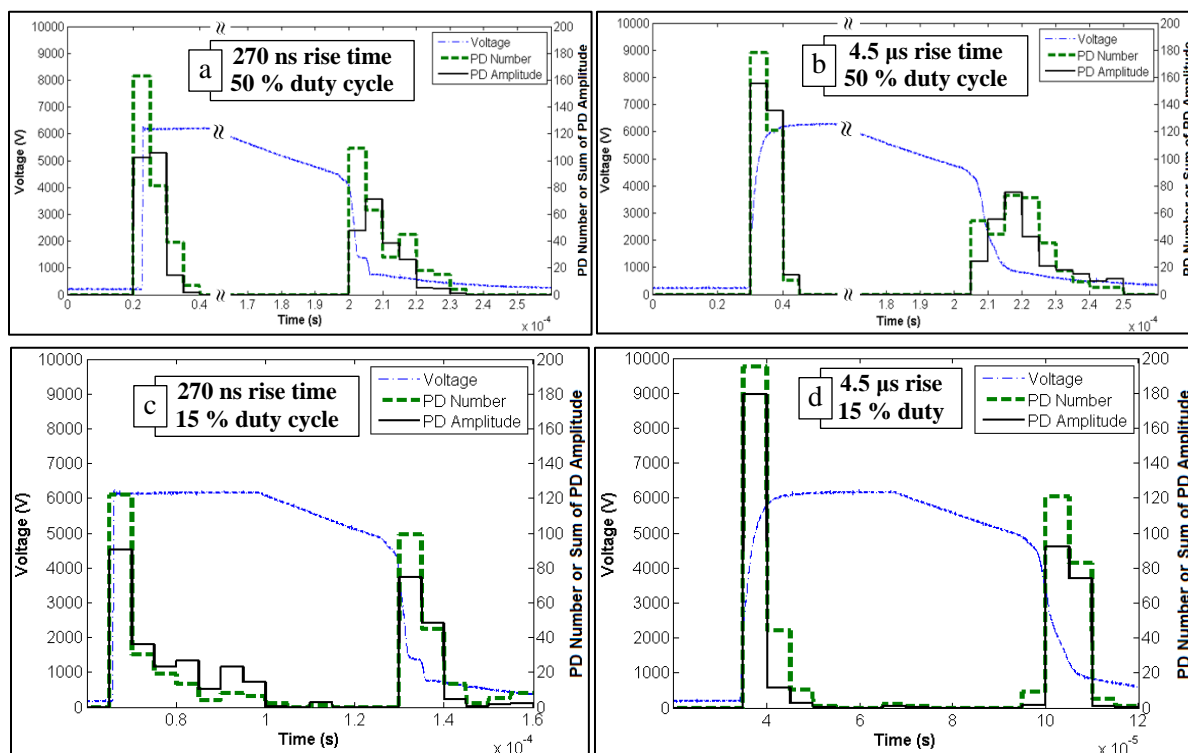
Figure 3.13. Phase-resolved PD measurements at 6 kV and 3 kHz, for different duty cycles and rise times.
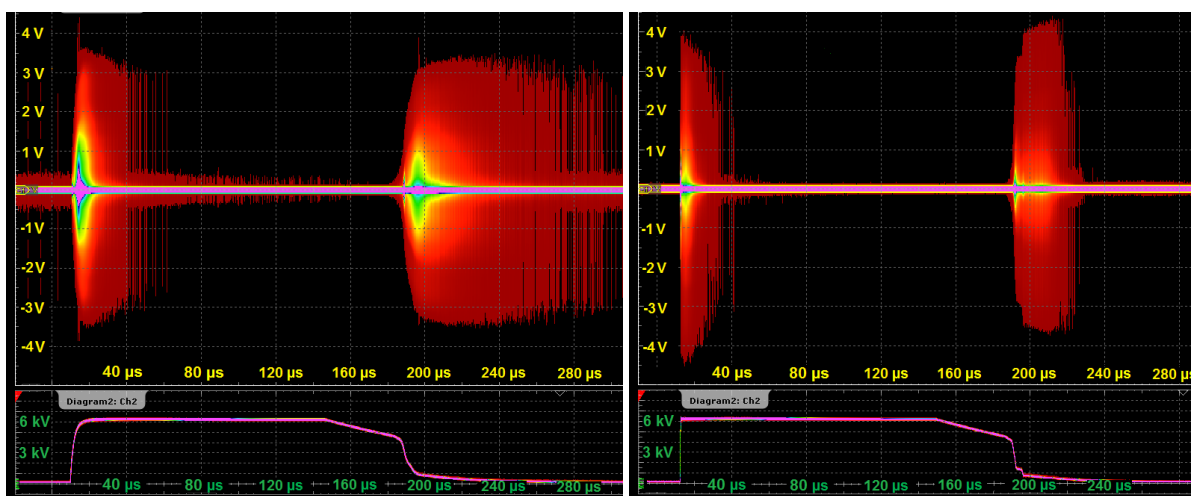
Figure 3.14. Accumulated PD using an RF antenna. The upper trace is for a pulse rise time of 4.5 µs with 1 V/div of PD and 2 kV/div of voltage. The lower trace is for a pulse rise time of 270 ns with 1 V/div of PD and 2 kV/div of voltage; both involve 40 µs/div of time. The brighter traces in the PD signals represent multiple occurrences of the pulses over time. The capture time was 15 min.

Figure 3.14 shows the voltage waveform along with accumulation of PD pulses over 15 minutes of aging. Each PD event is captured and added to the figure. Multiple occurrences of PD events at the same location increase the brightness of the traces. As can be seen, PD pulses mostly occur at the rise and fall times of the wave. This method of representation of PD events provides the capability to compare the pattern of PD as well as maximum PD amplitude over a long period of time. It is evident that the maximum PD magnitude is higher with faster rise time while it is more spread along the waveform with the slower rise time.

3.3.6 Effect of Switching Frequency and Pulse Type on Aging

A unipolar/bipolar pulse generator was employed to investigate the effect of pulse type and switching frequency on times-to-failure of the back-to-back samples. As the maximum output voltage of the bipolar generator was 4.5 kV peak-to-peak, the applied voltage was set to 4 kV for these tests. Three switching frequencies, 0.5, 1.0, and 3 kHz, were used in the study for both unipolar and bipolar square waves, and the applied voltage and rise time were kept constant at 4 kV and 300 ns, respectively. The applied voltage was selected to be always higher than RPDIV for the samples, which ranged from 2.5 kV to 2.8 kV. Case study Groups S to Y in Table 2.2 present the details of the test parameters for the back-to-back sample studies.

The Weibull plots shown in Figure 3.15 compare the time-to-failure of back-to-back samples with respect to switching frequency for unipolar waves with 4 kV peak voltage and 300 ns rise time. The results show that doubling the frequency from 500 to 1000 Hz reduces the life from 55.5 hours to 26.4 hours, which appears to be a linear behaviour. This means that in this frequency range, time-to-failure is a function of the number of cycles applied. However, increasing the frequency from 1 to 3 kHz reduces the life by a factor of two instead of three, suggesting a change in the aging mechanism that occurs above 1 kHz. This observation is in agreement with the results presented in [39] and [16] using twisted enamel wires, which contradicts with the results obtained from the aging of mica-based back-to-back samples in [29].

These experiments were repeated using bipolar square waves at the same switching frequencies, applied voltage, and rise time. As shown in the Weibull plot in Figure 3.16, there is a large difference between the time-to-failure at 500 Hz and the two other frequencies, suggesting a different failure mechanism. As was obtained with unipolar waves, a reduction in life by a factor of 2 was observed when the switching frequency increased from 1 to 3 kHz.
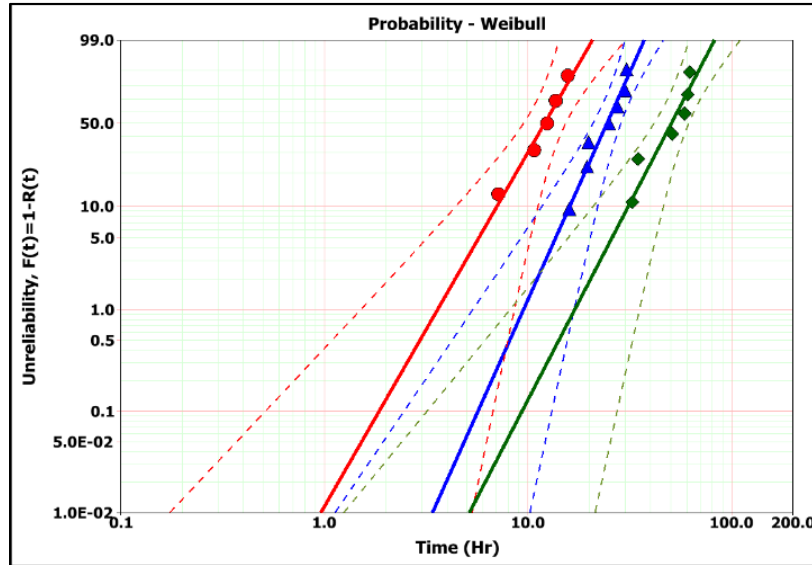
Figure 3.15. Weibull plot with 90% confidence bounds for unipolar square waves, 4 kV peak, and 300 ns rise time; for 0.5 kHz (♦), 1 kHz (▲), and 3 kHz (●) switching frequencies.
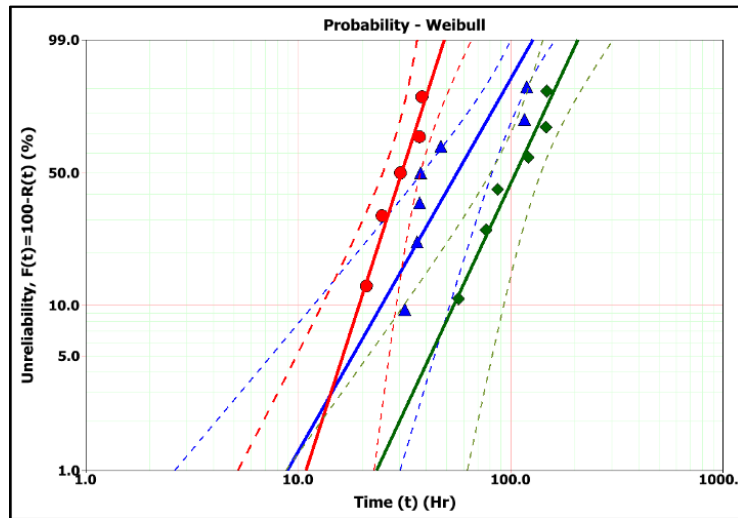
Figure 3.16. Weibull plot with 90% confidence bounds for bipolar square waves, 4 kV peak-to-peak, and 300 ns rise time; for 0.5 kHz (♦), 1 kHz (▲), and 3 kHz (●) switching frequencies.

Figure 3.17 compares the Weibull characteristic life (α scale factor) from Figure 3.15 and Figure 3.16. As can be seen, the life of the back-to-back samples is shorter for unipolar square waves than for bipolar waves; for all three switching frequencies applied. These results are in agreement with those obtained by [41] studying insulating films, but contradict with what was reported in [39], [42], and [43] using twisted enamel wires. The larger interface, which is present in form-wound back-to-back samples and insulation film samples compared to twisted enamel samples, could result in different amounts of space charge accumulation and PD behaviour and thus alter the aging results.
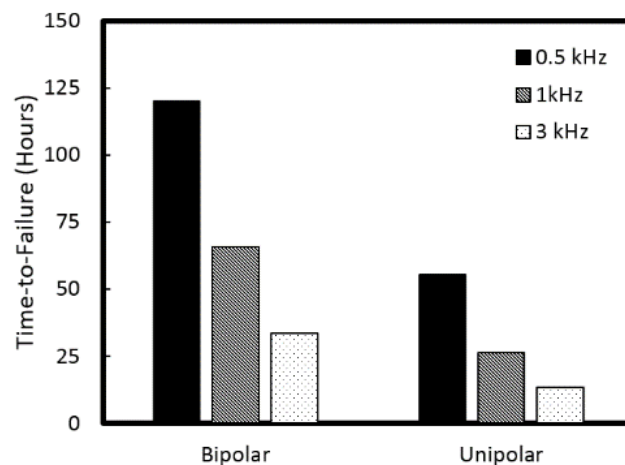
Figure 3.17. Time-to-failure of back-to-back insulation samples for bipolar and unipolar square waves, 4 kV peak, 300 ns rise time, and at 0.5, 1 and 3 kHz switching frequencies.

65

3.3.7 **FEM Simulation Results of Turn-to-turn Sample**

Electrostatic simulation is employed to investigate the electric field across the sample under various conditions. Figure 3.18a shows the field distribution across the sample when the input voltage is 20 kV. As can be seen, the electric field distribution is smooth at the straight section; whereas, enamel experiences a higher electric field due to its lower permittivity compared to mica. However, a considerably enhanced field at the crotch of the sample is evident in Figure 3.18b. The field enhancement at the crotch is not desired, as higher stress and breakdown will take place in the crotch rather than along the sample.

If the sealant epoxy is not applied properly resulting in an air gap at the crotch, the electric field will be high. This problem is simulated by adding a piece of glass in the geometry to leave an air gap in the joint between the insulation tapes and the sealant (Figure 3.19a). The result confirms an electric field reaching 8.3×10^6 V/m in the crotch (Figure 3.19b), confirming the failure problem and the necessity of filling the crotch properly.
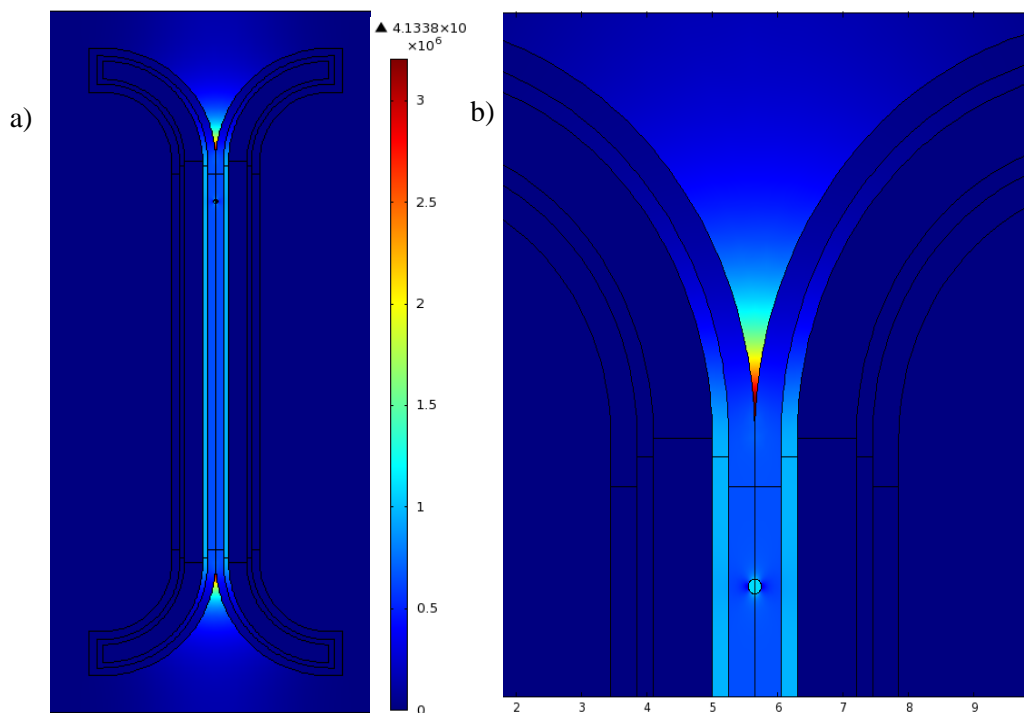
Figure 3.18. (a) Electric field distribution in the back-to-back sample with the applied voltage of 20 kV; (b) undesired field enhancement at the crotch.

66
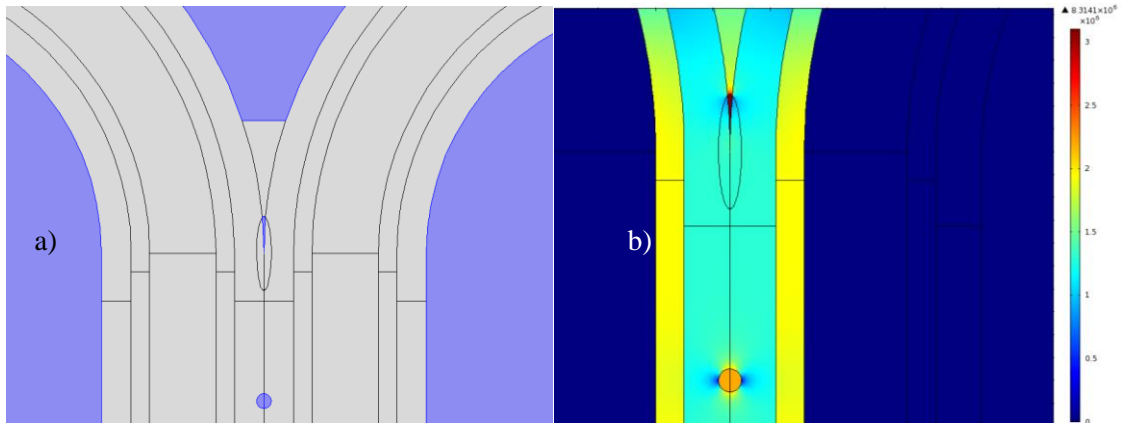
Figure 3.19. (a) Adding a sealant with air gap in the geometry; (b) simulation results indicating further field enhancement due to the incomplete fill of the crotch.

Figure 3.20 shows the smoothened electric field reduced to less than 2×10^6 V/m in the crotch by filling the gap completely. In this case, the highest electric field occurs in the air bubble located between the two insulation layers. Therefore, the aging and failure would shift to the straight section rather than to the crotch.
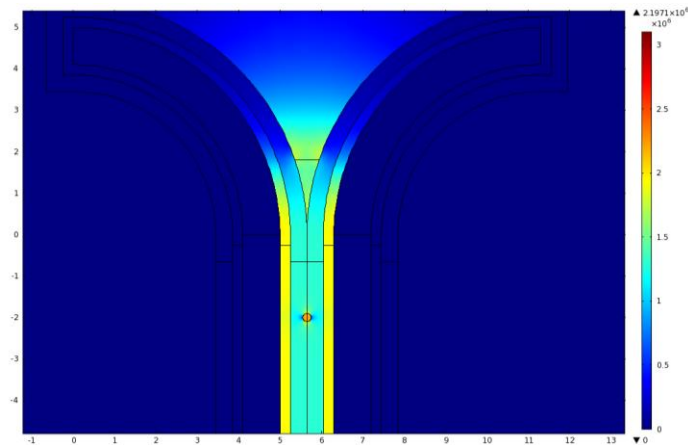
Figure 3.20. Smoothened electric field at the crotch by adding sealant.

Figure 3.21 shows the distribution of the electric field on the reference line across the sample. As can be seen, the highest electric field occurs in the air bubble, where there is a significant difference in permittivity in the presence of voltage and thus results in enhancing the electric field. The enhanced electric field at the crotch is due to differences in the permittivity of the insulating materials.

67
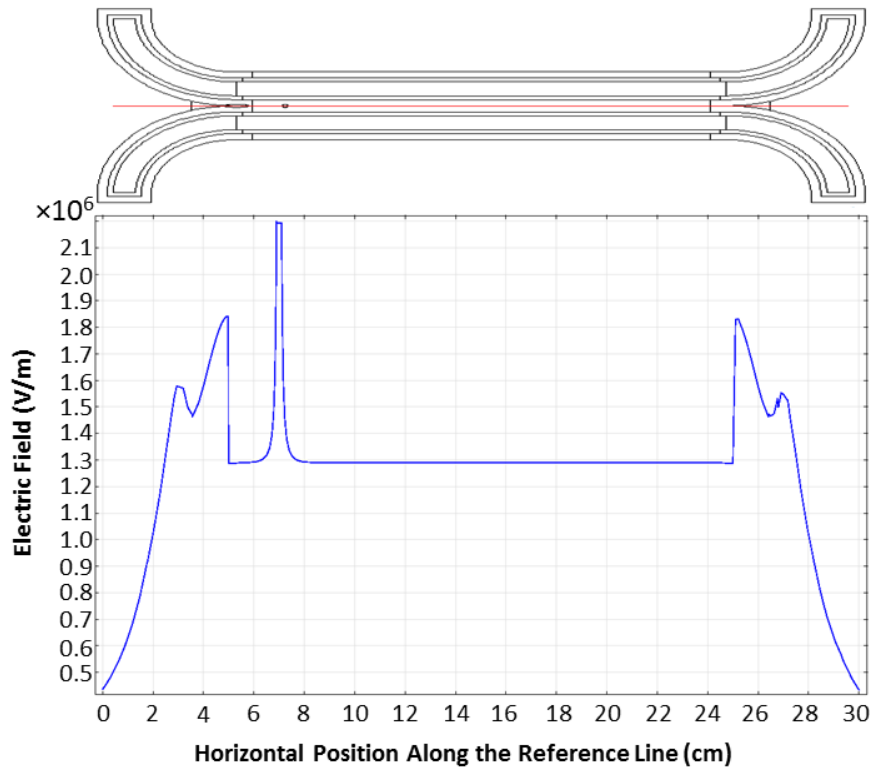
Figure 3.21. Electric field distribution along the sample on the red cutline shown on the top figure.

Figure 3.22 shows the electric field inside the air bubbles with different sizes. The radius was varied between 0.4 mm to 2 mm when applying a fixed voltage of 20 kV and the electric field was measured at the centre of the bubble. As can be seen, the smaller bubbles have a higher electric field, which is due to the higher gradient of the voltage.
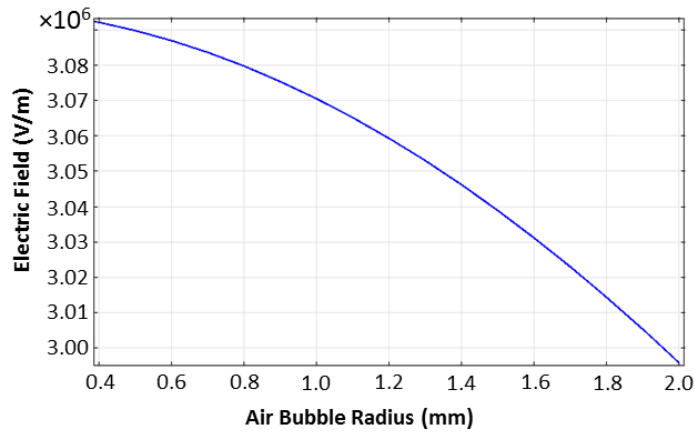
Figure 3.22. Electric field inside the bubbles with different sizes at a constant input voltage of 20 kV.

Time domain simulation was employed to observe temperature rise in the sample due to dielectric current and dielectric heating. A train of square pulses was generated and applied to the sample. Figure 3.23 shows a single pulse using the "rect" function in COMSOL®, where a pulse width of 0.8 µs and rise time of 300 ns are considered.
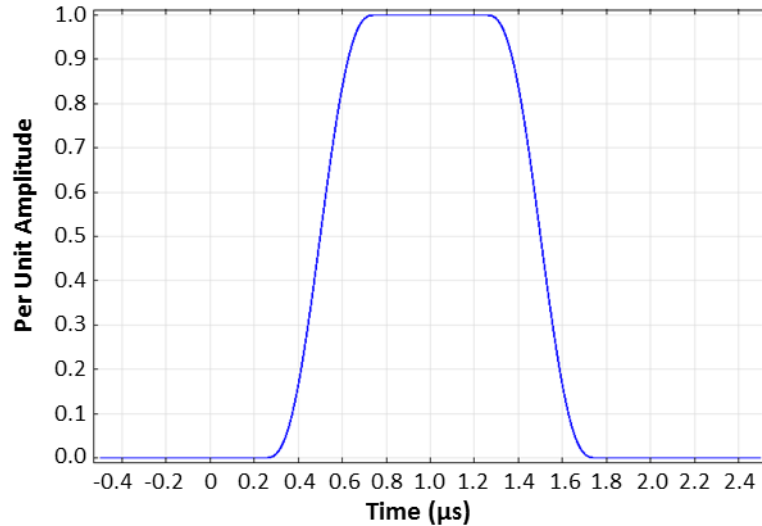
Figure 3.23. Square pulse generated in COMSOL® and applied as input pulsed voltage.

To generate a train of pulses, a mathematical term was added to the function, as follows:

$$Vin*rect(mod(t,2e\text{-}6))\ [1/s]$$

where Vin is the voltage peak of the pulse equal to 20kV.

The simulation result of the electric field varying with time is shown in Figure 3.24, with the simulation time increasing from left to right. As can be seen, the electric field follows the pulse shape as expected. The simulation results for the current density are also shown in Figure 3.25, where the capacitive current pulses during transients of the voltage can be observed.

The results shown in Figure 3.25 can be confirmed by plotting the applied voltage at the high voltage side and the current density along the *x* axis at the ground side. Figure 3.26a shows the simulated pulsed voltage and current of the sample. The results show a good agreement compared to the experimental results obtained from testing a turn-to-turn sample in the lab (Figure 3.26b).
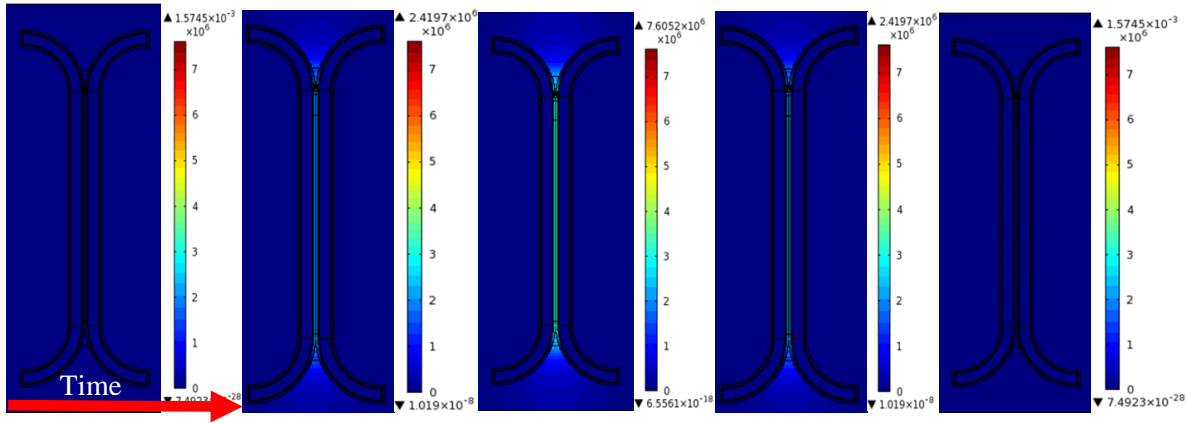
Figure 3.24. The variation of electric field with application of a square pulse over time.
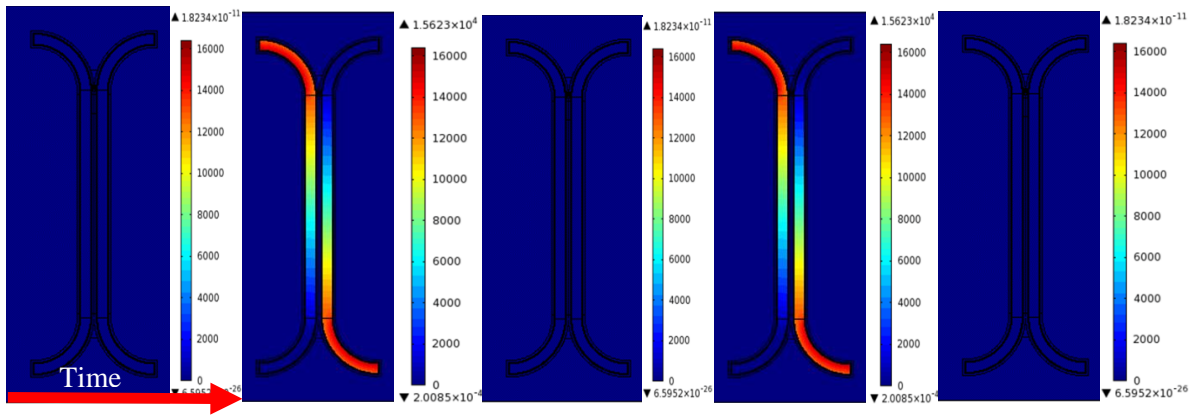
Figure 3.25. The variation of the current density with application of a square pulse over time.
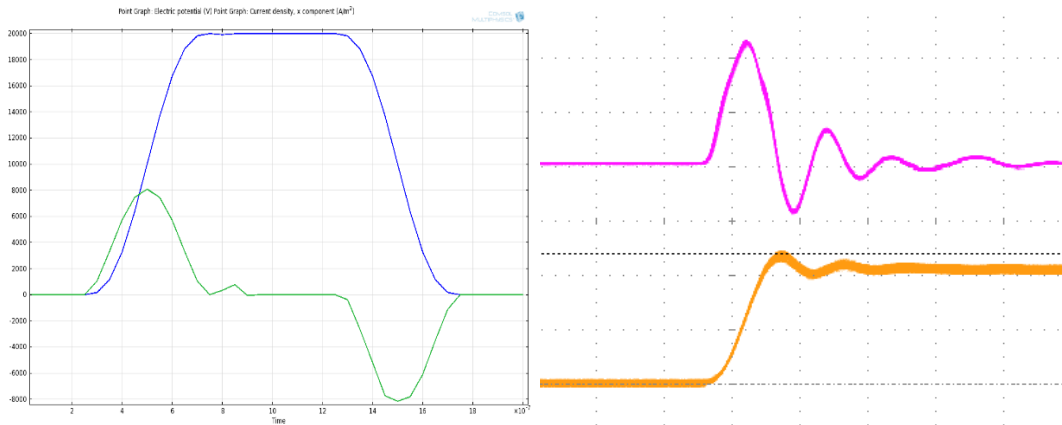
Figure 3.26. (a) Simulation results of voltage (blue) and current (green) of the sample; (b) experimental results of voltage (orange) and current (pink) of the sample in the laboratory.

70

As mentioned previously, a train of pulses was prepared and applied to the sample. The simulation was executed for hundreds of pulses. Figure 3.27 shows the voltage and current of the sample for several pulses.
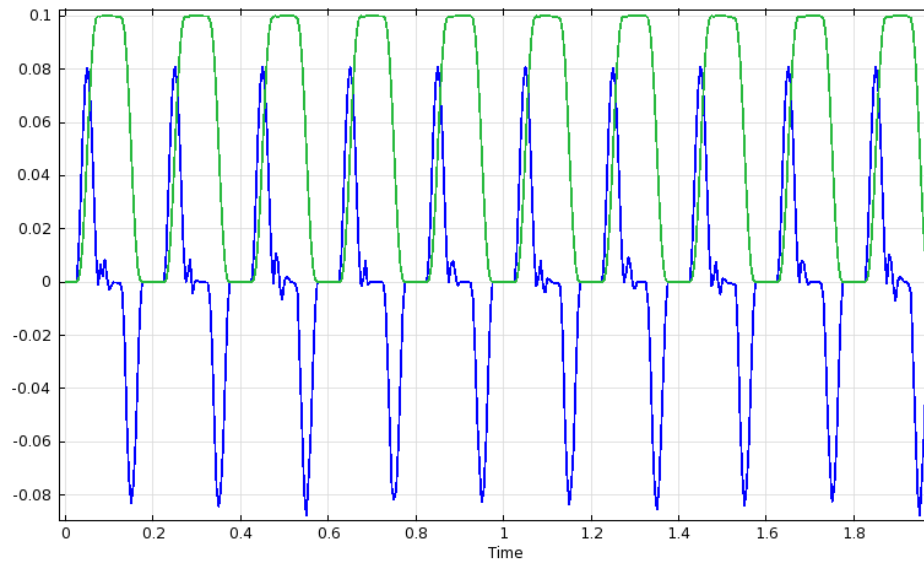
Figure 3.27. Train of pulses applied to the sample (applied voltage: green and current: blue).

Figure 3.28 shows the temperature of the sample during 30 seconds of the simulation under pulse stress when applying square pulses with an amplitude of 20 kV.
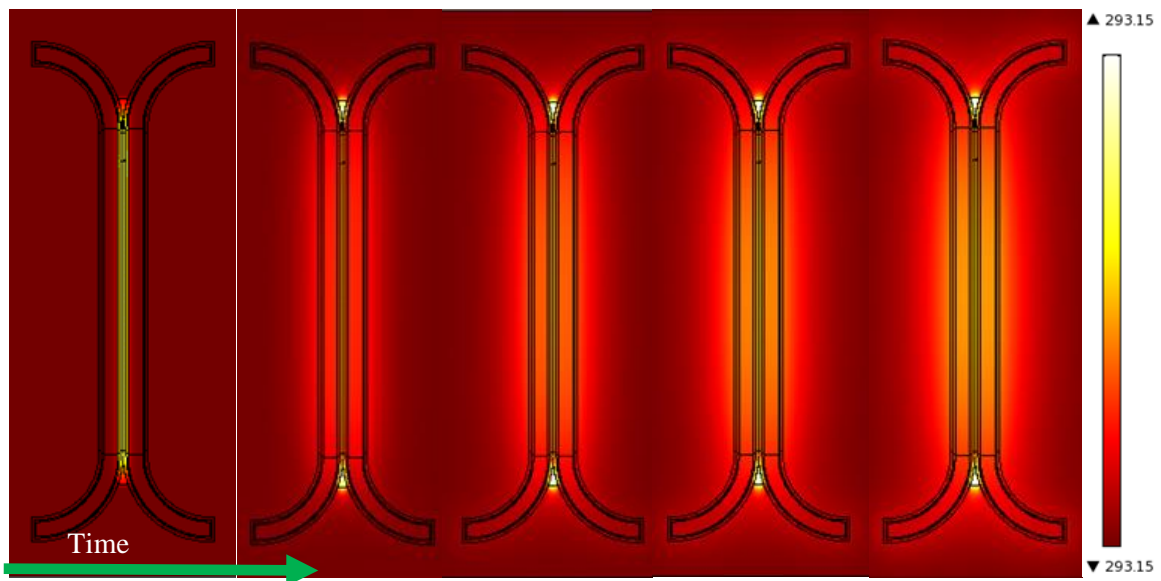
Figure 3.28. Temperature distribution as a function of time in the sample under pulse stress.

71

Although the above results appear to adequately show the concept, the temperature increase is not significant in this case. To observe the steady-state temperature, the simulation must be run for a long time using a very fine step, which is extremely time-consuming. The results can be confirmed by the data recorded using an infrared camera during aging of the samples (Figure 3.29).
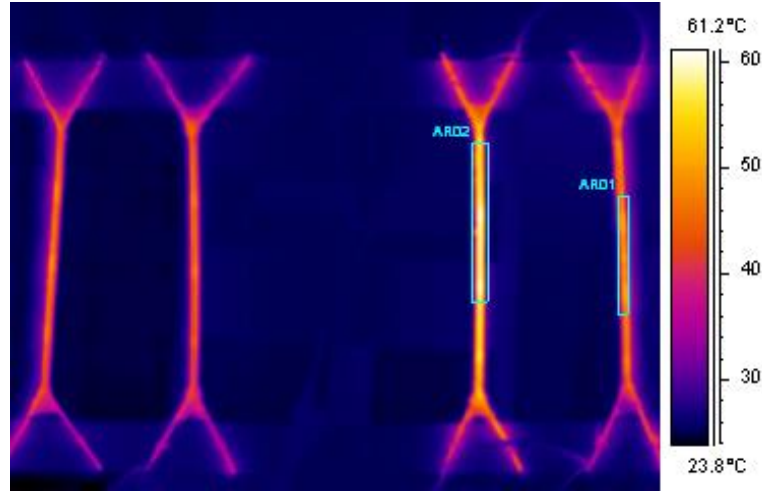
Figure 3.29. Measured temperature distribution during a test captured by an infrared camera.

Using the results of the simulation, post-processing and evaluation of the dissipation factor, tan δ, stored energy, capacitance and parametric studies (such as variation of capacitance or other parameters with variation of thickness or permittivity) can be done. As an example, the capacitance of the sample is extracted using COMSOL®. Knowledge of the capacitance of the sample is important because it can be used to calculate the total number of the samples that can be simultaneously tested with the PWM generator. It should be noted that the generator can handle only a certain capacitance load.

A voltage of 20 kV in this simulation was applied to the sample with enamel thickness and turn insulation thickness of 0.1 mm and 0.2 mm, respectively. The total charge, Q, was found by integrating the charge density over the sample area, using the COMSOL® post-processing option:

$$Q = \iint_S \rho_s ds = 9.5707 \times 10^{-6}$$

Having Q and V, the capacitance can easily be found using the following relationship:

$$Q = C\,V$$

Hence:

72

$$C = \frac{Q}{V} = \frac{9.5707 \times 10^{-6}}{20000} = 4.785 \times 10^{-11} = 47.85 \, pF$$

This result is in the range of a typical capacitance of a turn sample. Knowing that the PWM generator can handle a maximum capacitance of 400 pF, and using the above-mentioned results, it is possible to test up to 8 of these samples in parallel (8*47.85 = 382.8pF).

3.4 Fundamental Studies on Point-to-plane Setup with Insulation Film Barrier Stressed under Square Waves

Point-to-plane setup with insulation film provided a controlled environment and geometry with single source of PD, which was employed to investigate the charge accumulation and PD occurrence in greater detail. The effect of environment parameters such as humidity and temperature on PD features was also examined. The following subsections present the results.

3.4.1 Observation of the Effect of Space Charge Using Times-to-failure Examination of Films with Different Surface Resistivities

As the surface resistivity of insulating materials is known to affect the build-up of space charge on the surface of insulating materials, thereby modifying PD features and the time-to-failure, a comparison was made to examine the effect of surface resistivity (and thus the space charge accumulation) using two insulation films having ten orders of magnitude difference in the surface resistivity.

PA6 and PTFE films (Table 2.3) were stressed using unipolar square waves with a switching frequency of 3 kHz. The applied voltage was 3 kV for PTFE, which was selected to ensure that PD occurs at each pulse, as the measured RPDIV was 2.3 kV. The PDIV for both films was approximately 2.0 kV, and there was no noticeable change in PD behaviour over the aging time.

Figure 3.30 shows the dimensional details of the point-to-plane setup. Using the following relation, the electric field in gap E_0 is calculated to be 10.1 kV/mm. Hence, by the use of COMSOL® simulation, the maximum electric field at the tip of the electrode was estimated to be equal to 14.1 kV/mm for PTFE. Keeping the electric field the same for PA6, without the space charge field, the applied voltage is calculated to be 2.8 kV.

$$E_0 = \frac{V}{\frac{\varepsilon_0}{\varepsilon_1} d_1 + d_0}$$

73
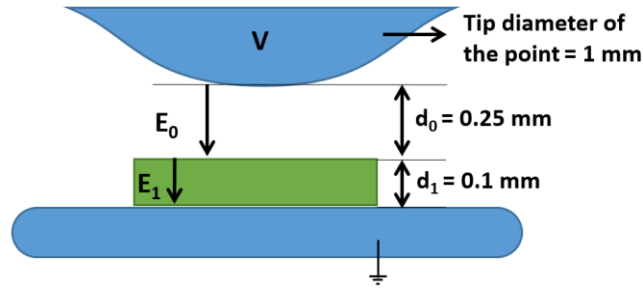
Figure 3.30. Dimensional details of the of point-to-plane setup with insulation barrier.

Figure 3.31 shows the Weibull results for the time-to-failure for five samples in each group that was tested. The slopes of the failure distribution are the same, suggesting that the failure modes are similar, i.e., by PD. Furthermore, the results suggest that the difference in life can be attributed to the development of a space charge field that is in opposition to the applied electric field.
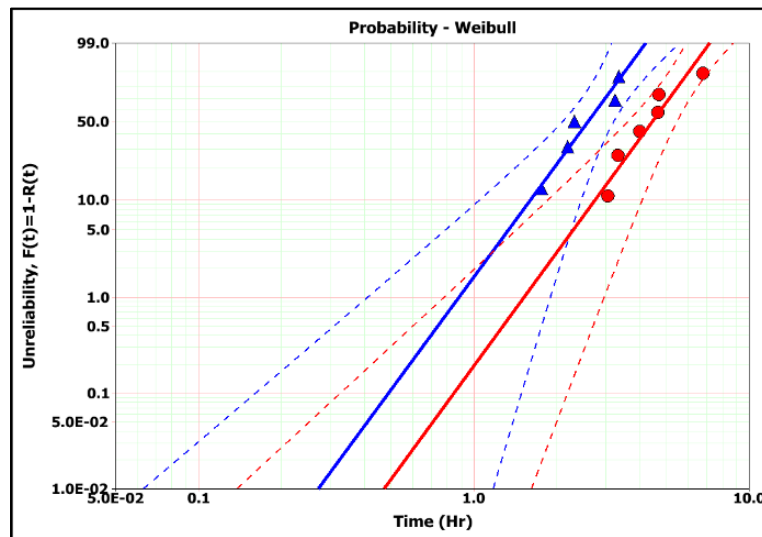
Figure 3.31. Weibull plot with 90% confidence bounds for unipolar square waves, 3 kHz switching frequency, and 300 ns rise time; for 0.1 mm thick PA6 film with 2.8 kV applied and surface resistivity of 5×10^{10} Ω/Sq (▲), and 0.1 mm thick PTFE film with 3.0 kV applied and surface resistivity of 10^{17} Ω/Sq (●).

The time-to-failure tests were repeated for PA6 film at several lower applied voltages, with the same square wave parameters of 300 ns rise time and 3 kHz switching frequency to determine the voltage at which the time-to-failure becomes equal to that of the PTFE stressed at 3 kV. Through trial and error, it was determined that 2.4 kV unipolar square wave gave the same time-to-failure as for 3 kV on PTFE

film. So, the total reduction of 0.6 kV can be attributed to the effect of a dielectric constant (0.2 kV) and a 0.4 kV space charge accumulation on the PFTE surface, as compared to that of PA6.

3.4.2 PD Measurements on Insulation Films and its Relation with Back-to-back Samples

PD measurements on the back-to-back samples were found to be inconsistent from sample to sample, which was attributable to voids having a multitude of locations and sizes. To better understand the relationship of PD to time-to-failure, the point-to-plane setup with insulation film that represents a single void in the back-to-back samples was used to examine the PD parameters on the time-to-failure. In both experiments, the insulating layer is polyimide (back-to-back samples with enamel on the strands and Kapton® (Table 2.3) film in the point-to-plane tests) and has the same surface conductivity and permittivity; these are the parameters that influence the surface space charge accumulation and electric field in the void. Therefore, it is reasonable to assume that PD measurements on the Kapton® film would be the same as those on the back-to-back samples when both are exposed to the identical square wave. Therefore, the single cavity setup was used to observe the PD features of highest PD magnitude, PD_{max} and the rms of the PD signals in a 1 ms window, PD_{rms}. As PD_{rms} contains both the magnitude and the number of PD pulses, it represents the total energy released by PD in a 1 ms window.

Although PD_{max} was sporadic, PD_{rms} stabilized after about three minutes (Figure 3.32). Hence, a five-minute capture interval was used to study the relationship between the PD features in the point-to-plane experiment and time-to-failure of the back-to-back samples when the exact same pulse parameters are applied.
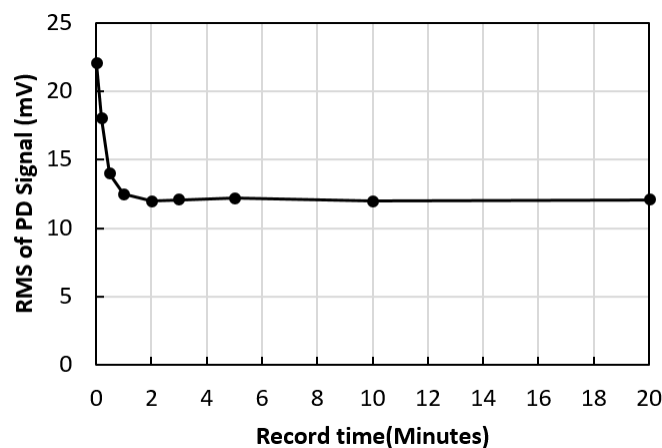
Figure 3.32. Progression of PD_{rms} with time for 3 kV unipolar square waves and 1 kHz switching frequency on Kapton® film insulation in the point-to-plane experiment.

75

Table 3.4 presents the results from the back-to-back samples with a 3 kV peak, 300 ns rise time, bipolar and unipolar square waves, and at 0.5, 1 and 3 kHz switching frequencies. As can be seen, there is no direct relationship between PD_{max}, which represents the highest intensity of the discharge during the five-minute recording interval and the time-to-failure. However, PD_{max} for unipolar square waves is higher than that observed for bipolar waves. A trend was, however, observed between the PD_{rms} and the time-to-failure. This shows that the main parameter of the time-to-failure is the total energy of the PD.

Table 3.4. PD_{max} and PD_{rms} from the single cavity point-to-plane experiment for 3 kV peak unipolar and bipolar square waves and 300 ns rise time compared to the time-to-failure of the back-to-back samples under the same conditions

Switching Frequency (Hz) / square wave	PDmax (mV) Point-to-plane	PDrms (mV) Point-to-plane	Weibull Characteristic Life in Hours (α scale factor) for Back-to-back Samples
500/ unipolar	47.7	4.5	55.5
1000/ unipolar	38.2	11.3	26.4
3000/ unipolar	29.8	15.3	13.4
500/ bipolar	29.2	1.8	120.0
1000/ bipolar	25.5	8.4	65.6
3000/ bipolar	20.0	12.8	33.5

3.4.3 PD Occurrence on Point-to-plane Setup

There was concern about the occurrence of PD from the edge of the film to the plane electrode due to the surface charge. The following presents the evidence to show that the PD occurs only at the tip of the electrode. The Kapton® sheets with two different sizes, as shown in Figure 3.33, were aged under unipolar pulses, with 3 kHz switching frequency with an applied peak voltage of 3 kV.
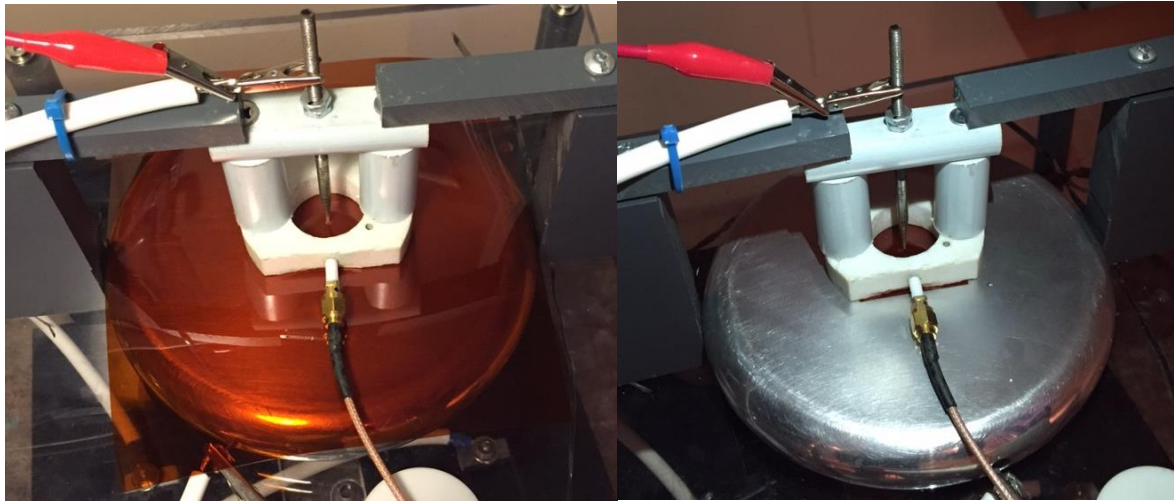
Figure 3.33. Aging Kapton® sheets with different dimensions.

The rms of PD signals was similar, as illustrated in Figure 3.34, after five minutes of stressing. After three hours of aging, the PD patterns deviated and a higher number of PD pulses was observed on the flat portion of the square wave for the sheet with the larger surface, while discharges at the transients was observed on the smaller sheet (Figure 3.35). Having the same peak PD level at the transients on both sheets suggests that the larger sheet is capable of collecting more charge over time. However, the time-to failure measurements came out equal for both sheets, and thus there was no indication that there is any discharge from the sheet to the grounded plane.
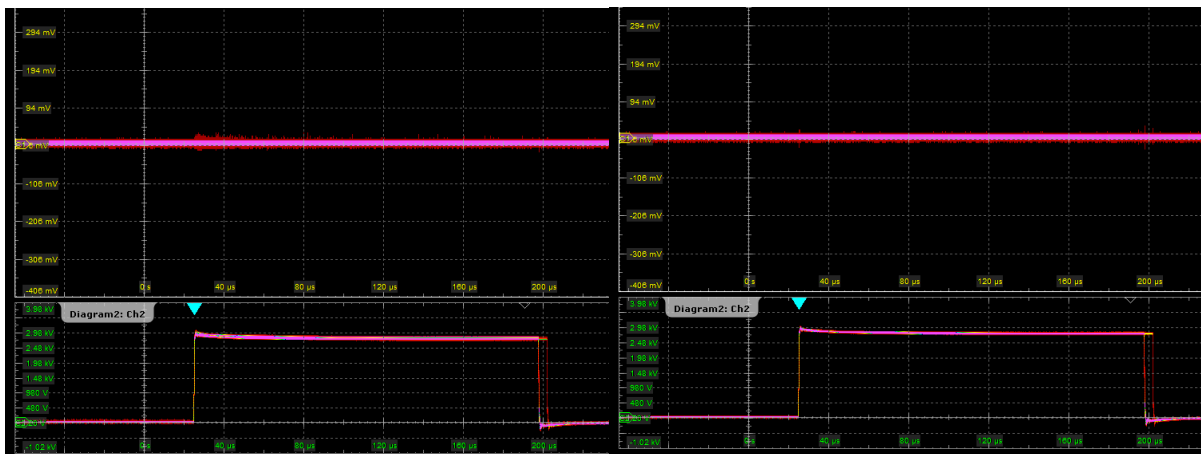
Figure 3.34. PD pattern after three minutes of aging: Left: 150 mm sheet; right: 37.5mm sheet.
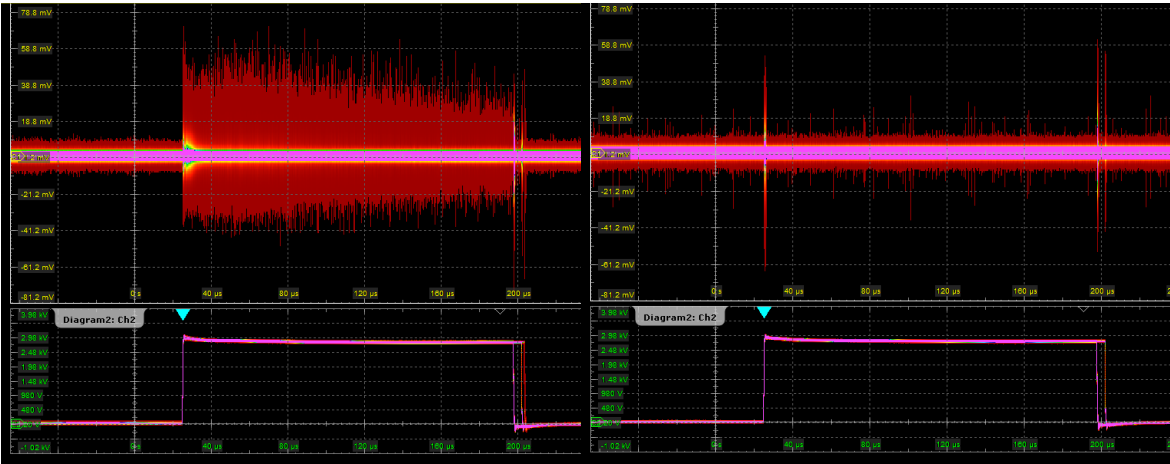
Figure 3.35. PD pattern accumulated after three hours of aging. Left: 150 mm sheet; right: 37.5mm sheet.

3.4.4 Surface Potential Measurements Using Non-contact Probe

To establish the rate of dissipation of deposited charge on the dielectric film, which is mainly due to PD rather than conduction over the surface, a PTFE film was pulse stressed for five minutes at 3 kV unipolar square wave and switching frequency of 3 kHz. The surface potential was then measured using the non-contacting potential probe as a function of time. As shown in Figure 3.36, the accumulated surface charge decays to one half after about four hours. The result demonstrates that measuring the surface potential shortly after removing the generator from the setup after pulse stressing does not introduce significant error to either the measurement of surface potential or the surface charge.

Based on the observation of a very slow decay of surface charge, each film was pulse-stressed with unipolar and bipolar square waves at a switching frequency of 3 kHz for five minutes, and the potential profile was measured with the non-contacting probe. The applied pulse voltage was adjusted according to capacitance so that the calculated maximum electric field in the gap at the tip of the point electrode was maintained at 14.1 kV/mm.

78
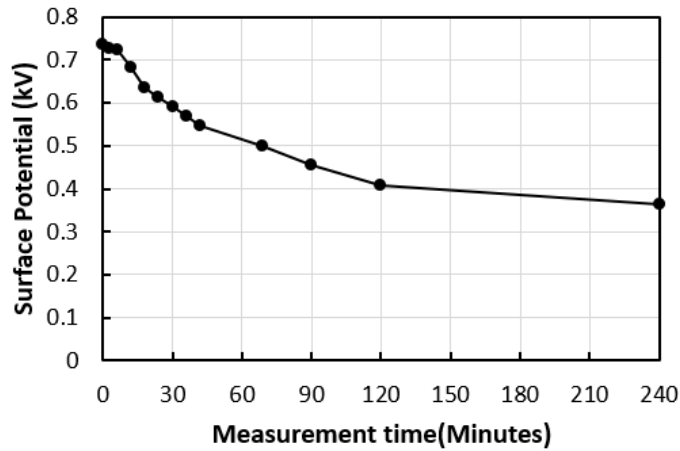
Figure 3.36. Surface potential measured using a non-contacting potential probe on the PTFE film after pulse stressing at 3 kV, unipolar square wave, and switching frequency of 3 kHz, for five minutes.
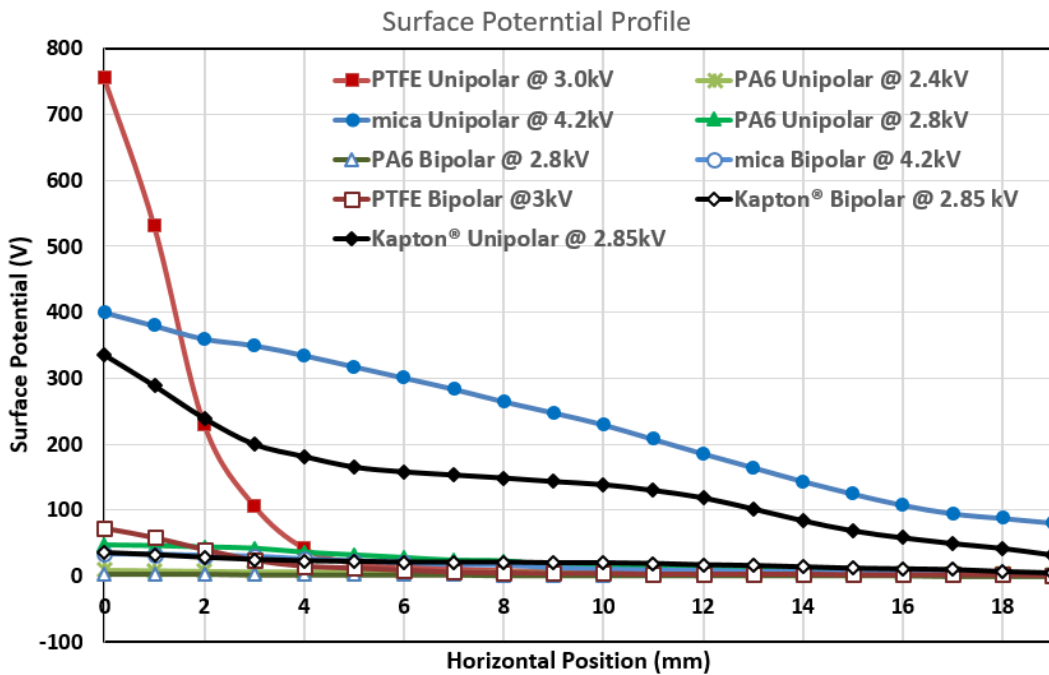
Figure 3.37. Potential profiles on insulation films stressed by unipolar and bipolar pulses, with a switching frequency of 3 kHz and a maximum electric field of 14.1 kV/mm at the tip of the point electrode. The horizontal axis corresponds to the horizontal position on the film from the centre of the film, and the vertical axis is the measured surface potential.

The surface potential profile was obtained by sweeping the probe across the surface using a linear motorized positioning device with steps of 1 mm, starting at the centre of the film to the edge.

79

Figure 3.37 shows the potential profiles related to surface charge for the three films in Table 2.3 and for both unipolar and bipolar square waves. The highest surface potential, or surface charge, is observed to be on the PTFE sheet, followed by mica and then PA6 when stressed with unipolar pulses. The accumulated charge under bipolar stress is significantly reduced on all films.

3.4.5 Surface Charge Measurements Using the Capacitance of Low Voltage Probe

Using the method described in section 2.9, the accumulated surface charge was estimated on PA6, PTFE, Kapton®, and mica sheets in order to examine the effect of switching frequency and pulse type. The method was tested at several pulse voltages and compared to non-contacting surface potential measurements.

Figure 3.38 shows the estimated surface charge measured at the switching frequencies of 500 Hz and 3 kHz on PA6 and PTFE films after five minutes of pulse stressing using unipolar pulses of 2.8 kV for PA6 and 3.0 kV for PTFE, producing the same electric field of 14.1 kV/mm at the tip of electrode and calculated by capacitance. Each measurement point was repeated five times.
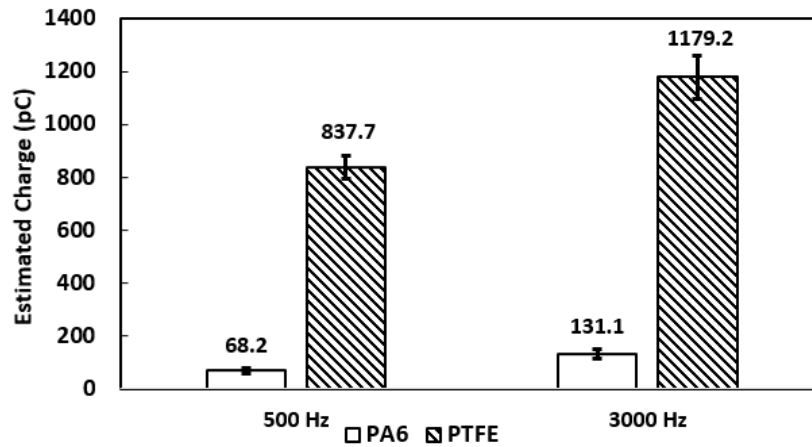
Figure 3.38. Estimated surface charge on PA6 and PTFE films when stressed for five minutes under unipolar pulses with the same electric field (PA6 @ 2.8 kV and PTFE @ 3 kV) and at 500 Hz and 3kHz switching frequencies.

Charge estimations were also repeated for mica and Kapton® sheets, which are the key materials used in machine insulation. The applied pulse voltage was adjusted to 4.2 kV and 2.85 kV, based on their permittivity and thickness values (Table 2.3) to impose the same electric field to that of PA6 and PTFE. Figure 3.39 shows the surface charge estimates for all four materials.
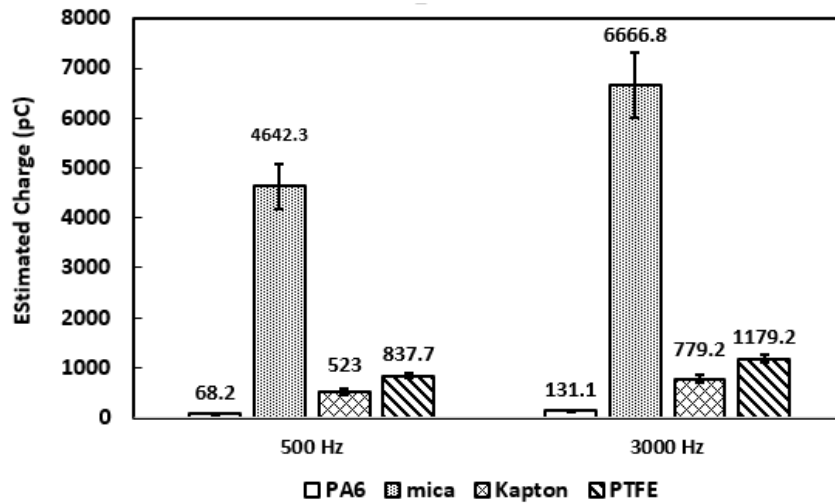
Figure 3.39. Estimated surface charge on PA6, mica, Kapton®, and PTFE films when stressed for five minutes under unipolar pulses (PA6@ 2.8 kV, mica@ 4.2kV, Kapton®@ 2.85kV, and PTFE@3 kV) for the same electric field and at 500Hz and 3 kHz switching frequencies.

It is evident that the accumulated charge on the mica sheet is considerably higher than on the Kapton®, PA6 and PTFE films. The surface charge was also estimated after stressing the films with bipolar pulses. These results are shown in Table 3.5. The estimated charge on all four films was significantly higher with unipolar than with bipolar pulses, which is an indication of charge neutralization taking place with bipolar pulses. Once again, mica sheets showed the highest charge accumulation followed by PTFE, Kapton® and PA6, respectively, for both unipolar and bipolar pulses. These results are in agreement with surface potential measurements using the non-contacting probe.

Table 3.5. Comparison of the estimated accumulated charge in pC using bipolar and unipolar pulses at 3 kHz switching frequency with the same electric field applied to the films

Insulation Film	Bipolar (pC)	Unipolar (pC)
PA6	14.2	131
Mica	127.0	6666
Kapton®	34.7	779
PTFE	90.0	1179

81

3.4.6 **Estimating the Barrier Film Surface Charge in the Point-to-plane Setup**

Corona discharge from the needle tip gives rise to PD as well as aging of the films with time. Through trial and error, it was found that a 2.4 kV unipolar square wave applied to PA6 gave the same times-to-failure as 3 kV applied to PTFE film, as presented in section 3.4.2. This suggests that the electric field in the air gap with PA6 film on the plane is the same as the electric field with PTFE, with 2.4 and 3 kV applied, respectively, to PA6 and PTFE. It was also suggested that 0.2 kV of this difference may be attributable to the difference in permittivity of the materials 2.1 and 3.6, respectively, for PTFE and PA6. Furthermore, 0.4 kV of this difference is the potential that results from the surface charge as affected by the surface resistivity.

To further support the experimentally derived test voltages for equal times-to-failure for both materials, COMSOL® simulation of the test geometry was used by adding a charge distribution based on the measured surface potential shown in Figure 3.37 and estimated charge shown in Figure 3.39. The distribution functions were extracted from each potential distribution from Figure 3.37 and multiplied by a coefficient to make the corresponding total estimated charge value reported in Figure 3.39 when integrated over the film surface, as illustrated in Table 3.6. The surface charge estimation and surface potential measurements were repeated for PA6 at 2.4 kV when stressed by unipolar waves of 3 kHz frequency in order to compare the results with PTFE at the same electric field in the presence of space charge, as confirmed by the lifetime test. The total estimated charge was 53.3 pC, and the surface potential was added to the Figure 3.37. Figure 3.40 shows the charge distribution with adjusted charge densities for the considered materials.

Table 3.6. Extracted charge distribution function for the studied materials

Material	Estimated Function
PA6	$10^{-14}(5 \times 10^{-5}\, r^4 - 0.005\, r^3 + 0.11\, r^2 - 1.07\, r + 8.88)$
Mica	$0.0336 \times 10^{-12}(0.005\, r^4 - 0.17\, r^3 + 1.44\, r^2 - 19.95\, r + 399.03)$
Kapton®	$0.0046 \times 10^{-12}(0.023\, r^4 - 1.028\, r^3 + 15.59\, r^2 - 106.92\, r + 512.21)$
PTFE	$0.09 \times 10^{-12}\left(-1.76 + \dfrac{752.82}{1 + \left(\frac{r}{1.43}\right)^{2.51}}\right)$

By adding the charge distribution presented in Figure 3.40, the maximum electric field in the air gap at the tip of the point electrode, which initiates PD pulses and aging of the insulation, was estimated using the electrostatic study.
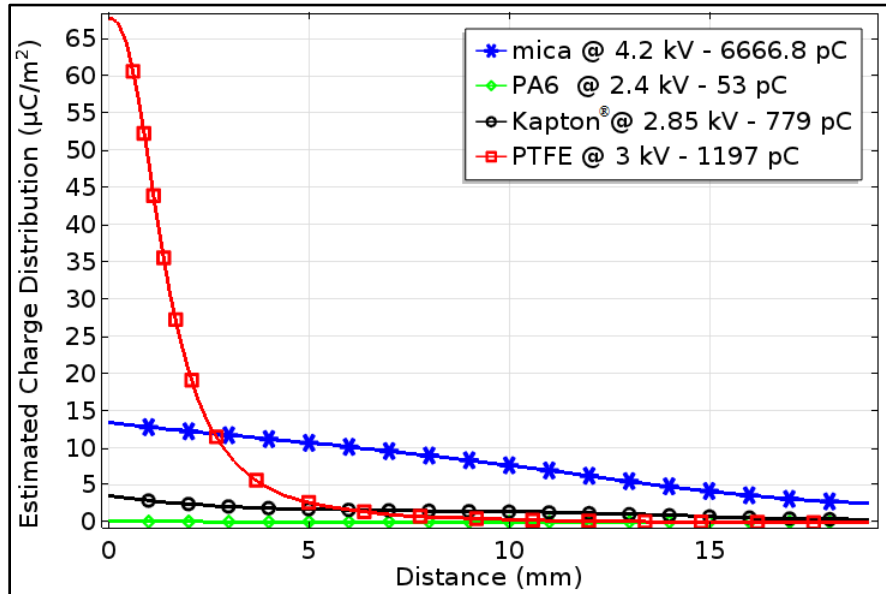
Figure 3.40. Extracted charge distribution functions for different materials using surface potential measurements and surface charge estimation for unipolar pulses of 3 kHz switching frequency. The total estimated charge for each material is equal to integration of each function over the surface.

Figure 3.41 demonstrates the electric field distribution in the air gap as well as its value using the cutline from the surface of the plane electrode to the point electrode.
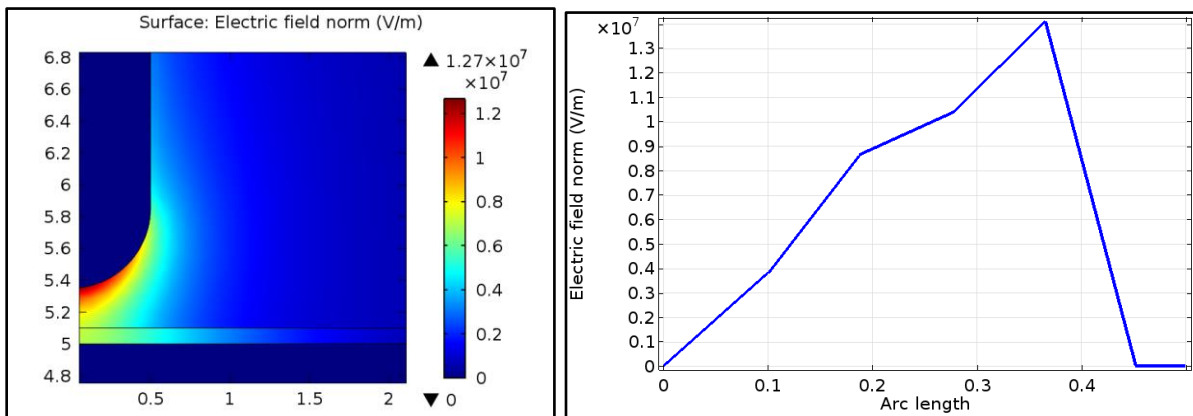
Figure 3.41. An example of electric field distribution in the air gap. The arc length is the distance from the surface of the plane electrode toward the point electrode in millimeters.

Table 3.7 summarizes the simulation results of estimating the maximum electric field at the tip of the point electrode for different materials, with surface charge added to the films. As can be seen, the electric field for PA6 at 2.4 kV is equal to that of PTFE at 3 kV, confirming the reduction of the electric field on the surface of PTFE due to the presence of surface charge. The electric field is highest for mica due to its lower charge density compared to that of PTFE.

Table 3.7. Comparison of the estimated charge density ρ_0 under the point electrode for the materials under study

Insulation Film	Charge Density ($\mu C/m^2$)	Applied Voltage (kV)	Max Electric Field (kV/mm)
PA6	0.1	2.40	12.17
Mica	13.4	4.20	13.26
Kapton®	2.4	2.85	14.02
PTFE	67.7	3.00	12.47

3.4.7 Effect of Humidity and Temperature on PD Features

The point-to-plane setup placed in an environment chamber is used to investigate the effect of humidity and temperature on PD features as back-to-back samples are sealed after VPI, making them isolated from environmental parameters. Table 3.8 shows the results on the effect of increasing humidity on PD features at room temperature. In each test point, unipolar square waves with a peak voltage of 6 kV, a switching frequency of 1 kHz, and a rise time of 100ns were applied to the test cell for one minute. The PD events were captured with the antenna. The captured data were then analyzed using MATLAB, and PD features such as amplitude and number of occurrences in each part of the wave were extracted.

As can be seen from Table 3.8, the threshold humidity is at 0.015 kg/m^3, where the discharges on the DC part of the wave diminish in number. The time to inception represents the time measured from the point at which the voltage rises to the first PD. The time to inception increases with increased humidity so that PD occurs after the rise time.

In addition, higher humidity results in having higher magnitudes of PD, as can be observed from Table 3.8. These observations can be explained by considering the effect of humidity on charge accumulation and on the breakdown strength of air when pulsed voltage is applied.

84

Table 3.8. Dependence of PD Features on Absolute Humidity at Room Temperature (23 °C)

Humidity (kg/m³)	Average Number on DC part of the wave	Time to Inception (ns)	Max Amplitude (V)
0.011	16	102	2.6
0.013	10	103	3.7
0.014	31	103	4.2
0.015	1	133	5.7
0.016	1	156	4.7
0.018	1	174	7.2
0.019	2	245	17.0

The experiment was repeated at 50°C, the humidity was varied between 0.01 and 0.05 kg/m³ under 6 kV square wave pulses, and the PD events were recorded. Table 3.9 shows a summary of test results. For lower humidity levels, the results follow the same pattern as at room temperature. However, and different from the results at room temperature, the peak PD decreased with increased absolute humidity. This may be due to the combined effect of humidity and temperature on forming droplets, thereby reducing the charges while increasing the chance of complete breakdown on the surface of the insulation film.

Table 3.9. Dependence of PD features on absolute humidity at 50 °C

Humidity (kg/m³)	Average Number on DC Part of the Wave	Time to Inception (ns)	Max Amplitude (V)
0.011	6	126	1.9
0.020	13	114	2.2
0.027	21	100	2.7
0.031	9	105	0.4
0.042	15	117	0.8
0.051	7	122	0.9
0.053	1	236	14.3
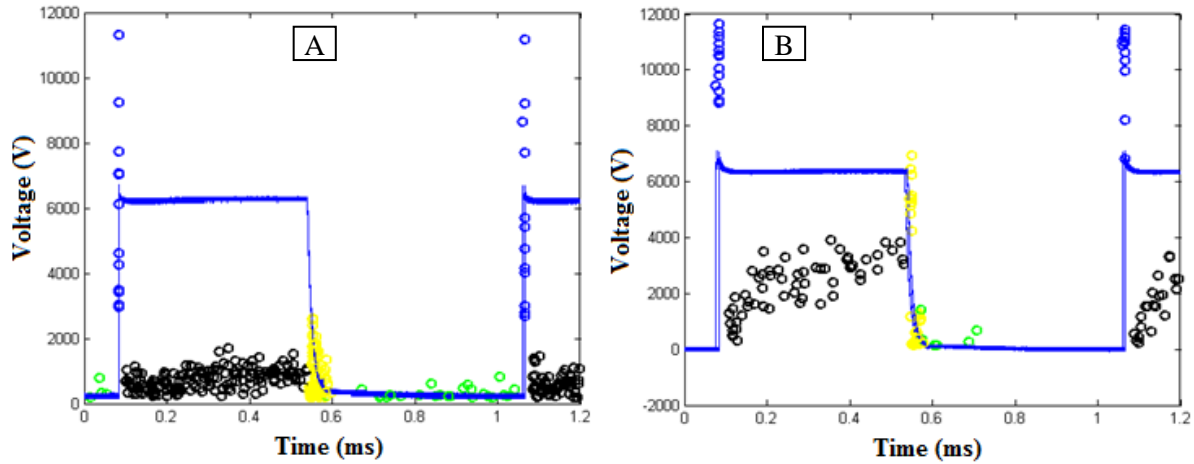
Figure 3.42. Phase-resolved PD pattern of point-to-plane insulation barrier under 6 kV square waves, with a switching frequency of 1 kHz at absolute humidity of 0.011 kg/m^3 and a temperature of 23 °C in (A) and 50 °C in (B). The circles represent the location and relative intensity of each PD event, where blue, black, yellow and green circle represent PD at rise, fall, DC part, and zero part of the wave, respectively.

Figure 3.42 shows the phase-resolved representation of PD events with respect to the applied waveforms at 23 °C and 50°C, while the absolute humidity level was fixed at 0.011 kg/m^3 and the 6 kV peak voltage square waves with a switching frequency of 1 kHz were applied. The PD events here are classified according to their location of occurrence at rise time, DC part, fall time, and zero voltage level, and are marked with blue, black, yellow, and green circles, respectively.

Chapter 4

Discussion

4.1 Introduction

This chapter discusses the results presented in the previous chapter. The parametric studies for both back-to-back samples and film insulation samples are analyzed, and the aging mechanism under square pulses are presented and discussed. As well, the results obtained from charge accumulation measurements are employed to characterize and validate time-to-failure examinations.

4.2 Time-to-failure of Back-to-back Samples under Square Wave Stress

This section discusses the results of the time-to-failure testing for different test parameters and relates them to the PD activities as the dominant factor in insulation failure. The infrared camera measurements of the temperature rises in the samples being aged provided confirmation that thermal aging does not take place, as only a few degrees of temperature change were recorded. Therefore, it is reasonable to assume that the PD occurs as a result of the accumulation of space charge and/or possibly the presence of a sufficiently strong electric field.

4.2.1 Effect of Rise Time on Aging

No significant differences were observed in the time-to-failure for the two rise times considered for the 50% duty cycle (Figure 3.8). This finding contradicts those presented in [27], [39], [40], in which the times-to-failure of enamel samples of random-wound machines under PWM pulses with faster rise times were reported to be shorter. However, the times-to-failure were observed to be independent of rise time when mica-based samples were aged under PWM pulses [27], [29]. The PD results shown in Figure 3.13a and Figure 3.13b are in agreement with the results of life tests shown in Figure 3.8, as the PD features are fairly similar. Both cases involve PD with high magnitudes that occur at the rise and fall, and the PD is also extended by about 10 µs over the flat portion of the wave.

Earlier investigations by [33] and [35] also did not find any change in PD behaviour when stressing twisted pair enamel samples under different rise times. The peak amplitude of the PD is higher for faster rise times, as shown in Figure 3.14 and in Table 4.1. This finding is in agreement with those reported in [31] and [36]. It is thus reported that a higher PD peak magnitude is not the only parameter that

causes failure, but that the number of PD occurrences, along with their position/amplitudes, influence the failure results, as the times-to-failure are the same for both rise times considered.

As shown in Figure 3.14, greater numbers of PDs are spread over the wave for a slower rise time, while the PD peak signal is higher for a faster rise time. This effect is indicated statistically in Table 4.1. It can be concluded that the higher number of PDs occurring with a slower rise time compensates for the higher PD amplitude at a faster rise time as PD energy is more effective than PD magnitude. Therefore, it is not possible to directly relate PD peak magnitude to the time-to-failure of the insulation, as the synergetic effects of PD occurrence and their strength result in material degradation.

Table 4.1. Statistics related to the PD features for square waves with a 3 kHz switching frequency and a 6 kV applied voltage for different rise times and duty cycles

Rise Time (µs)	Duty Cycle (%)	PD Amplitude (V)	PD Number
0.27	50	4.1	618
4.50	50	3.5	629
0.27	15	4.0	410
4.50	15	2.3	479

When the duty cycle is reduced from 50% to 15% (Figure 3.13b and Figure 3.13d, respectively), the number of occurrences of PD diminishes and the PD is evident primarily at the rise and fall times of the waves. This result may be due to the greater relaxation time created by the reduction in the time in which the electric field is present in the insulation. This could lead to a lower accumulation of the space charge, thus causing discharges in the flat portion. In such a case, it is possible to observe the effect of the rise time. At a fast rise time of 270 ns, due to the presence of the time lag in the formation of the discharge, the electric field exceeds levels well above the PD threshold before the discharge takes place, generating additional charges. Assuming a similar time lag for slower rise times, the electric field enhancement is lower for a slower rate of rise so that a smaller amount of charge is generated (Figure 4.1). This effect may explain why the peak of the PD magnitude is higher and also why failure occurs relatively sooner at the reduced duty cycle for the faster rise time, as shown in Figure 3.9.
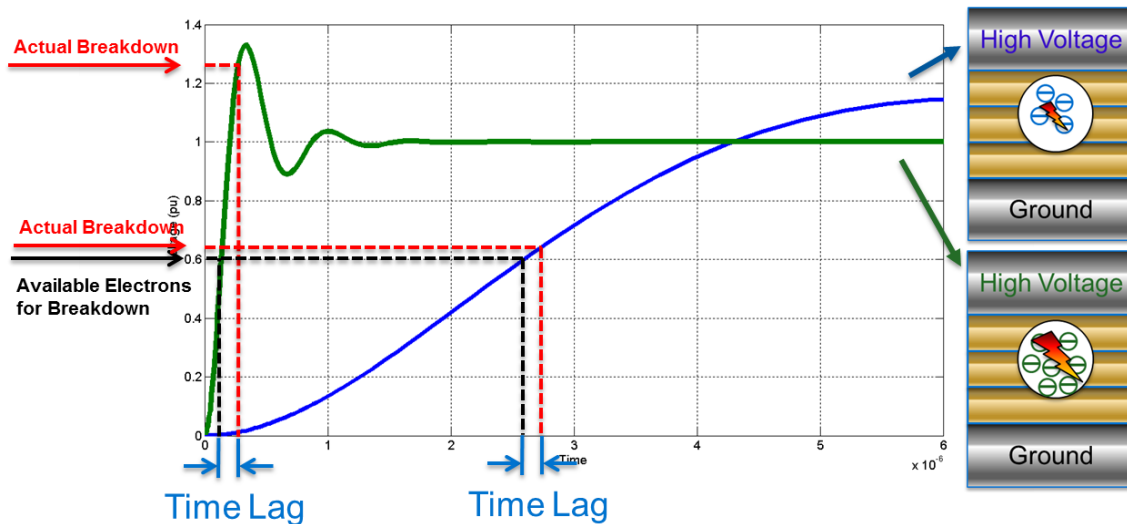
Figure 4.1. Higher magnitude of PD for different rise times.

The IEC standard has recognized rise time as a significant aging factor for turn insulation systems, mainly due to the uneven voltage distribution on stator coils resulting from the high frequency component of fast rise time pulses [1]. In the present research, faster failures under faster rise times are only observed at duty cycle of 15%.

4.2.2 Effect of Duty Cycle on Aging

At a slow rise time of 4.5 µs, the effect of duty cycle on PD features can be observed in Figure 3.13b and Figure 3.13d, for duty cycles of 50% and 15%, respectively. The results show that, for 15%, the PD events are concentrated on the transients, while for 50%, they extend over the flat portion and with a high amplitude. This effect occurs because of the accumulation of greater charges for the pulse with a longer duty cycle, in which case the electric field is present for a longer time. Therefore as indicated in Table 4.1, the number of PDs increases from 479 to 629 when the duty cycle is increased from 15% to 50%. Relating this observation to the results of the time-to-failure tests shown in Figure 3.10, one can say that additional numbers of PDs with a high PD amplitude can contribute to faster failures, as occurred for 50%, rather than concentrated high amplitude pulses with lower rise time numbers, as occurred for 15%. Grzybowski [40] also reported faster failures at higher duty cycles.

It can also be noted that a higher number of PDs as well as the occurrence of PDs in the flat portion contribute to faster failure. Although accumulated pulses are present with a high amplitude at 15%,

89

failure is faster at 50%, where a greater number of PDs are observed. It can be inferred from this that the number of PDs and the sum of the PD amplitudes represent the total energy delivered to the insulation by the PD, which is related to the failure of the insulation.

Another interesting point is the role of 'ON' time and duty cycle in aging. As illustrated in Figure 4.2, while the 3 kHz wave with a 15% duty cycle (upper trace) has the same 'ON' time as the 8.3 kHz wave (lower trace), the slope of the Weibull plot for 8.3 kHz parallels the one for the same duty cycle (middle trace with 3 kHz and 50% duty cycle), but not the same 'ON' time (3 kHz and 15% duty cycle). This observation indicates that the flat portion itself and the time between two adjacent transients both play a role in PD features and aging, as they might affect the rate of accumulation of the space charge in the insulation. As can be seen, the aging results can be misinterpreted if the effect of duty cycle is not considered. Hence, it is recommended that the IEC standard considers recognizing this parameter.
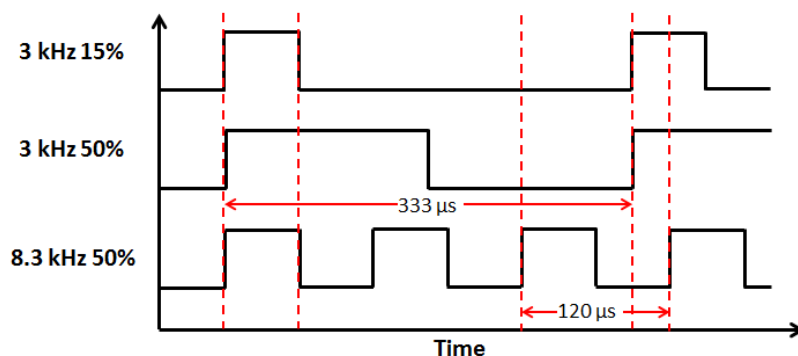
Figure 4.2. Comparison of 8.3 kHz wave with 3 kHz with the same ON time (upper trace) and 3 kHz with the same duty cycle as 8.3 kHz wave (middle trace).

4.2.3 **Effect of Switching Frequency on Time-to-failure**

It was observed that increasing the switching frequency from 0.5 kHz to 1 kHz reduced the time-to-failure by a factor of two (Figure 3.15). However, the slope of the reduction decreases with switching frequency. A similar trend is seen in Table 3.4, where PD measurements are reported at different switching frequencies for point-to-plane setup. Here we can see that the PD_{rms} increased from 4.5 mV to 11.3 mV when the switching frequency was increased from 0.5 to 1 kHz, whereas only an increase to 15.3 mV occurred when the frequency was further raised to 3 kHz. Similar observations were made with bipolar waves. Figure 4.3 illustrates the results reported in Table 3.4 relating the time-to-failure of

back-to-back samples to the measured RMS value of the PD at different frequencies and square wave types. This means that the energy in the PD pulses, or PD_{rms}, decreases with increasing switching frequency. It should be noted that in order to observe the trend properly, an additional measurement point of 750 Hz was added to the dataset for both unipolar and bipolar cases. A similar saturation of PD amplitude at switching frequencies higher than 500 Hz was reported on twisted enamel wires using square waves [35] and [37]. However, [29] reported the time-to-failure as being only a function of number of cycles when using aging mica-based insulation, whereas the IEC standard listed the switching frequency as a significant aging factor [1].

Reductions in PD_{rms} are caused by a reduction in surface charge transfer and may also be due to the mobility of the surface charges on the insulation film. As the switching frequency increases, the time becomes shorter for charge depletion on the insulation film reducing the PD magnitude, thus resulting in a residual charge on the surface that increases with increasing switching frequency. This is confirmed by surface charge measurements of insulation films using point-to-plane setup at different switching frequencies. Comparing the surface charge in Figure 3.39 (estimated at 500 Hz and 3 kHz), it is evident that the charge does not increase with frequency in the same ratio, rather saturation of the accumulated charge takes place.
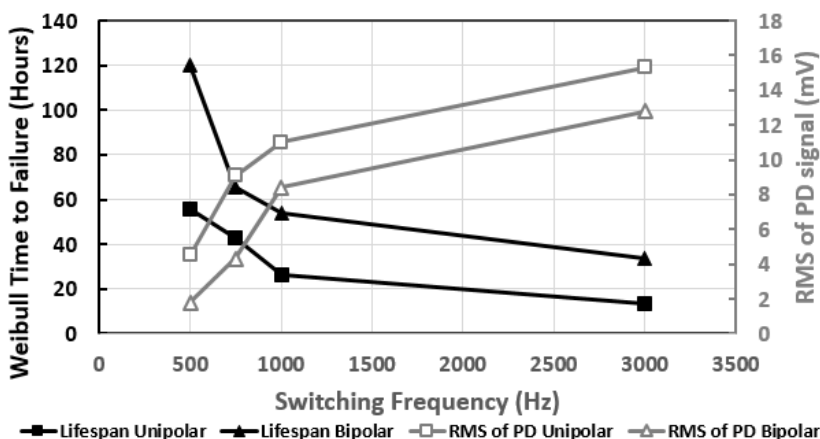
Figure 4.3. Time-to-failure of back-to-back samples with switching frequency for unipolar and bipolar waves.

4.2.4 **Effect of Applied Pulse Type**

It is evident from Table 3.7 that the charge accumulation is significantly lower under bipolar pulses compared to that of bipolar ones. This observation is in agreement with the results presented in

Figure 4.3. Under the unipolar square wave, stress accumulation of positive charges that drifted away from the positive electrode on the surface of the insulation film takes place at the rise of the wave with the occurrence of the PD. Some of the charges are dissipated with the later discharges on the DC portion of the square wave or during the fall time. Therefore, in case of unipolar pulses, charge dissipation comes at the cost of PD occurrence and insulation aging. On the other hand, when the insulation is stressed under bipolar pulses, the positive charges generated at the rise time of the wave are neutralized with the negative charges generated at the fall time, and any additional remaining charges will contribute to form a PD discharge. Hence, the dominant portion of the generated charge recombines with the opposite polarity charges rather than generating new PD pulses. This explains why the PD amplitude presented in Figure 4.3 and the accumulated charge presented in Table 3.7 and Figure 3.37 are significantly lower under bipolar square waves.

Figure 4.4 shows a scanning microwave microscopy (SMM) image of the surface of PA6 after one hour of aging before failure. It is evident that PD in the air gap causes holes in the surface of the insulation film. The mechanism in forming these holes is unknown; however, the appearance does not suggest melting or thermal erosion from PD to be the reason. Physical erosion may be possible, but the appearance of holes seems to be more in line with localized dielectric punctures that likely comes about due to accumulated surface charge giving rise to electric fields that reach the intrinsic breakdown (20 kV/mm) of the film.
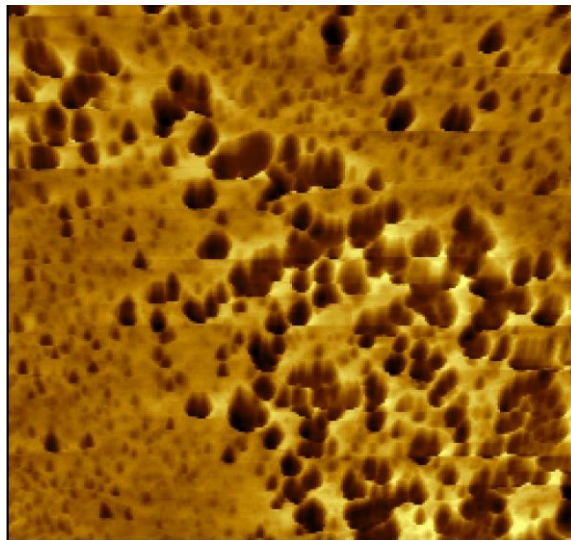
Figure 4.4. Scanning microwave microscopy (SMM) image of the surface of PA6 film after one hour of PD aging and preceding failure. The scan area is 17 x 17 microns.

Table 3.5 shows the accumulated charge for unipolar pulses to be significantly higher than for bipolar pulses. Assuming localized dielectric puncture due to accumulated surface charge as the reason for forming these holes, the time-to-failure under unipolar pulses having higher charge will be shorter than bipolar pulses with lower surface charge.

4.3 PD Mechanism in the Presence of Surface Charge

This section presents the mechanism of PD occurrence in the presence of surface charges based on the pulse stressing results of point-to-plane setup. Figure 4.5 illustrates the sequence of events that can explain the results obtained during the application of a unipolar square wave to the point-to-plane setup.

Initially, there is no surface space charge on the barrier film. Then, when the front of the positive trending square wave of voltage V_s yields an electric field E_s within the gap that equals or exceeds the electric field for breakdown of the gap E_g, a discharge occurs on the front of the square wave. This PD, according to [30], gives rise to a positive surface charge which accumulates on the barrier film during the DC portion of the square wave. The surface charge reduces the electric field within the gap, falling below the electric field that is required for PD, as illustrated in Figure 4.5b. Hence, no PD occurs during the DC portion of the square wave. It is then assumed that the duration of the square wave is short relative to the relaxation time of the accumulated surface charge, so it essentially remains in place until the fall of the square wave voltage to zero. At this point, the charge discharges to the point producing PD, as illustrated in Figure 4.5c. The occurrence of space charge PD neutralizes a portion of the total charge and thus the sequence repeats itself, with some charge being present on the barrier surface of subsequent applications of the unipolar square wave. Therefore, we can see that PD events take place at both the rise and fall times of the square wave, even after the external electric field is reduced to zero at the fall time of the wave.

In the case of a bipolar square wave applied to the point electrode of the point-to-plane configuration, which has a peak-to-peak voltage equal to the peak voltage of the unipolar square wave, the transition from positive to negative polarity enhances the electric field in the air gap by adding to the positive space charge field (Figure 4.6a). This enhancement produces a PD that completely depletes the positive charge on the film and leaves a negative space charge, as illustrated in Figure 4.6b. This negative space charge is lower than the positive space charge under unipolar square waves due to some neutralization of charge that takes place on the surface when the bipolar wave changes its polarity. Thus, the charge accumulation is lower under bipolar than under unipolar square waves, so the PD

magnitude will also be lower. Finally, when the bipolar wave switches from negative to positive polarity, another PD develops due field enhancement, this time because of the summation of applied field with that of the negative space charge (Figure 4.6c). In consequence, a positive space charge develops on the film, but once again, of lower magnitude than in the case of a unipolar square wave, as shown in Figure 4.6d.

$E_G = E_S > E_{PD}$ $E_G = (E_S - E_{SP}) < E_{PD}$ $E_G = E_{SP} > E_{PD}$

(a)   (b)   (c)
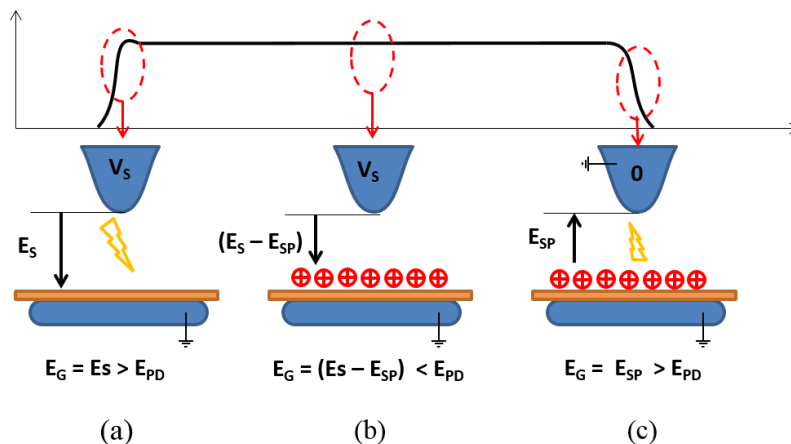
Figure 4.5. Development of space charge and occurrence of PD on a unipolar square wave applied to the point-to-plane setup with barrier insulation; during the rise time in (a), during the DC in (b), and during the fall time in (c).

$E_{Gap}=-E_S/2 - E_{SP}$ $E_{Gap}=-E_S/2 + E_{SP}$ $E_{Gap}= E_S/2 + E_{SP}$ $E_{Gap}= E_S/2 - E_{SP}$

(a)   (b)   (c)   (d)
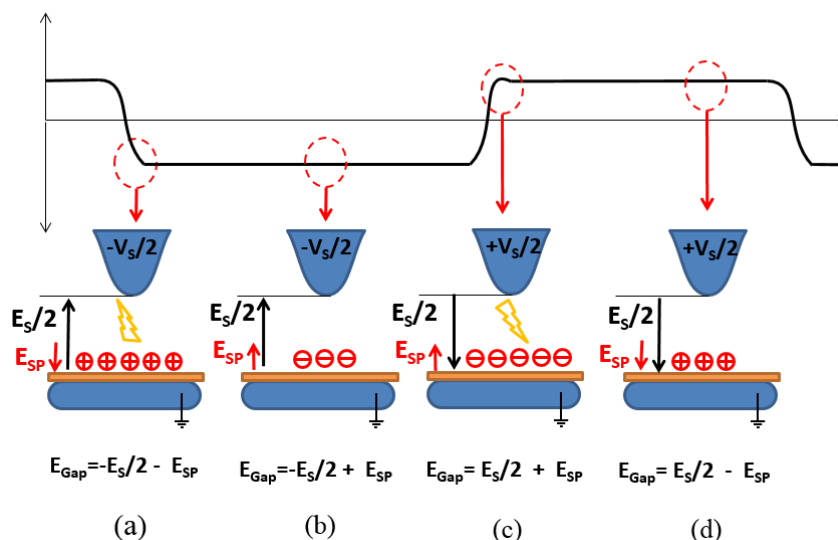
Figure 4.6. Development of space charge and occurrence of PD on a bipolar square wave applied to the point-to-plane setup with barrier insulation; during the fall time in (a), during the negative DC in (b), during the positive DC in (c), and during the rise time in (d).

94

In summary, the descriptions given in Figure 4.5 and Figure 4.6, respectively, describe the PD activities that result from space charge under unipolar and bipolar waves in point-to-plane geometry. Further, these PD features are correlated to the time-to-failure results of the turn insulation.

The abovementioned mechanism was validated by conducting measurements on the direction of PD pulses at the rise and fall times for unipolar waves. As illustrated in Figure 4.7, the PD pulse at the rise time has the opposite polarity compared to that which occurs at the fall time, suggesting an opposite direction of discharge for rise and fall times.

Figure 4.7. Comparing the measured PD pulse polarities at rise and fall times.

4.4 Effect of Humidity and Temperature on PD Features of Point-to-plane Setup

The effects of different pulse parameters on the aging of insulation of back-to-back samples were discussed in the previous sections. In order to show the influence of humidity and temperature, the point-to-plane setup was used to stress the insulation films under square wave stress. The obtained results are discussed in this section.

The application of a positive pulse on the point electrode with respect to the ground plane enhances the electric field in the air gap. According to the results presented in [30], field enhancement causes an accumulation of charges with the same polarity as the applied field on the surface of the insulation. Therefore, a higher accumulation of these charges reduces the electric field in the air gap. However, when the electric field in the air gap reaches the required level for developing a discharge, a PD occurs and neutralizes some of the accumulated charges. This discharge may appear anywhere along the DC portion of the wave. An increase in absolute humidity reduces the surface conductivity of the insulation,

as reported in [45], which accelerates the rate of recombination of charges while decreasing the space charge on the surface. As a consequence, the electric field in the air gap increases with the decrease in the electric field arising from the space charge.

The outcome is an increased rate of occurrence of PD on the DC portion of the wave. This explains why the average PD number increases when the humidity level rises from 0.011 to 0.014 kg/m^3. However, this is not the only consequence of increased humidity, as inferred from Table 3.8 for humidity levels higher than 0.015 kg/m^3. As reported in [60] and [48], increased humidity causes an increase in PDIV as well as the breakdown strength of air in the gap. Hence, the electric field is not high enough to form a discharge on the DC part of the wave, and the discharges appear only at the transients.

The occurrence of PD at polarity reversals of the waves is because of the combined effect of charge accumulation on the surface and the rapid transient of the applied voltage, as discussed in section 4.3. The PD amplitude at transients has a higher magnitude because of increased PDIV as a result of a rise in the absolute humidity level. It also increases the time-to-inception of the discharges at rise times.

From Table 3.8, it can be noted that at 0.019 kg/m^3 (94% relative humidity at 23ºC), the PD amplitude shows a large jump to 17 V, which indicates a very large discharge. This is due to the extremely high humidity level leading to the formation of water droplets in the air gap (at the interface). In some cases, the water droplets complete a path over the surface of the film, resulting in a complete breakdown over the surface.

As is evident from Figure 3.42, increasing the temperature from 23°C to 50°C resulted in a fewer number of discharges, while their intensity increased on the DC part of the wave. Therefore, increasing the temperature increases the rate of charge recombination on the surface, thereby reducing the space charge and the number of discharges. In addition, the reduction in the electric field that arises from the space charge enhances the electric field in the air gap, which then results in the development of discharges with higher amplitudes on the DC portion of the wave. An increase in PD magnitude on the fall time of the wave, evident in Figure 3.42, supports the mechanism presented earlier.

4.5 Surface Charge Accumulation

There are two mechanisms that contribute to the reduction of surface charge with time on the barrier film. The first is charge neutralization, which takes place during the PD under square wave pulses. A

96

portion of the surface charge can be expected to be neutralized with each PD pulse that is dependent on the applied electric field. It is reasonable to assume that, over time, an equilibrium surface charge will remain on the surface. The second mechanism is the dissipation of charge due to surface conductivity. The lower the surface resistivity, the faster the rate of charge dissipation. Regarding the fact that the charge distribution on the sheets are different, it is reasonable to compare the charge densities instead of the total accumulated charge.

According to Figure 3.39, PTFE with the highest surface resistivity has the highest charge density, followed by mica and PA6 with lower surface resistivity. Although the total charge on PTFE is not significant, it is mostly concentrated under the tip of the point electrode as a result of its high resistivity preventing the charge to spread on the surface.

Regarding mica, there is a high charge density under the tip of the electrode as well as over the surface of the film, suggesting the high capability of charge accumulation and easier mobility of charge over the surface. It is well known that the atomic structure consists of atoms that are held together by strong covalent bonds forming flat sheets. The electrostatic interaction between the sheets is relatively weak, allowing for a perfect cleavage of the mineral to form a molecularly smooth, defect-free surface [61]. According to [61], the resin also helps to transport the accumulated charge to the surface. Moreover, the atomically flat surface over a large area allows for large charge density, as observed from the surface potential distribution seen in Figure 3.37. Therefore, the unique structure of mica results in having different charge accumulation behaviour compared to other homogenous materials studied. For instance, the presence of the surface charge density of 13.4 $\mu C/m^2$ reduced the max electric field from 14.1 kV/mm to 13.26 kV/mm, as presented in Table 3.7, which is still higher than that of PA6 and PTFE. Although the electric field is higher on the mica sheet, it is known to have a longer time-to-failure due to its inherent resistance to PD.

The COMSOL$^®$ simulations of computing the max electric field in the presence of a surface charge for different materials confirmed that the approximately 1048 pC higher accumulated charge ($Q_{PTFE@3kV}$ − $Q_{PA6@2.8kV}$) on the surface of PTFE (compared to that of PA6) reduced the maximum electric field in the air gap which resulted in longer times-to-failure at both 500 Hz and 3 kHz switching frequencies, while the initial electric field was set to be the same. Considering the measured equal times-to-failure of PTFE at 3 kV and PA6 at 2.4 kV, it was confirmed that the maximum electric fields in the air gaps of the two systems are equal when there is 1126 pC more charge ($Q_{PTFE@3kV}$ − $Q_{PA6@2.4kV}$) accumulated

97

on the surface of PTFE, while the applied voltage on PTFE and PA6 are 3 kV and 2.4 kV, respectively, under unipolar stress. A reduction in the strength of the electric field in the air gap with the increase of surface resistivity and therefore higher surface charge was also observed indirectly in the previous publication. Higher PD amplitude was observed when the absolute humidity was increased at a constant temperature while stressing under unipolar square waves. The increase in humidity resulted in a decrease in the surface charge and thus a decrease in the surface charge accumulation level. The result was an increase in the electric field in the gap and PD pulses with larger amplitudes [62].

Chapter 5

Conclusion and Suggestions for Future Work

5.1 Summary

The increased use of motor adjustable speed drives has given rise to the question of whether the distorted voltage waveform of the converter adversely affects the insulation of the machine. Many studies have been focused on this question, with most emphasizing the stress-grading system and relatively a few investigating the turn insulation. Hence, the effect of converter pulses on turn insulation of form-wound machines are investigated in the present research. Back-to-back turn insulation samples with enamel insulation were prepared based on IEC 60034-18-42, with improved insulation in the crotch region to prevent failure. A high voltage pulse generator along with an antenna-based PD measurement system was implemented to investigate the effects of several pulse parameters (e.g., rise time, switching frequency, pulse duty cycle, pulse type and applied voltage) on insulation aging. The performance of different insulation materials and constructions were also evaluated by aging back-to-back samples. It was reported that the pulses with the faster rise times and higher duty cycles led to faster times-to-failure. By examining the time-to-failure of turn insulation subjected to bipolar and unipolar pulses at different switching frequencies, it was presented that the PD behaviour and therefore times-to-failure was modified with the accumulation of surface charge for different pulse types and applied switching frequencies. A qualitative mechanism of PD pulses was suggested under both unipolar and bipolar pulses based on the experimental results.

A point-to-plane setup with an insulation film representing a single defect in the turn insulation system as a controlled single source of PD was used to investigate the PD features and their relationship to the times-to-failure of back-to-back samples. The results were employed to determine the main PD feature affecting time-to-failure of back-to-back samples.

By conducting time-to-failure examination, surface charge measurements, surface potential measurements, and FEM simulations on point-to-plane setup with different insulation films, the significance of charge accumulation on the time-to-failure of insulation samples was investigated and the results were used to explain the aging results of back-to-back samples and to support the presented aging mechanism.

5.2 Conclusions

- In evaluating different insulation materials subjected to unipolar PWM stress, it was concluded that the mica materials demonstrated the highest endurance, followed by samples of enamel and glass diffused enamel. Among the mica-based turn tape insulation samples investigated, 1/2 lap construction showed the highest endurance, followed by 2-layer butt lap, followed by 1/3 lap samples.

- The results of the time-to-failure tests as well as the PD measurements on the form-wound turn insulation samples were presented as a means of considering the effects of rise time, duty cycle, and switching frequency on the aging of insulation. For the two different rise times considered; namely 270ns and 4.5 μs aging and PD features were shown to be independent of rise time for a 50% duty cycle; however, slightly faster times-to-failure were observed at a 15% duty cycle for the faster rise time. Although the PD amplitude was higher for faster rise times, it is not likely a significant factor in the time-to-failure because PDs with lower amplitudes and higher numbers resulted in similar failure times. The PD pattern for different duty cycles led to different times-to-failure, such that a 50% duty cycle represented the worst case observed, with the highest number of PD pulses as well as the largest occurrence of PD along the flat portion. By increasing the switching frequency from 500 Hz to 3 kHz, the time-to-failure decreased linearly with the number of applied cycles up to about 750 Hz. However, it decreased non-linearly above this threshold, both under unipolar and bipolar waves. The time-to-failure under bipolar square waves was considerably longer than those for bipolar waves.

- The effects of humidity and temperature were investigated by stressing point-to-plane electrode geometry using 6 kV unipolar square pulses and a switching frequency of 1 kHz with a 250 μm air gap and a Kapton® film barrier on the ground plane electrode. The mechanism of PD development with the humidity of the air gap showed that increasing the absolute humidity enhances PD amplitude, while the discharges appear mainly at the polarity reversals of the wave. It was also found that at lower absolute humidity, an increase in temperature results in having a lower number of PD pulses with higher amplitudes on the DC portion of the wave.

- The time-to-failure tests and PD measurements on back-to-back samples of form-wound turn-to-turn insulation samples and on point-to-plane with barrier insulation were studied with unipolar and bipolar square waves and as a function of switching frequency. It was reported that variations in PD energy from the point-to-plane test on Kapton® film barrier insulation

correlates with the time-to-failure data from the back-to-back samples, showing the significance of PD energy on time-to-failure.

- It was observed that failure of the insulation films are preceded by holes in the surface of the film that likely come about due to localized intrinsic breakdown that is brought about due to charge accumulation and faster failures under unipolar pulses compared to bipolar.

- The surface charge accumulation was evaluated by measuring the charge using a capacitance and measuring the surface voltage profile under square pulse stress at different frequencies and pulse polarities to explain aging mechanisms under unipolar and bipolar pulses as well as different switching frequencies. It was observed that the accumulation of charge is not proportional to the increase in the switching frequency. The findings were employed to explain the reduced slope of aging at frequencies higher than 1 kHz on back-to-back turn insulation samples. It was also found that the surface charge accumulation is significantly lower when using bipolar pulses at the considered switching frequency for the studied materials, which confirms the longer measured times-to-failure of insulation samples stressed under bipolar waves.

- Using a combination of time-to-failure measurements, charge estimations, and FEM simulations, it was found that the accumulation of higher charge on the surface of PTFE results in the reduction of the electric field in the air gap compared to that of PA6 and results in a longer time-to-failure of PTFE when the applied voltages were selected to impose an equal electric field for both materials. The amount of charge contributing to the modification of the electric field was estimated. By estimating the charge density of the studied materials, we saw that mica has the highest charge density despite having a lower measured surface resistivity. This result was suggested to be attributable to the inhomogeneous and layered structure of mica sheets.

5.3 Potential Contributions

- The test equipment developed during this research including high voltage pulse generators, PD measurement system, and charge measurement system will contribute to further research and developments in high voltage engineering laboratory at the University of Waterloo.

- The improvements achieved during this research on the design of back-to-back turn insulation samples are being used by the manufacturer and has potentials to include in future revisions of IEC 60034-18-42 standard.

- The parametric study data on effect of different pulse parameters on aging of turn insulation samples can be employed by manufacturers to improve the design of converter fed machines.

- The suggested breakdown mechanism of form-wound insulation under pulse stress can contribute to better understanding of the form-wound insulation failure.

5.4 Suggestions for Future Work

The following presents the suggestions for future work based on the experience gained through the presented study:

- In the context of back-to-back sample preparation, using wires with larger cross-sections when preparing samples involving turn tapes is recommended. This allows the turn tape to settle on the wire completely and avoid the formation of air pockets on the surface of the wire. In order to conduct feasible aging experiments on mica-based samples, accelerated aging needs to be shortened, which can be done by developing thinner mica films or modifying the sample construction.

- The present research used the back-to-back samples representing the straight section of the stator coils. It is interesting to evaluate the performance of insulation system at bended areas such as coil ends which may introduce more defect and higher electric field, especially on the first coil, and compare the results with that of existing back-to-back samples.

- Regarding the fact that the accumulation of charge on form-wound insulation requires further investigations, implementing a charge measurement system specific to form-wound samples has great benefits.

- A comparison of different insulation materials at the same applied voltage was conducted in the present research. The life endurance of materials at the same electric field level could also be compared, but there are challenges that need to be addressed in doing so, such as variations in thickness from one sample to another.

- The implementation of a fully automated system capable of removing failed samples and conducting the aging test automatically was tackled in the present research, but it was unfortunately not completed. Such a system could be developed by implementing a current monitoring relay and high voltage disconnecting switch on each sample under the test.

- A PD measurement system capable of detecting the PD in the presence of PWM stress was implemented during this research, and PD pulses were captured using a high performance oscilloscope to extract PD features. In the future, a high performance electronic circuit could be implemented to extract PD features from each pulse and thus save only the pulse features rather than the full waveform. Such a system would help avoid losing the PD pulses while maintaining the maximum recording resolution.

- Mica-based turn insulation systems are typically used in Type II insulation of converter-fed motors. Currently, such an insulation system is applied that considers a large over-design factor, which then leads to a larger motor at higher costs. Future work could investigate the optimal thickness of the insulation system to fully withstand worst-case PWM stress while maintaining a minimal thickness.

- Findings confirmed that the PD is the main factor in the aging of insulation and that it typically stems from defects or air pockets in the insulation system. Future research efforts could conduct investigations on the materials and construction of insulation systems in order to minimize the possibility of defect formation or decrease the vulnerability of the insulation to PD activities. The study on enhancement of the properties of VPI epoxy or the use of nano-filled enamel insulation are the examples of interesting topics in this context.

- It was presented that the environmental parameters such as temperature, humidity, and pressure can modify the partial discharge characteristics. Hence, it is recommended to investigate the insulation performance in environmental conditions such as elevated temperature or testing the system at higher altitudes.

Bibliography

[1] "IEC 60034 Rotating Electrical Machines - Part 18-42: Qualification and Acceptance Tests for Type II Electrical Insulation Systems used in Rotating Electrical Machines Fed from Voltage Converters," *IEC 60034-18-42-TS Ed. 1.0*. 2008.

[2] E. Sharifi-ghazvini, "Analysis of Electrical and Thermal Stresses in the Stress Relief System of Inverter Fed Medium Voltage Induction Motors," PhD Thesis, University of Waterloo, Waterloo, Ontario, Canada, 2010.

[3] A. H. Bonnett, "Analysis of the impact of pulse-width modulated inverter voltage waveforms on AC induction motors," *IEEE Trans. Ind. Appl.*, vol. 32, no. 2, pp. 386–392, 1996.

[4] G. C. Stone and M. K. W. Stranges, "New IEC standards for qualifying stator insulation systems for PWM converter drives," *2007 Electr. Insul. Conf. Electr. Manuf. Expo, EEIC 2007*, pp. 94–97, 2007.

[5] G. C. Stone, I. M. Culbert, and B. A. Lloyd, "Stator Insulation Problems Associated With Low Voltage and Medium Voltage PWM Drives," in *Cement Industry Technical Conference Record*, 2007, pp. 187–192.

[6] M. K. W. Stranges, G. C. Stone, and D. L. Bogh, "Progress on IEC 60034-18-42 for qualification of stator insulation for medium-voltage inverter duty applications," *Rec. Conf. Pap. - Annu. Pet. Chem. Ind. Conf.*, 2007.

[7] E. Sharifi, S. H. Jayaram, and E. A. Cherney, "Analysis of thermal stresses in medium-voltage motor coils under repetitive fast pulse and high-frequency voltages," *IEEE Trans. Dielectr. Electr. Insul.*, vol. 17, no. 5, pp. 1378–1384, 2010.

[8] E. Sharifi, "Temperature and electric field dependence of stress grading on form-wound motor coils," *IEEE Trans. Dielectr. Electr. Insul.*, vol. 17, no. 1, pp. 264–270, 2010.

[9] F. P. Espino-Cortes, S. H. Jayaram, and E. A. Chemey, "Effectiveness of stress control coatings in medium voltage form wound coil ends under fast rise time pulses and contamination," in *IEEE EIC and Electr. Manufact.*, 2005, vol. 2005, pp. 167–170.

[10] "IEC 60034 Rotating Electrical Machines - Part 18-41: Qualification and type tests for Type I electrical insulation systems used in rotating electrical machines fed from voltage converters," *IEC 60034-18-41-TS Ed. 1.0*. 2005.

[11] F. P. Espino-Cortes, "Stress Grading Materials Evaluation and Performance," PhD Thesis, University of Waterloo, Waterloo, Ontario, Canada, 2002.

[12] J. C. G. Wheeler, A. M. Gully, A. E. Baker, and F. A. Perrot, "Thermal performance of stress grading systems for converter-fed motors," *IEEE Electr. Insul. Mag.*, vol. 23, no. 2, pp. 5–11, 2007.

[13] J. Wheeler and A. Gully, "Novel stress grading systems for converter-fed motors," *IEEE Electr. Insul. Mag.*, vol. 23, no. 1, pp. 29–35, 2007.

[14] A. Roberts, "Stress Grading for High Voltage Motor and Generator Coils," *IEEE Electr. Insul. Mag.*, vol. 11, no. 4, pp. 26–31, 1995.

[15] J. C. G. Wheeler, "Effects of converter pulses on the electrical insulation in low and medium voltage motors," *IEEE Electr. Insul. Mag.*, vol. 21, no. 2, pp. 22–29, 2005.

[16] S. U. Haq, "A Study on Insulation Problems in Drive Fed Medium Voltage Induction Motors," PhD Thesis, University of Waterloo, Waterloo, Ontario, Canada, 2007.

[17] S. U. Haq, S. H. Jayaram, and E. A. Cherney, "Evaluation of medium voltage enameled wire exposed to fast repetitive voltage pulses," *IEEE Trans. Dielectr. Electr. Insul.*, vol. 14, no. 1, pp. 194–203, 2007.

[18] S. U. Haq and E. A. Cherney, "Space Charge Accumulation in Induction Motor MagnetWire: A New Measurement Approach," *IEEE Trans. Energy Convers.*, vol. 22, no. 2, pp. 535–538, 2007.

[19] S. Ul Haq, S. H. Jayaram, and E. A. Cherney, "Performance of nanofillers in medium voltage magnet wire insulation under high frequency applications," *IEEE Trans. Dielectr. Electr. Insul.*, vol. 14, no. 2, pp. 417–426, 2007.

[20] G. G. Raju, "DC breakdown characteristics of high temperature polymer films," *IEEE Trans. Dielectr. Electr. Insul.*, vol. 13, no. 4, pp. 917–926, 2006.

[21] R. A. Hanna and S. W. Randall, "Medium-voltage adjustable-speed-drive retrofit of an existing eddy-current clutch extruder application," *IEEE Trans. Ind. Appl.*, vol. 36, no. 6, pp. 1750–1755, 2000.

[22] "Available at website: http://www.eetimes.com/." .

[23] "Available at website: http://www.emainc.net/newsletter/medium-voltage-drive-market/." .

[24] "Available at website: http://www.controleng.com/." .

[25] "Available at website: http://www.arcweb.com/." .

[26] "Available at website: http://www.tmeic.com/."

[27] W. Chen, G. Gao, and C. A. Mouton, "Stator insulation system evaluation and improvement for medium voltage adjustable speed drive applications," *Rec. Conf. Pap. - Annu. Pet. Chem. Ind. Conf.*, pp. 1–7, 2008.

[28] Y. Luo, G. N. Wu, P. Wang, K. J. Cao, and Y. Cui, "Insulation failure of inter-turn insulation in inverter-fed traction motor," *Annu. Rep. - Conf. Electr. Insul. Dielectr. Phenomena, CEIDP*, pp. 831–834, 2012.

[29] D. Manns, S. Galioto, K. Weeber, and J. Yagielski, "High Frequency Life Testing of Stator Coil Insulation," in *IEEE Inte'l . Symposi. Elect. Insul.*, 2008, pp. 269–272.

[30] D. Fabiani, G. C. Montanari, A. Cavallini, and G. Mazzanti, "Relation between space charge accumulation and partial discharge activity in enameled wires under PWM-like voltage waveforms," *IEEE Trans. Dielectr. Electr. Insul.*, vol. 11, no. 3, pp. 393–405, 2004.

[31] B. Florkowska, J. Roehrich, P. Zydroń, and M. Florkowski, "Measurement and analysis of surface partial discharges at semi-square voltage waveforms," *IEEE Trans. Dielectr. Electr. Insul.*, vol. 18, no. 4, pp. 990–996, 2011.

[32] E. Lindell, T. Bengtsson, J. Blennow, and S. M. Gubanski, "Influence of rise time on partial discharge extinction voltage at semi-square voltage waveforms," *IEEE Trans. Dielectr. Electr. Insul.*, vol. 17, no. 1, pp. 141–148, 2010.

[33] K. Wu, T. Okamoto, and Y. Suzuoki, "Effects of discharge area and surface conductivity on partial discharge behavior in voids under square voltages," *IEEE Trans. Dielectr. Electr. Insul.*, vol. 14, no. 2, pp. 461–470, 2007.

[34] M. Di Lorenzo del Casale, R. Schifani, and J. T. Holboll, "Partial discharge tests using CIGRE method II," *IEEE Trans. Dielectr. Electr. Insul.*, vol. 7, no. 1, pp. 133–140, 2000.

[35] D. Fabiani, G. C. Montanari, and A. Contin, "Aging acceleration of insulating materials for electrical machine windings supplied by PWM in the presence and in the absence of partial

discharges," in *IEEE ICSD*, 2001, pp. 283–286.

[36]   Peng Wang, A. Cavallini, G. C. Montanari, and Guangning Wu, "Effect of rise time on PD pulse features under repetitive square wave voltages," *IEEE Trans. Dielectr. Electr. Insul.*, vol. 20, no. 1, pp. 245–254, Feb. 2013.

[37]   P. Wang, A. Cavallini, and G. C. Montanari, "The influence of square voltage rise time on partial discharge spectra," in *IEEE CEIDP*, 2012, pp. 129–132.

[38]   K. Kimura, S. Ushirone, T. Koyanagi, Y. Iiyama, S. Ohtsuka, and M. Hikita, "Study of PD behaviors on a crossed sample of magnet-wire with repetitive bipolar impulses for inverter-fed motor coil insulation," in *IEEE CEIDP*, 2005, vol. 2005, pp. 393–396.

[39]   W. Yin, "Failure mechanism of winding insulations in inverter-fed motors," *IEEE Electr. Insul. Mag.*, vol. 13, no. 6, pp. 18–23, 1997.

[40]   S. Grzybowski, E. A. Feilat, and P. Knight, "Accelerated aging tests on magnet wires under high frequency pulsating voltage and high temperature," in *IEEE Electr. Insul. and Dielect. Phenom.*, 1999, vol. 2, pp. 555–558.

[41]   J. P. Bellomo, H. Olivier, and T. Lebey, "Lifetime determination of polyimide under square voltage waveforms," in *IEEE Electr. Insul. Conf. and Electr. Manufact. and Coil Winding Conf.*, 1997, pp. 419–423.

[42]   M. Kaufhold, G. Börner, M. Eberhardt, and J. Speck, "Failure mechanism of the interturn insulation of low voltage electric machines fed by pulse-controlled inverters," *IEEE Electr. Insul. Mag.*, vol. 12, no. 5, pp. 9–16, 1996.

[43]   D. Fabiani, "Accelerated Degradation of AC-Motor Winding Insulation due to Voltage Waveforms Generated by Adjustable Speed Drivers," Ph.D. Thesis, University of Bologna, Bologna, Italy, 2003.

[44]   Z. Nawawi, Y. Muramoto, N. Hozumi, and M. Nagao, "Effect of Humidity on Partial Discharge Characteristics," *Int. Conf. Prop. Appl. Dielectr. Mater.*, pp. 307–310, 2003.

[45]   Z. Nawawi, Y. Murakami, N. Hozumi, and M. Nagao, "Effect of Humidity on Time Lag of Partial Discharge in Insulation-Gap-Insulation System," *2006 IEEE 8th Int. Conf. Prop. Appl. Dielectr. Mater.*, pp. 199–203, 2006.

[46]   E. P. Waldi, Y. Murakami, and M. Nagao, "Effect of humidity on breakdown of low density polyethylene film due to partial discharge," *2008 Int. Conf. Cond. Monit. Diagnosis*, pp. 655–658, 2008.

[47]   L. Centurioni, F. Guastavino, and E. Torello, "An investigation about the PD degradation of thin polymer films and its correlation with surface charge decay measurements," in *IEEE Int'l. Sympo. on Electr. Insul.*, 2002, pp. 371–374.

[48]   M. Fenger and G. C. Stone, "Investigation of the effect of humidity on partial discharge activity in stator windings," in *Inter'l . Conf. on Prop. and Applic. of Dielect. Materials (ICPDAM)*, 2003, vol. 3, pp. 1080–1083.

[49]   Y. Kikuchi *et al.*, "Effects of ambient humidity and temperature on partial discharge characteristics of conventional and nanocomposite enameled magnet wires," *IEEE Trans. Dielectr. Electr. Insul.*, vol. 15, no. 6, pp. 1617–1625, 2008.

[50]   R. Soltani, E. David, and L. Lamarre, "Study on the effect of humidity on dielectric response and partial discharges activity of machine insulation materials," *2009 IEEE Electr. Insul. Conf. EIC 2009*, no. June, pp. 343–347, 2009.

[51]   R. Soltani, E. David, and L. Lamarre, "The impact of humidity on partial discharge activity of large rotating machines," *Conf. Rec. IEEE Int. Symp. Electr. Insul.*, 2010.

[52]   A. Cavallini, D. Fabiani, and G. C. Montanari, "A novel method to diagnose PWM-fed induction motors," *IEEE Trans. Dielectr. Electr. Insul.*, vol. 15, no. 5, pp. 1313–1321, 2008.

[53]   D. Fabiani, A. Cavallini, G. C. Montanari, and A. Caprara, "A technique for defect investigation in pulse-controlled motors through partial discharge measurements," *Conf. Rec. IEEE Int. Symp. Electr. Insul.*, no. September, pp. 196–199, 2004.

[54]   M. Hikita *et al.*, "Development of repetitive voltage impulse generator and automatic repetitive PD inception voltage measurement system for testing inverter-fed motor insulation," *Annu. Rep. - Conf. Electr. Insul. Dielectr. Phenomena, CEIDP*, pp. 145–148, 2012.

[55]   Y. Yu, "High Voltage Square-Wave and SPWM-Wave Generator Design and Application," MACs Thesis, University of Waterloo, Waterloo, Ontario, Canada, 2009.

[56]   "Available at website: http://www.irispower.com/motor_cm_pdalert.aspx." .

[57]   "Available at website: http://www.techimp.com/holding/Main/index.aspx." .

[58]   "Standard Test Methods for DC Resistance or Conductance of Insulating Materials," *ASTM D257-14*. .

[59]   "IEEE Guide for the Statistical Analysis of Electrical Insulation Voltage Endurance Data," *ANSI/IEEE Std. 930*. 1987.

[60]   P. Ortega, R. T. Waters, A. Haddad, R. Hameed, and A. J. Davies, "Impulse breakdown voltages of air gaps: a new approach to atmospheric correction factors applicable to international standards," *IEEE Trans. Dielectr. Electr. Insul.*, vol. 14, no. 6, pp. 1498–1508, Dec. 2007.

[61]   W. Loh and A. Hubbard, *Encyclopedia of surface and colloid science*. 2002.

[62]   M. S. Moonesan, S. H. Jayaram, and E. A. Cherney, "Effect of Temperature and Humidity on Surface Discharge Activities under High Voltage Unipolar Pulses," in *Electrostat. Society of America (ESA) Conf.*, 2015.